

WESTFÄLISCHE  
WILHELMS-UNIVERSITÄT  
MÜNSTER

# **Production of Pions, Kaons, Protons and Deuterons in p-Pb Collisions at $\sqrt{s_{NN}} = 5.02$ TeV Measured with ALICE**

Jonas Anielski, Dissertation 2014



EXPERIMENTELLE PHYSIK

**Production of Pions, Kaons,  
Protons and Deuterons in p-Pb  
Collisions at  $\sqrt{s_{\text{NN}}} = 5.02$  TeV  
Measured with ALICE**

Inaugural-Dissertation  
zur Erlangung des Doktorgrades  
der Naturwissenschaften im Fachbereich Physik  
der Mathematisch-Naturwissenschaftlichen Fakultät  
der Westfälischen Wilhelms-Universität Münster

vorgelegt von  
Jonas Anielski  
aus Ibbenbüren

— November 2014 —

Dekan: Prof. Dr. C. Weinheimer  
Erster Gutachter: Prof. Dr. J. P. Wessels  
Zweiter Gutachter: Priv.-Doz. Dr. H. Oeschler

Tag der Disputation:  
Tag der Promotion:





# Contents

<b>1. Motivation</b>	<b>1</b>
<b>2. Quarks, Gluons and the Strong Interaction</b>	<b>5</b>
2.1. Quantum Chromodynamics . . . . .	6
2.2. Quark-Gluon Plasma . . . . .	9
2.2.1. Space-Time Evolution of Ultra-Relativistic Particle Collisions	11
2.3. Signatures of the QGP . . . . .	13
2.3.1. Hydrodynamic Behavior . . . . .	13
2.3.2. Nuclear Modification Factor . . . . .	18
2.4. Cold Nuclear Matter Effects . . . . .	21
2.4.1. Cronin Effect . . . . .	21
2.4.2. Shadowing, Anti-Shadowing and EMC Effect . . . . .	23
2.4.3. Gluon Saturation – Color Glass Condensate . . . . .	25
<b>3. The ALICE Experiment</b>	<b>29</b>
3.1. Inner Tracking System . . . . .	31
3.2. Time Projection Chamber . . . . .	33
3.3. Time Of Flight Detector . . . . .	35
3.4. V0 Detector . . . . .	37
3.5. Additional Detectors . . . . .	37
3.6. ALICE Software . . . . .	38
3.6.1. Event and Track Reconstruction . . . . .	38
3.6.2. Simulation . . . . .	40
3.6.3. Analysis Tasks . . . . .	42
<b>4. Glauber Models</b>	<b>43</b>
4.1. Optical Glauber Model . . . . .	44
4.2. Monte Carlo Glauber Model . . . . .	45
4.3. Glauber Simulation for p-Pb Collisions with ALICE . . . . .	47
<b>5. Production of Pions, Kaons and Protons in p–Pb Collisions</b>	<b>49</b>
5.1. Particle Identification at Intermediate Transverse Momenta . . . . .	49
5.1.1. Event Selection . . . . .	50
5.1.2. Multiplicity Selection . . . . .	51

5.1.3.	Track Selection . . . . .	52
5.1.4.	Choice of Rapidity Range . . . . .	53
5.1.5.	Corrections . . . . .	54
5.1.6.	Monte Carlo Closure Test . . . . .	60
5.1.7.	Systematic Uncertainties . . . . .	62
5.2.	Other Particle Identification Methods Used in ALICE . . . . .	66
5.2.1.	ITS Standalone Analysis . . . . .	66
5.2.2.	Statistical Identification with TOF . . . . .	66
5.2.3.	Statistical Identification with TPC . . . . .	67
5.3.	Transverse Momentum Distributions of Pions, Kaons and Protons . . . . .	68
5.3.1.	Particle Ratios . . . . .	72
5.3.2.	Mean Transverse Momentum . . . . .	78
5.3.3.	Blast-Wave Fits . . . . .	78
5.3.4.	Nuclear Modification Factor of Pions, Kaons and Protons . . . . .	84
5.3.5.	Comparison with Model Calculations . . . . .	88
<b>6.</b>	<b>Production of Deuterons and Anti-Deuterons in p–Pb Collisions</b>	<b>91</b>
6.1.	Event and Track Selection . . . . .	91
6.1.1.	Momentum Correction . . . . .	94
6.2.	Monte Carlo Simulation . . . . .	95
6.3.	Particle Identification . . . . .	96
6.4.	Corrections . . . . .	97
6.4.1.	Absorption Correction . . . . .	98
6.4.2.	Tracking and Matching Efficiency . . . . .	100
6.4.3.	Secondary Correction . . . . .	101
6.5.	Systematic Uncertainties . . . . .	103
6.5.1.	Multiplicity Uncorrelated Uncertainties . . . . .	106
6.6.	Transverse Momentum Distributions of (Anti-)Deuterons . . . . .	106
6.6.1.	Anti-Deuteron to Deuteron Ratio . . . . .	109
6.6.2.	Mean Transverse Momentum . . . . .	110
6.7.	Deuteron Production Models . . . . .	111
6.7.1.	Deuteron to Proton Ratio . . . . .	111
6.7.2.	Coalescence Model . . . . .	113
6.7.3.	Thermal-Statistical Model . . . . .	115
<b>7.</b>	<b>Summary</b>	<b>121</b>
<b>A.</b>	<b>Kinematic Variables</b>	<b>127</b>
	<b>List of Figures</b>	<b>129</b>
	<b>List of Tables</b>	<b>131</b>



<b>Bibliography</b>	<b>133</b>
---------------------	------------



# 1. Motivation

Proton-lead (p-Pb) collisions at the *Large Hadron Collider* (LHC) and proton-nucleus collisions in general were originally motivated as a control experiment for heavy-ion collisions. Heavy-ion collisions at high energies on the other hand are a tool to create a quark-gluon plasma (QGP) phase in the laboratory. This is a phase of matter at extreme temperatures and densities, in which quarks and gluons are free [CP75b, CP75a]. To prove the existence of a QGP and to study it quantitatively, a comparison with elementary proton-proton (pp) collisions is necessary, because it is believed that no QGP is formed there. One missing piece of information to attribute potential differences to the QGP, comes with the assumption that heavy-ion collisions can be modeled as the superposition of independent pp collisions. However, the nucleons are bound in the heavy ion. This means that not all effects observed in heavy-ion collisions are necessarily a feature of the hot and dense QGP, but *cold nuclear matter effects* might also play a role.

Experimentally, cold nuclear effects matters are measured with collisions of a free proton with a lead ion at the LHC. Here it is assumed that a QGP cannot be formed and final-state effects are not present. The first measurements like the charged particle pseudo-rapidity density [ALICE13h] and the nuclear modification factor  $R_{pPb}$  [ALICE12b] are consistent with this expectation. However, long-range angular two-particle correlations (the so called *double ridge*) have been observed in high multiplicity p-Pb collisions [ALICE13e, CMS13b, ATLAS13b], which are reminiscent of the measurements in heavy-ion collisions. They revealed that p-Pb collisions might be subject to final-state collective effects, which would be in contradiction to the previous assumptions. To further investigate this possibility, different particle types are identified and the light-flavor hadron production is studied.

Within this thesis the transverse momentum distributions of  $\pi^\pm$ ,  $K^\pm$ , p,  $\bar{p}$ , d and  $\bar{d}$  as a function of multiplicity have been measured in p-Pb collisions at  $\sqrt{s_{NN}} = 5.02$  TeV

with ALICE at the LHC. ALICE stands for *A Large Ion Collider Experiment* and the primary goal of the collaboration is to explore the properties of the quark-gluon plasma with heavy-ion collisions. Still, smaller collision systems like pp and p-Pb are of particular interest, because they provide the baseline to study heavy-ion collisions.

The measurement of pions, kaons and protons contributes to the on-going discussion of possible collective effects in high multiplicity p-Pb collisions. Many interpretations of collectivity in heavy-ion collision are based on hydrodynamic models, which include radial flow, i.e. a velocity push of particles in radial direction from the pressure gradient of the hydrodynamically expanding fireball. Since a common pressure gradient introduces a mass-dependent momentum shift, the transverse momentum distributions of identified particles are a crucial contribution to the discussion of collectivity in high multiplicity p-Pb collisions.

The measurement of deuterons and anti-deuterons as a function of multiplicity in p-Pb events can give insight into the production mechanism of light nuclei in ultra-relativistic particle collisions. With ALICE, the deuteron production has already been measured in pp and Pb-Pb collisions [ALICE14f], where a qualitatively different behavior was observed for the abundance in the two collision systems. Because p-Pb collisions are intermediate in terms of multiplicity and system size, a transition in the production mechanism between the two systems can be revealed by the deuteron measurement.

This document is organized as follows: first, the theoretical and experimental basis of heavy-ion collisions and the quark-gluon plasma are established in Chapter 2. In the third chapter, the ALICE experiment and its excellent tracking and particle identification techniques are introduced. In the following chapter, the concept of Glauber calculations is discussed and a Monte Carlo Glauber model is used to calculate the number of binary nucleon-nucleon collisions in p-Pb. This allows to compare the obtained results to proton-proton collisions. The analysis technique used for pions, kaons and protons, the transverse momentum distributions and their comprehensive results are presented in Chapter 5. This part of the thesis, together with the transverse momentum distributions of  $K_S^0$  and  $\Lambda(\bar{\Lambda})$ , has already been published in [ALICE14h] and the chapter is largely based on the publication. Chapter 6 is dedicated to the measurement and interpretation of the transverse momentum distributions of deuterons and anti-deuterons. The deuteron production mechanism

---

is discussed within coalescence and thermal-statistical models. Finally, a summary of the most important results is given in Chapter 7. Within this thesis common kinematic variables for collider experiments are used. They are summarized in Appendix A.



## 2. Quarks, Gluons and the Strong Interaction

In this chapter, a brief introduction to the nature of the strong force and the corresponding well established theory *quantum chromodynamics* (QCD) will be given. In addition, some properties and experimental signatures of the quark-gluon plasma, which are relevant for this thesis, will be discussed.

The standard model of particle physics has proven to be very successful in describing the vast variety of particles produced in collider experiments. Within the model several particles have been predicted, which have been measured experimentally afterwards. The latest and widely known success was the measurement of a Higgs-like particle by the ATLAS and CMS collaborations at the LHC [ATLAS12a, CMS12a], which has been confirmed with a significance of more than  $5\sigma$  by now [ATLAS12b].

The standard model of particle physics constitutes twelve elementary particles. They are divided into six quarks (up, down, charm, strange, top and bottom) and six leptons (electron, muon, tauon and the corresponding neutrinos). In addition, each particle is accompanied by an anti-particle and three forces are defined, which are mediated by the gauge bosons. The electromagnetic gauge boson is the photon and the weak force is mediated by the  $W^\pm$  and  $Z^0$  bosons. The gauge bosons of the strong force are eight gluons, which will be discussed in the following section.

While neutrinos are only subject to the weak force, the other leptons and all quarks also carry a charge and interact electromagnetically. Quarks additionally carry a color charge, to which the strong force couples. Their properties and quantum numbers are summarized in Table 2.1.

The strong force is dominant at the subatomic level and the well established theory of quantum chromodynamics will be discussed in the following.

Name	Symbol	Charge ( $e$ )	$I_Z$	S	C	B	T	Mass ( $\text{GeV}/c^2$ )
up	u	$+2/3$	$+1/2$	0	0	0	0	$0.0023^{+0.0007}_{-0.0005}$
down	d	$-1/3$	$-1/2$	0	0	0	0	$0.0048^{+0.0005}_{-0.0003}$
strange	s	$-1/3$	0	-1	0	0	0	$0.095 \pm 0.005$
charm	c	$+2/3$	0	0	1	0	0	$1.275 \pm 0.025$
bottom	b	$-1/3$	0	0	0	-1	0	$4.180 \pm 0.03$
top	t	$+2/3$	0	0	0	0	1	$160^{+5}_{-4}$

Table 2.1.: Properties of the six quarks. Shown are the charge as multiple of  $e$ , the third component of the isospin  $I_Z$ , quantum numbers strangeness S, charmness C, bottomness B, topness T and the current quark masses. Data from [PDG12]

## 2.1. Quantum Chromodynamics

Since quantum chromodynamics have been discussed at length in several theses and reviews, only a short introduction is given here. For a full review please refer to [PDG12].

In addition to the electrical charge, quarks also carry a color charge to which the strong force couples. The color charge can be either red, green or blue for quarks and the corresponding anti-colors for anti-quarks. The force is mediated by eight gluons, which carry a color and an anti-color charge themselves, unlike the photon, which is the gauge boson of quantum electrodynamics (QED). The three colors give nine possible color anti-color combinations, but the color-neutral gluon is not realized in nature. QCD describes the strong force and is a non-Abelian gauge theory of the  $SU(3)$  symmetry group.

The strong force has two unique qualitative characteristics: *asymptotic freedom* and *color confinement*. The color confinement corresponds to the experimental observation that free color-charged particles do not exist and asymptotic freedom describes the weaker coupling of the strong force for higher momentum transfers  $Q$ .

To understand these two effects, one can compare the relative strengths of the strong force and the electromagnetical force with the coupling parameters. The coupling of QED varies only slightly. It is given by the fine structure constant  $\alpha \approx 1/137$  at zero squared momentum transfers  $Q^2$  and grows to  $1/128$  at  $Q^2 = m_W^2$ . On the other hand, the coupling  $\alpha_s$  of the strong force changes drastically with the momentum transfer.



This is called *running coupling* and in first order perturbative QCD the dependence of  $\alpha_s$  on the momentum transfer is given by:

$$\alpha_s(Q^2) = \frac{12\pi}{(33 - 2N_f) \cdot \ln(Q^2/\Lambda_{QCD}^2)}, \quad (2.1)$$

where  $N_f$  is the number of quark flavors, which are energetically accessible and  $\Lambda_{QCD}$  is the QCD scale parameter, which also depends on the number of flavors under consideration. For example, at LHC energies the five lightest quarks describe the relevant degrees of freedom and  $\Lambda_{QCD}^{(5)} = 213 \pm 8$  MeV. For this reason, the coupling is often reported for a given scale, which is usually the mass of the  $Z^0$  boson. The current world average is  $\alpha_s(m_{Z^0}) = 0.1184 \pm 0.0007$ . [Bet13]

A summary of the available measured data points of the strong coupling as a function of momentum transfer is shown in Fig. 2.1. The markers represent different measurements at different  $Q$  and the black line with the uncertainty band is a QCD

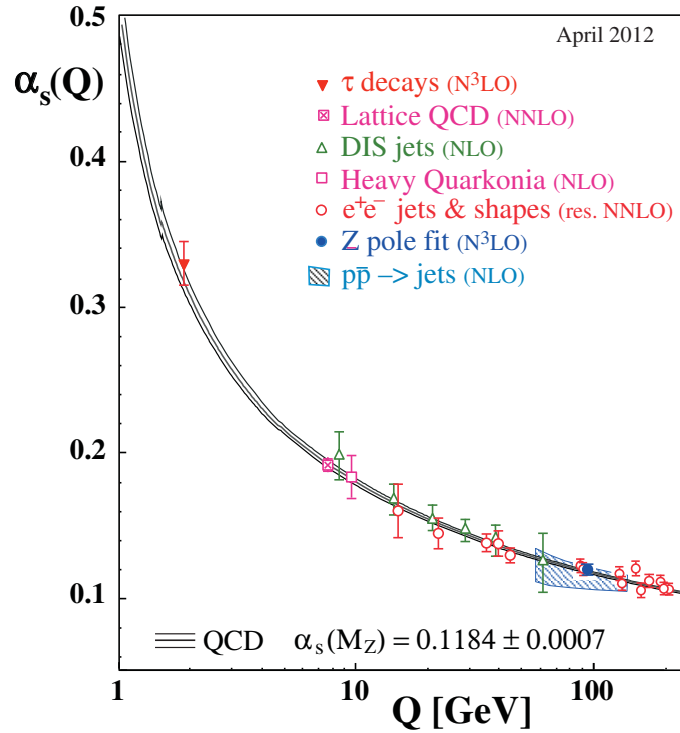


Fig. 2.1.: Summary of experimental results for the strong coupling  $\alpha_s$  as a function of the energy scale  $Q$ . In addition, the QCD calculation is shown with the line and uncertainty band. Figure from [Bet13].

calculation. While  $\alpha_S$  increases exponentially for low momentum transfers, the coupling becomes weaker for large momentum transfers and  $\alpha_S \rightarrow 0$  for  $Q^2 \rightarrow \infty$ , which corresponds to the asymptotic freedom of the strong force. The momentum transfer is related to the resolution with which structures can be probed. Figuratively speaking, large momentum transfers correspond to short distances or high resolutions.

The phenomenological potential of the strong force for two quarks is

$$V_S(r) = \frac{4}{3} \frac{\alpha_S}{r} + kr, \quad (2.2)$$

where  $r$  is the distance between the quarks [Per00]. The first term can be considered as a single gluon exchange term, analogous to the electromagnetical potential in QED. The second term accounts for the experimentally observed color confinement of particles, with the string tension  $k \approx 850$  MeV/fm. The potential energy increases with increasing distance  $r$  until the energy in the field is sufficient to create new quark anti-quark pairs to form color neutral objects. On the other hand, quarks and gluons, can move quasi-free for large momentum transfers, because the coupling is weak and for small distances the  $kr$ -term goes to zero.

These two regions also define the possible theoretical approaches. For small  $\alpha_S$  or high momentum transfers, where  $Q \gg \Lambda_{QCD}$  or  $\alpha_S \ll 1$  perturbative theories can be applied. However, they are not applicable for low momentum transfers and large  $\alpha_S$ . Here effective models or lattice QCD [Wil74] have to be used. The latter is a non-perturbative approach to solve QCD, which is formulated on a lattice of points in space and time.

In general, two types of particles are considered to form color neutral objects: mesons consist of a quark and an anti-quark and baryons contain three quarks or three anti-quarks, i.e. one of each color. However, other combinations like *tetraquarks* (two quarks and two anti-quarks) and *pentaquarks* (four quarks and one anti-quark) are theoretically possible to form color neutral objects. It is experimentally difficult to distinguish a bound state of four quarks from a bound state of two mesons, which form a meson molecule. However, at the time of writing this thesis two promising candidates of tetraquarks have been identified. One has been independently measured by the Belle collaboration and the BES III experiment [BESIII13, Belle13].

Another candidate, which has been reported by the Belle collaboration, has recently been confirmed by the LHCb collaboration [LHCb14].

## 2.2. Quark-Gluon Plasma

Although quarks and gluons are confined in color neutral particles under ordinary conditions, a phase of matter where quarks and gluons are free is predicted: the quark-gluon plasma (QGP). Analogous to a phase transition of ordinary matter from solid to liquid or from liquid to gas, this phase can be generated by adjusting the external parameters like temperature and density.

It is believed that the universe has been in this state shortly after the Big Bang until quarks and gluons hadronized at about  $10 \mu\text{s}$ . To investigate the QGP in the laboratory, ultra-relativistic heavy-ion collisions at accelerator facilities are an adequate tool. During the violent collisions energy densities can be reached, that are high enough to create a locally equilibrated system of free quarks and gluons. With the advent of more powerful colliders like the *Relativistic Heavy-Ion Collider* (RHIC) and the LHC, the QGP has successfully been observed in the laboratory. The QGP phase lasts for a few fm/c and can only be observed indirectly. Thus, several signatures of the QGP have been proposed in the last decades and some of them will be briefly introduced in Section 2.3.

The phase diagram of strongly interacting matter at these extreme temperatures and baryon densities is still a focus of the present research and the current knowledge is summarized in Fig. 2.2. The phase is shown as a function of temperature  $T$  and the baryo-chemical potential  $\mu_B$ , which accounts for the net-baryon density of the system.

The early universe is believed to have undergone a continuous cross-over transition at very low or zero  $\mu_B$  and at high temperatures. As shown in the phase diagram, the phase transition is at a critical temperature of about  $T_C \approx 160 \text{ MeV}$ , which can be calculated with the comparably simple bag model [CJJ<sup>+</sup>74]. A more sophisticated way are lattice QCD calculations, which also predict the continuous cross-over for lower  $\mu_B$ , while a first order phase transition with a clear separation of the phases is expected for higher  $\mu_B$  [AEF<sup>+</sup>06]. In case these expectations are correct, they also imply a critical point at intermediate  $\mu_B$ .

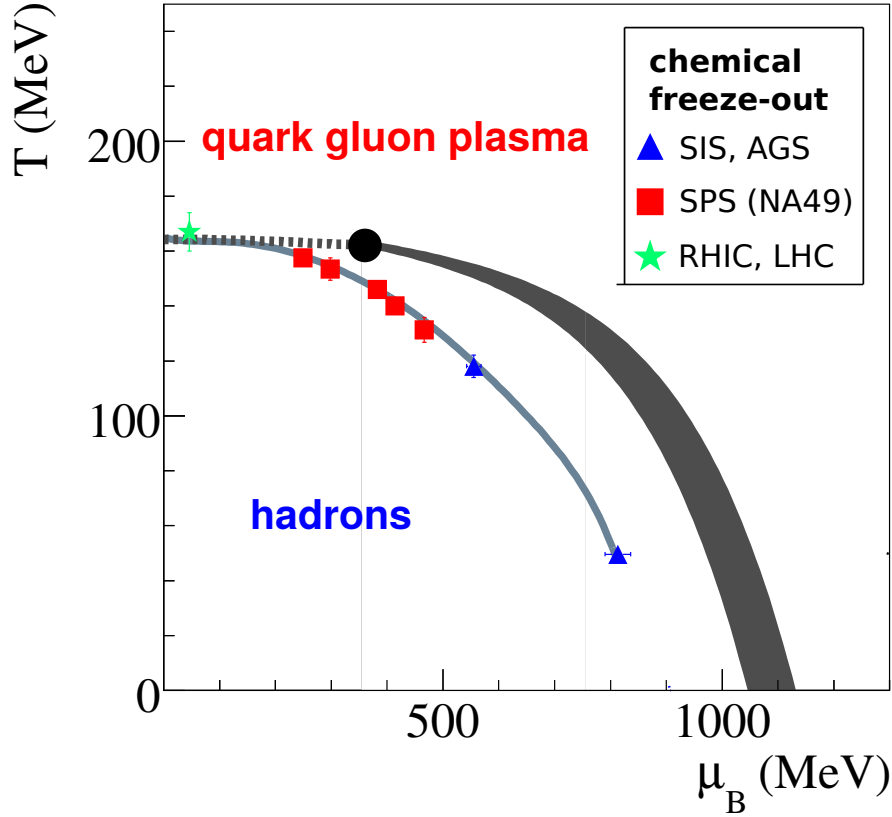


Fig. 2.2.: QCD phase diagram as a function of the temperature and the baryo-chemical potential  $\mu_B$ . The early universe is believed to have undergone hadronization at high temperatures and low  $\mu_B$ . The matter produced in Pb-Pb collisions at the LHC is believed to show a similar behavior. Colliders with lower energies explore the phase diagram rather at higher  $\mu_B$ . Their chemical freeze-out temperatures are below the QCD phase transition expectation. Figure based on [KSSS10].

The ALICE experiment at the LHC probes the same region of the phase space at very low  $\mu_B$  as the universe shortly after the Big Bang. For LHC and top RHIC energies the phase transition at the temperature  $T_C$  calculated with lattice QCD appears to be close to the chemical freeze-out temperature  $T_{ch}$  that marks the temperature at which all inelastic processes cease and the hadron chemistry is fixed. This temperature is experimentally accessible and can be determined by fitting the hadron yields with a thermal model (compare Section 6.7.3). The lower energies of the beam energy scan at RHIC and heavy-ion collisions at colliders with lower

center-of-mass energies like AGS and SPS have rather probed the phase diagram at higher baryo-chemical potentials and lower temperatures. Here, the chemical freeze-out temperatures are clearly below the expected critical temperatures of the phase transition.

The future experiment *Compressed Baryonic Matter* (CBM) at the planned FAIR facility at GSI will probe the phase boundary at higher  $\mu_B$  and will give new insights into the phase diagram of QCD. CBM and the beam energy scan at RHIC are also well suited to investigate the critical point in the phase diagram. This could be achieved by measuring e.g. event-by-event fluctuations of the net-proton multiplicity, which is expected to behave differently at the critical point of the phase diagram. Current results from the STAR collaboration are not yet conclusive [STAR14].

### 2.2.1. Space-Time Evolution of Ultra-Relativistic Particle Collisions

The geometry and space-time evolution of a heavy-ion collision is illustrated in Fig. 2.3. In the top panel two nuclei are shown before and after a collision, looking from a radial position. Due to the Lorentz contraction, the nuclei see each other as flat discs. The nucleons that take part in the collisions are called participants and form a hot and dense fireball, while the rest of the nuclei fly along the beam axis. These remaining nucleons are called spectators (cf. Chapter 4 on Glauber calculations).

In the Bjorken picture [Bjo83] the nucleons are transparent and penetrate each other. In the reaction zone a fireball emerges, which is mostly formed by the interaction of gluons and sea quarks, which dominate the nucleus at low  $x$  (cf. Section 2.4.3). This leads to a vanishing net-baryon density and a flat rapidity distribution at mid-rapidity. This picture is applicable for heavy-ion at LHC energies.

In the bottom panel of Fig. 2.3 the space-time evolution of a heavy-ion collision with the formation of a quark-gluon plasma phase is shown. After a pre-equilibrium phase, which presumably lasts less than 1 fm/c, a quark-gluon plasma exists for about 10 fm/c at LHC energies. As already discussed, the transition from the deconfined to the confined state is a smooth cross-over transition at low  $\mu_B$ . This is indicated by the critical temperature  $T_C$ , which could actually be a critical temperature range.

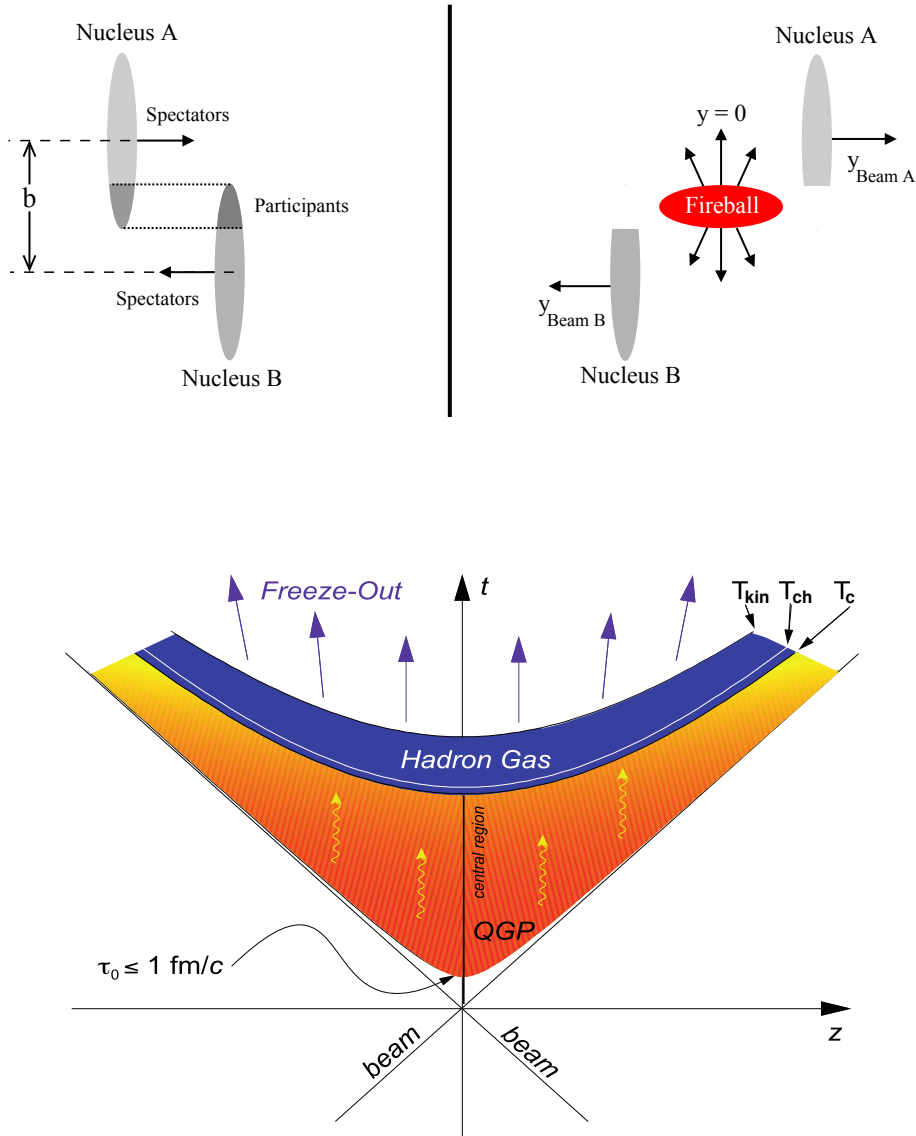


Fig. 2.3.: Two nuclei with impact parameter  $b$  before and after a collision (top). For heavy-ion collisions at LHC energies, the Bjorken picture of the space-time evolution is applicable. After the nuclei collide it takes less than  $1 \text{ fm}/c$  until a thermal equilibrium is reached and a quark-gluon plasma is created. The fireball then cools down quickly by expanding in space until the critical temperature  $T_C$  of the phase transition is reached after about  $10 \text{ fm}/c$ . The chemical freeze-out temperature  $T_{ch}$  found above top SPS energies coincides with the freeze-out curve calculated with lattice QCD. The momenta of the particle still change by elastic collisions until the kinetic freeze-out temperature  $T_{kin}$  is reached. Figures from [KB04] and [KSS10].

For LHC and RHIC energies this temperature is close to the chemical freeze-out temperature  $T_{ch}$ , where all inelastic processes cease and the hadron chemistry is fixed. The hadron gas cools further until the kinetic freeze-out temperature  $T_{kin}$  is reached. At this point all elastic processes cease and the momentum distributions of the particles are fixed.

The general expectation is that a QGP is not formed in p-Pb collisions, which means that this phase is skipped and the hadronic phase directly follows after the collision. However, some signatures, which have been attributed to the QGP in heavy-ion collisions, have been observed in high multiplicity p-Pb collisions and it remains unclear, if the assumption of absent hot matter effects in p-Pb collisions is valid. It is one of the objectives of this work to test some of the QGP signatures in p-Pb collisions.

## 2.3. Signatures of the QGP

Due to the confinement and the short lifetime of the quark-gluon plasma it is impossible to observe it directly in heavy-ion collisions. However, several signatures of the QGP have been proposed over the last decades, which have been more or less successful. A summary on the signatures is given in [BMS07b], for example. Here, only two characteristics or signatures of the QGP will be discussed. They can also be tested with the transverse momentum distributions of identified particles and are therefore of particular interest for this work:

1. Hydrodynamic behavior
2. Nuclear modification factor

The connection to the measurements presented in this work will be made and motivated by the results published so far.

### 2.3.1. Hydrodynamic Behavior

It has already been proposed by Bjorken in his famous publication [Bjo83] that the fireball created in ultra-relativistic heavy-ion collisions will exhibit hydrodynamic behavior and can be described as a relativistic fluid. A more recent introduction to hydrodynamics in heavy-ion collisions can be found in [Oll08].

A hydrodynamical description is only appropriate, when the single but strong requirement is met that the medium under consideration is in local thermal equilibrium. This implies that the mean free path of a particle in the medium is much smaller than all the characteristic dimensions of the system. In addition, ideal hydrodynamic models assume a viscosity of zero.

The hydrodynamical description is then provided by conservation laws of the momentum and energy

$$\partial_\mu T^{\mu\nu} = 0, \quad (2.3)$$

where  $T^{\mu\nu}$  is the relativistic energy-momentum tensor. In addition, the conservation of the baryon number current

$$\partial_\mu j_B^\mu(x) = 0 \quad (2.4)$$

is required. This gives in total five equations for six variables. Together with the *Equation of State* (EOS) of the fluid, which is usually calculated with lattice QCD in modern models, they form a closed system of equations. The EOS is a functional relation between the energy density  $\epsilon(x)$ , the momentum density  $p(x)$  and the baryon number density  $n_B(x)$ .

In the Bjorken model this is simplified by considering only the longitudinal expansion of the medium and assuming a net baryon density  $n_B = 0$ . To derive the equation of state two extreme cases are considered. At very low temperatures the system is described as a dilute pion gas and at very high temperatures as an ideal fluid of quarks and gluons and it follows:

$$p = \frac{\pi^2}{90} n(\beta) \beta^{-4}, \quad (2.5)$$

where  $\beta = 1/T$  and  $n$  is the number of degrees of freedom in the system, which depends on the phase under consideration. The equation of state can then be written as:

$$\frac{\epsilon}{3p} = 1 - \frac{\beta}{3n} \frac{\partial n}{\partial \beta}, \quad (2.6)$$



where  $n$  needs to satisfy  $\frac{\partial n}{\partial \beta} \leq 0$ . Please note that current state-of-the-art hydrodynamical models follow a much more sophisticated approach, but nevertheless, the general idea remains (cf. Section 5.3.5). In particular, they consider up to  $3 + 1$  dimensions on an event by event basis and introduce viscosity and thermal conductivity parameters to account for a non-perfect fluid. As in the Bjorken model, the degrees of freedom are usually encoded in the EOS to account for the partonic and hadronic phase. The transition from a hydrodynamic medium to free streaming particles can be performed within the *Cooper-Frye* formalism [CF74], which conserves energy or within the *cut-off* formalism [Bug96], which conserves the momentum in addition. For the remaining hadronic interactions transport models like UrQMD [BBB<sup>+</sup>98] can be used.

Please note that a hydrodynamic description is not limited to a QGP phase. For a proper hydrodynamic description, however, the mean free path needs to be much smaller than the characteristic dimensions of the system and a local equilibrium is required. While this requirement can be met easier by a strongly interacting QGP it may not be excluded that a hydrodynamic expansion is also applicable for a hot hadron gas created in particle collisions. However, comparisons of hydrodynamic models with measurements in heavy-ion collisions have shown that the existence of a partonic phase is strongly favored in order to describe the data [BRAHMS05b, PHENIX05, PHOBOS05].

The experimentally accessible observable for hydrodynamic behavior is *flow*, which is a common velocity field for all particles, due to the hydrodynamic expansion of the medium, which is induced by the pressure gradient. In case of central heavy-ion collision a symmetric fireball is expected and all particles receive a velocity push in transverse direction, regardless of their mass. This is usually called *radial flow* and manifests in the transverse momentum distributions of (identified) particles. The spectra are expected to become harder with respect to a collision without a hydrodynamic expansion, which means particles are pushed to higher momenta. In addition, a mass dependence is observed in the transverse momentum signal, because radial flow increases the particle velocity and not the momentum. The effect of radial flow increases for higher pressure gradients and longer hydrodynamic phases, which is usually correlated with the event multiplicity. In first order, the hardness of a spectrum can be measured by the mean transverse momentum  $\langle p_T \rangle$ . For heavy-ion

collisions a hardening of the spectra with centrality has been measured and a mass ordering has been observed at RHIC and at the LHC [STAR09, ALICE13b]. These measurements are generally interpreted as an effect of radial flow in the QGP phase. In p-Pb collisions a similar hardening of the spectra is observed, which might not necessarily be due to radial flow, but also questions if the interpretation of the data in heavy-ion collisions within the context of radial flow is correct. The possibility of hydrodynamic behavior in high multiplicity p-Pb collisions will be discussed with the transverse momentum distributions of identified hadrons in Section 5.3.

Another signature of the hydrodynamic expansion can be observed in non-central heavy-ion collisions. Here, the formed fireball is asymmetric and exhibits an *almond shape*. This results in different pressure gradients for different azimuthal angles with respect to the reaction plane<sup>1</sup>. While the mechanism of the velocity push is the same in this case, an azimuthal anisotropy of particle yields is observed in addition to the hardening. This is called *elliptic flow* and a recent review can be found in [Sne11]. The anisotropy of the particle emission is usually described with a Fourier expansion of the particle production with respect to the reaction plane:

$$E \frac{d^3N}{d^3\mathbf{p}} = \frac{1}{2\pi} \frac{d^3N}{p_T dp_T dy} \left( 1 + \sum_{n=1}^{\infty} v_n \cos[n(\varphi - \Phi_{RP})] \right), \quad (2.7)$$

where  $E$  is the energy of the particle,  $\varphi$  the azimuthal angle of the particle and  $\Phi_{RP}$  the angle of the reaction plane.

The magnitude of the corresponding harmonic is described with the Fourier coefficients  $v_n$ , e.g.  $v_2$  for elliptic flow. It is an established probe in heavy-ion collisions and has been measured at AGS, SPS, RHIC and the LHC. The measurement of elliptic flow of identified particles at RHIC revealed a clear mass ordering, which is in agreement with predictions from an ideal fluid [Sne11]. ALICE has recently published elliptic flow results in Pb-Pb collisions for identified particles that also show the typical mass ordering [ALICE14e]. Higher harmonics like  $v_3$ , i.e. triangular flow, have also been measured and are generally interpreted as fluctuations in the initial stage [AR10].

Elliptic flow is also visible in two-particle correlation studies, which do not require the definition of an event plane. All three experiments at LHC with a heavy-ion

---

<sup>1</sup>The reaction plane is defined by the two shorter axes of the ellipsoid.

program published results of these studies for unidentified charged particles in p-Pb collisions. They revealed a double ridge structure and a significant  $v_2$  (and  $v_3$ ) has been measured [ALICE13e, CMS13b, ATLAS13b]. PHENIX has also published compatible results for d-Au collisions at RHIC [PHENIX13a].

Transverse momentum distributions of identified particles are not directly sensitive to elliptic flow, but the PID techniques and calibration used for the identified particle spectra have also been used to measure two-particle correlations of identified particles [ALICE13d]. In Fig. 2.4 the Fourier coefficient  $v_2$  is shown for pions, kaons and protons measured in p-Pb collisions. It was obtained with two-particle correlations and to enhance the visibility of the effect the jet contribution was removed by subtracting the signal of low multiplicity events from the signal of high multiplicity events. The typical mass ordering observed in heavy-ion collisions is also seen for p-Pb collisions. Please note that the magnitude of  $v_2$  is smaller compared to heavy-ion collisions [ALICE14e], but nevertheless, given these results, the interpretation of the heavy-ion results in the context of flow will have to be handled with more caution.

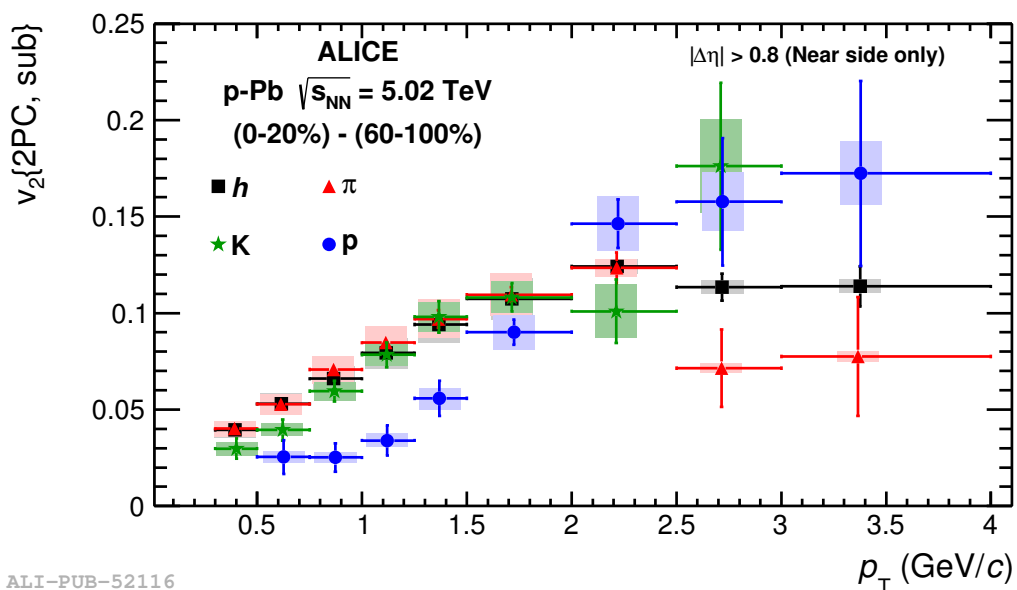


Fig. 2.4.: The Fourier coefficient  $v_2$  of identified particles measured with two-particle correlations. To enhance the visibility of the effect, the signal of low multiplicity events has been subtracted from the signal of high multiplicity events. The resulting  $v_2$  shows a clear mass ordering, which is reminiscent of the behavior in Pb-Pb collisions. Figure from [ALICE13d].

On the other hand, one can argue that these results add another question mark to the paradigm that no hot matter effects are present in p-Pb (d-Au) collisions.

### 2.3.2. Nuclear Modification Factor

While hydrodynamic effects can influence the transverse momentum distributions and particle correlations at low to intermediate momenta ( $p_T < 5 \text{ GeV}/c$ ), other effects become important for the high momentum part, which is connected to hard processes. For a high momentum parton, which originates from a hard nucleon-nucleon collision and which escapes the collision region, a qualitative difference arises for proton-proton and heavy-ion collisions. Since the reaction zone of the pp collision is small, the parton can escape and hadronize without further interaction. In case of heavy-ion collisions, the parton has to traverse the quark-gluon plasma, which is much larger than the average mean free path. Analogous to Bremsstrahlung of charged particles, color-charged partons could emit gluons in the color charge field of other partons. This would lead to a significant decrease of the parton energy and the momentum of the leading hadron in the parton fragmentation.

Experimentally this behavior should be observable as a suppression of high  $p_T$  particles, when comparing heavy-ion collisions to pp collisions. To compare the two systems, the nuclear modification factor  $R_{AA}$  is defined as the particle production in a heavy-ion collision divided by the particle production in pp collisions at the same energy  $\sqrt{s_{NN}}$ , scaled with the average number of binary collisions  $N_{coll}$  in the heavy-ion collision (cf. Formula 5.8).

To obtain the mean number of nucleon-nucleon collisions for heavy-ion collisions, Glauber models are used. They will be described and used for p-Pb collisions in Chapter 4. If a quark-gluon plasma is formed, the nuclear modification factor is expected to be smaller than unity in the high  $p_T$  region, where the particle production is governed by hard processes and the scaling with the number of binary collisions is appropriate.

Several results have been published on the nuclear modification factor  $R_{AA}$  and a clear suppression of high  $p_T$  particles is seen in Au-Au collisions at RHIC [PHENIX01, STAR02] and in Pb-Pb collisions at the LHC [ALICE13a, CMS12c]. In Fig. 2.5 some recent measurements are summarized to illustrate the current knowledge. The  $R_{PbPb}$  measurements from ALICE and CMS for the 0-5% most central

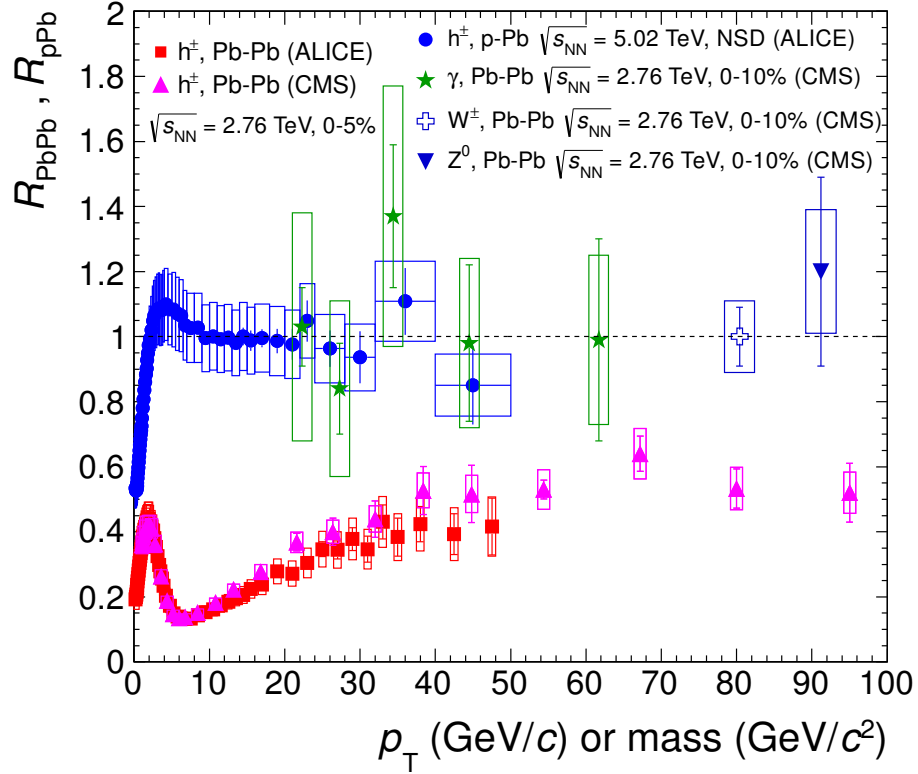


Fig. 2.5.: The nuclear modification factor for charged hadrons for Pb-Pb collisions from ALICE [ALICE13a] and CMS [CMS12c] and for p-Pb collisions from ALICE [ALICE14b]. For Pb-Pb a clear suppression is seen, which is attributed to the interaction of partons with the QGP created in heavy-ion collisions. The nuclear modification factor of p-Pb collisions is compatible with unity for high  $p_T$ , but shows an small enhancement at intermediate  $p_T$ . Also shown is the  $R_{\text{PbPb}}$  of  $W^\pm$  [CMS12e] and  $Z^0$  [CMS11b] bosons and direct photons [CMS12b]. They do not interact strongly with the QGP and do not show any suppression. Figure from [ALICE14b].

Pb-Pb events at the LHC are in very good agreement and show a suppression over the whole  $p_T$  range. The structures at low to intermediate  $p_T$  are due to soft processes and initial state effects. Furthermore, the scaling with the number of binary collisions, i.e. scaling with hard processes, is not expected to work in this region. The suppression at high  $p_T$  is in general interpreted as an effect of the quark-gluon plasma, which has a high color charge density and slows partons through strong interactions.

The argument of the presence of strongly interacting matter is further substantiated by the nuclear modification factors of  $W^\pm$  and  $Z^0$  bosons and direct photons measured with CMS. They do not interact strongly and show thus no suppression, but are compatible with unity. This also confirms that the scaling with the number of binary collisions is adequate at high  $p_T$ .

Analogous to the suppression of high  $p_T$  particles, a suppression of *jets* in heavy-ion collisions has been measured at RHIC [PHENIX04a, STAR03b] and the LHC [CMS11a, ATLAS13a, ALICE14a], which is substantial up to 210 GeV/ $c$ . A jet consists of the fragmentation products of a high  $p_T$  parton, that has undergone a hard collision. This means not only the leading high  $p_T$  particle is measured, but also the hadronized fragmentation products. Please note that a jet is a not very well defined object and measurements may depend on the jet definition. However, the measured suppression factors are consistent with the suppression of single high  $p_T$  particles, which leads to the conclusion that the energy is radiated outside of the jet cone.

For p-Pb collisions, the situation looks qualitatively different. The nuclear modification factor  $R_{pPb}$  of charged hadrons is compatible with unity at high  $p_T$ . It needs to be noted that the volume of the possible fireball created in p-Pb collisions is much smaller than in heavy-ion collisions and particles have to traverse less matter. Nevertheless, the consistency of  $R_{pPb}$  with unity suggest the absence of a quark-gluon plasma in minimum bias p-Pb collisions. In addition, the results underline that the suppression in heavy-ion collisions is not an initial-state effect, but rather a final-state effect. At intermediate  $p_T$  (2-7 GeV/ $c$ ) an enhancement is visible, which is commonly labeled *Cronin peak* and will be discussed in Section 2.4. Please note that within the full systematic uncertainties the factor is also compatible with unity in this region. However, systematic uncertainties are largely correlated across  $p_T$ -bins.

CMS has also shown preliminary data of the nuclear modification factor, which rises up to values of  $R_{pPb} \approx 1.5$  for  $p_T > 30$  GeV/ $c$  [CMS13a]. This  $p_T$  region could be affected by anti-shadowing (cf. Section 2.4.2), but for the commonly used nuclear parton density function EPS09 this effect would only amount to a few percent [HEHS12]. ATLAS has recently shown preliminary results of  $R_{pPb}$ , that are consistent with the CMS measurement [ATL14b]. The results from ALICE are compatible with the measurements from d-Au collisions at RHIC, where no suppression at high

$p_T$  was found [STAR03a, CMS12e]. However, an enhancement of  $R_{dAu}$  at intermediate  $p_T$  was observed, which is in qualitative agreement with  $R_{pPb}$  at the LHC. Please note that the enhancement in p-Pb is not as pronounced as in d-Au.

The CMS and ATLAS results appear to be in contradiction with the ALICE results, especially, since the last bin in the ALICE data might suggest a different trend. However, one has to keep in mind that the uncertainties correspond to only  $1\sigma$  and in this sense, the results are not incompatible. This is in particular the case, when directly comparing the measured spectra of all charged particles in p-Pb. The differences in the nuclear modification factor are mainly generated by the interpolated pp reference and a measurement of the charged particle production in pp collisions at  $\sqrt{s} = 5.02$  TeV is much needed. It needs to be noted that all three experiments have measured a nuclear modification factor of jets in p-Pb, which is compatible with unity over the full  $p_T$  range up to 1000 GeV/ $c$  in minimum bias collisions [CMS14a, ATL14a, ALICE13j].

Within this work, the low and intermediate  $p_T$  region, where the enhanced particle production with respect to the scaled pp reference is observed, is studied. The  $R_{pPb}$  of pions, kaons and protons has been measured, which can shed more light into the nature of the Cronin peak (cf. Section 5.3.4).

## 2.4. Cold Nuclear Matter Effects

In the Glauber picture, a heavy-ion collision can be considered as the superposition of independent nucleon-nucleon collisions and the comparison with pp collisions can reveal effects of the QGP. However, *cold nuclear matter effects* can also modify the particle production with respect to a simple superposition, because the nucleons are bound and interact with each other. In this section a brief introduction to the commonly described effects will be given.

### 2.4.1. Cronin Effect

The Cronin effect is an enhanced particle production at low to intermediate transverse momenta  $p_T$  in proton-nucleus collisions with respect to the scaled particle production in proton-proton collisions. It has been observed first in the 70s by a

group around Cronin [CFS<sup>+</sup>73, ACF<sup>+</sup>79], after whom the Cronin effect or Cronin peak is named. They investigated the particle production of a 200 GeV – 400 GeV proton beam on different nuclei targets and found that the particle production cross-section scales with a power-law  $A^\alpha$ , where  $A$  is the nucleon number of the nucleus and  $\alpha$  is obtained by a fit to the data. Fig 2.6 shows  $\alpha$  as a function of transverse momentum, where  $\alpha > 1$  corresponds to an enhanced particle production with respect to lighter nuclei.

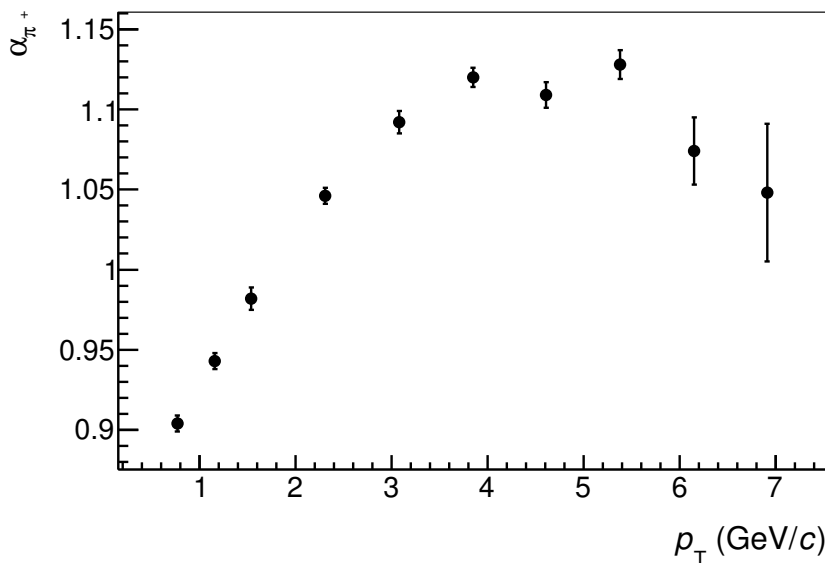


Fig. 2.6.: The power-law exponent  $\alpha$  as a function of  $p_T$  for positive pions. The production cross-section scales with  $A^\alpha$ , where  $A$  is the number of nucleons in the nucleus. For  $p_T > 2$  GeV/ $c$   $\alpha$  is above unity, which indicates an enhanced particle production with respect to smaller nuclei. These results have been obtained with a 400 GeV proton beam on different nuclear targets. Data from [ACF<sup>+</sup>79].

The effect is commonly explained by multiple scattering of the proton, which results in momentum fluctuations and increased particle momenta on average. A review of models that describe the Cronin effect as an initial state effect due to multiple scattering can be found in [Acc02]. Another theoretical approach is laid out in [HY04], where the Cronin effect is explained as a final state effect within the recombination model [DH77]. The explanation of the enhanced particle production remains an open issue.



More recently, a Cronin peak has been observed in the nuclear modification factor  $R_{\text{dAu}}$  of the proton transverse momenta distributions in d-Au collisions at RHIC [STAR06, PHENIX13b] and in p-Pb collisions at the LHC [ALICE14b]. Within this thesis this behavior is further investigated by measuring the nuclear modification factor of pions, kaons and protons. Please refer to Section 5.3.4.

### 2.4.2. Shadowing, Anti-Shadowing and EMC Effect

In this section the modification of the parton density in nuclei with respect to the superposition of nucleons will be discussed. This is important, because the particle production is naturally sensitive to the number of scattering centers in the nucleus. In the most simple approach one could assume a scaling with the number of bound nucleons  $A$ . However, measurements of the structure functions  $F_2$  of nuclei have shown that the scaling with  $A$  is only an approximation. A common way to measure these effects is to compare  $F_2$  of a nucleus with  $F_2$  of deuterium, where the  $F_2$  are normalized by  $A$ . This gives the nuclear modification factor  $R_{F_2}^A$ . A direct comparison with nucleons is not as advantageous, because nuclei contain protons and neutrons and deuterium is the smallest isospin-averaged system. It is hence a good baseline for nuclei which contain a similar number of protons and neutrons. The structure function  $F_2$  can be translated to the charge distribution and is used to calculate (nuclear) parton density function. It is therefore directly connected to the particle production in heavy-ion and proton-nucleus collisions.

Structure functions have been measured extensively with deep inelastic scattering (DIS) of leptons off nuclei at several accelerator facilities. The nuclear modification of  $F_2$  was first measured by the EMC collaboration at intermediate Bjorken  $x$ , which resulted in the name of the *EMC effect* [EMC83]. Here,  $x$  is a dimensionless variable and corresponds to the momentum fraction of the nucleon, that is carried by a parton. A review of the nuclear modification of structure functions can be found in [Arn94].

In Fig. 2.7 a schematic graph of the different regions of nuclear modification with respect to the deuterium  $F_2$  as a function of Bjorken  $x$  is shown. The magnitude and to some extent the position in  $x$  depends on the nucleus under consideration and the squared momentum transfer  $Q^2$ , but the qualitative statement is universal.

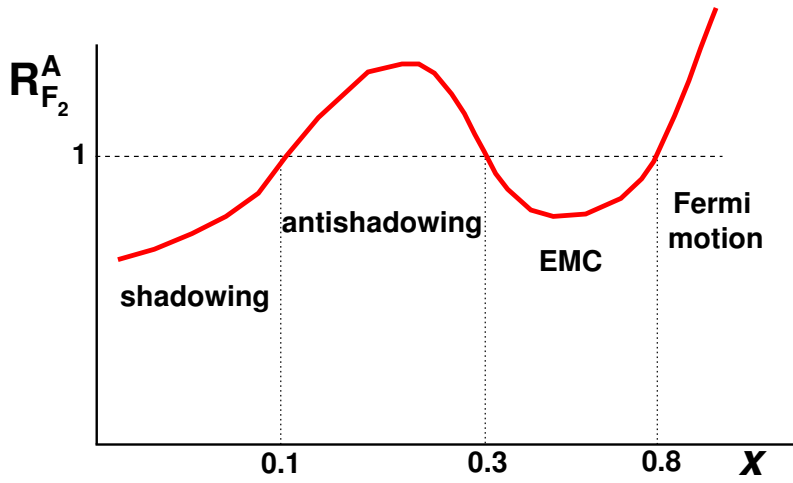


Fig. 2.7.: Sketch of the structure function of nucleus A normalized to scaled deuterium structure function as a function of Bjorken  $x$ . Figure from [Arm06].

The region at very low  $x < 0.1$  exhibits a  $R_{F_2}^A$  below unity and is called *shadowing* region. In the context of DIS experiments, shadowing is commonly explained by a fluctuation of the virtual photon, which is exchanged between the electron and the nucleon, into a superposition of vector mesons, which then interacts strongly with a nucleon on the surface of the nucleus. This nucleon is most relevant for the interaction and shadows the nucleons behind it. The cross-section per nucleon is thus smaller than for free nucleons. The effect is most relevant at low  $x$ , where the lifetime of the fluctuation is comparable to the distance of the nucleons in the nucleus. Another theoretical approach is the interaction and fusion of partons in the nucleus. This will be discussed within the context of the *Color Glass Condensate* in Section 2.4.3. At low to intermediate  $x$  (0.1 - 0.3) an increase above unity of the structure function in nuclei with respect to deuterium is observed. This region is analogously called *anti-shadowing* and would be a direct consequence of the parton fusion model.

The EMC effect dominates the region of  $0.3 < x < 0.8$ . An attempt to explain this depletion with conventional physics is an excess of virtual pions, which are associated with the nuclear force. These virtual pions represent additional scattering centers at

lower  $x$  and effectively reduce the carried momentum fraction of the partons. Thus the  $x$  distribution is softened.

As  $x$  approaches unity, the Fermi motion of the nucleons within the nuclei becomes most relevant and causes a steep increase in  $R_{F_2}^A$ . In summary, several theoretical approaches have been proposed for the different  $x$  regions and the interested reader is referred to [Arn94], which contains a theoretical overview, but also an experimental review.

The discussed effects may also be connected to the particle production in p-A or A-A collisions. In general, a  $R_{F_2}^A$  above unity indicates more scattering centers and hence an increased particle production in ultra-relativistic A-A or p-A collisions. For regions of  $x$  with a  $R_{F_2}^A$  below unity a decreased particle production would be expected. Depending on the collision energy per nucleon-pair, the relevant  $p_T$  ranges can be estimated by

$$x \approx \frac{2p_T}{\sqrt{s_{NN}}}, \quad (2.8)$$

when assuming that most of the momentum of a hard parton scattering is carried away by the leading hadron.

### 2.4.3. Gluon Saturation – Color Glass Condensate

The parton distributions of nucleons have been measured with high precision as a function of  $x$  and  $Q^2$ . In Fig. 2.8 fit results from the ZEUS collaboration are shown for deep inelastic scattering of leptons off protons with  $Q^2 = 10 \text{ GeV}^2$ . Shown are the distributions of up and down flavor, which are the valence quarks of the proton, but also the gluon and the sea quark distribution. Please note that the sea quark distribution cannot be measured directly, but can be obtained by comparing DIS results of charged leptons and neutrinos. The gluon distributions can be obtained by solving the DGLAP equations [GL72, ZEUS03], which in return give the gluon and quark momentum distributions and thus the structure function  $F_2$ .

At higher  $x$  the valence quarks clearly dominate and have a maximum at  $x \approx 0.2$ . The up quark distribution is naturally higher since the proton contains two of them and only one down quark. At lower  $x$  the valence quarks of the proton are clearly dominated by sea quarks and especially gluons. Please note that the sea quark and

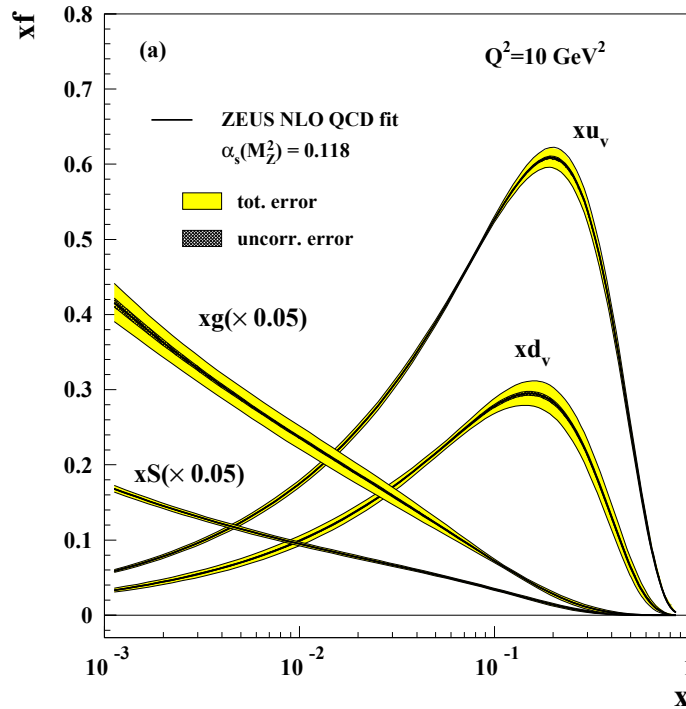


Fig. 2.8.: Flavor distributions  $x f$  of a proton at  $Q^2 = 10 \text{ GeV}^2$  as a function of  $x$  calculated by ZEUS with deep inelastic scattering. At high  $x$  the valence quarks dominate and reach a maximum at  $x \approx 0.2$ . At low  $x$  sea quarks and gluons clearly dominate the valence quarks, while gluons dominate the sea quarks. Please note that the gluon and sea quark distributions have been scaled by a factor of 0.05 for visibility. Figure from [ZEUS03].

gluon distributions have been scaled by a factor 0.05 for visibility. Within the measured  $x$  range the gluon distribution is rising steadily. In addition to  $Q = 10 \text{ GeV}^2$  the gluon distribution has also been calculated at  $Q^2 = 7, 200$  and  $2000 \text{ GeV}^2$ , which is shown in Fig. 2.9. The extreme gluon densities at low  $x$  are even more dominant for higher momentum transfers. This means that at higher nucleon-nucleon energy  $\sqrt{s_{\text{NN}}}$  at particle colliders like the LHC, the particle production is mostly governed by low  $x$  gluons.

However, the phase space in the nucleon is limited and the gluon distribution is expected not to grow to infinity. This has led to the proposal of a new state of matter: the *color glass condensate* (CGC). It could exist in nuclei, which are almost at the speed of light and highly Lorentz contracted. The basic idea is that at high enough densities gluons overlap and interact with each other. In particular, two gluons can

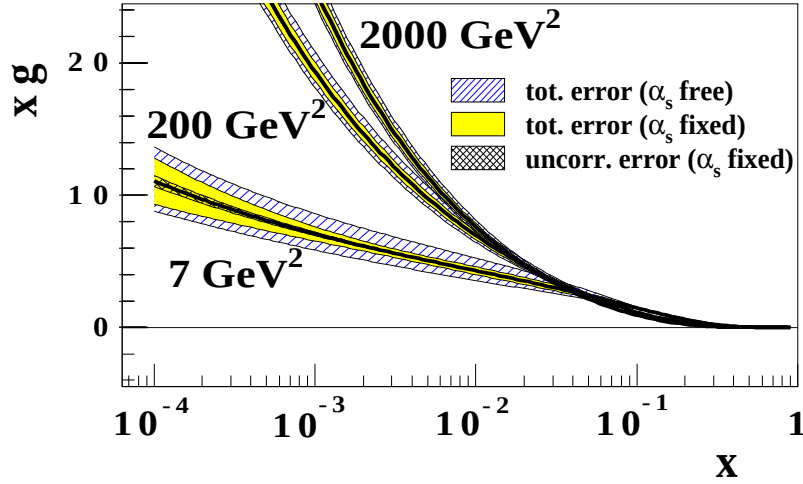


Fig. 2.9.: Gluon distributions  $xg$  at different  $Q^2$  as a function of  $x$  calculated with ZEUS deep inelastic scattering data. For higher momentum transfers the dominance of the gluons is even more pronounced and becomes relevant at higher  $x$ . Figure based on [ZEUS03].

fuse to a single gluon, which is an effect not considered in the DGLAP evolutions. When taking it into account, the gluon density is limited and the saturation scale  $Q_S$  for a nucleus with nucleon number  $A$  is defined as:

$$Q_S^2 \propto \alpha_S(Q_S^2) \frac{xg_A(x, Q_S^2)}{\pi R_A^2}, \quad (2.9)$$

where  $R_A$  is the nuclear radius and  $g_A(x, Q_S^2)$  the gluon distribution in the nucleus, which can be approximated with the nucleon gluon distribution  $g(x, Q_S^2)$ :

$$g_A(x, Q_S^2) \approx g(x, Q_S^2) \cdot A. \quad (2.10)$$

Since the radius of the nucleus scales with  $A^{1/3}$ , the CGC is more important in heavy nuclei and could play a crucial role for the initial conditions of p-A and A-A collisions. In measurements the CGC would manifest in a lower particle production rate. It is also a potential explanation for the shadowing measured for nuclear structure functions. A review of the CGC can be found in [IV03].



### 3. The ALICE Experiment

The ALICE experiment is one of four large experiments at the LHC and is designed to investigate the properties of the strong interaction in heavy-ion collisions. The LHC at CERN is located about 100 m underground of the Swiss-French border by Geneva and has a circumference of 27 km. It has reached unprecedented energies of  $\sqrt{s} = 8$  TeV in pp,  $\sqrt{s_{NN}} = 2.76$  TeV in Pb-Pb and  $\sqrt{s_{NN}} = 5.02$  TeV in p-Pb collisions since its start in 2008. After the current maintenance shutdown it will resume operation with pp collisions in 2015 with the full design energy of  $\sqrt{s} = 14$  TeV. For a detailed description and performance please refer to [BCL<sup>+</sup>04, EB08, AF<sup>+</sup>13].

The key feature of the ALICE detector is that it can cope with the immense particle multiplicities of heavy-ion collisions, where the multiplicity is commonly stated as the number of charged particles per unit of pseudo-rapidity  $dN_{ch}/d\eta$ . While ALICE was designed for the most extreme multiplicity extrapolation  $dN_{ch}/d\eta \approx 8000$  from SPS heavy-ion collisions, the particle production in the most central Pb-Pb collisions reaches  $dN_{ch}/d\eta \approx 1600$  [ALICE11a]. In addition, ALICE has excellent vertexing and tracking capabilities from  $p_T > 100$  MeV/ $c$  up to high momenta and superior particle identification (PID) capabilities with several techniques.

Fig. 3.1 shows a sketch of the ALICE detector. The beam setup for the data used in this thesis is indicated with the two black arrows. Here, the protons come in from the A-side and the lead ions from the C-side. By convention, the positive direction of the  $z$ -axis points towards the proton-going direction and thus positive rapidities are on the C-side.

The ALICE detector consists of the muon spectrometer and the central barrel. The muon arm is at forward rapidities and is mainly used to detect muon pairs stemming from light and heavy vector-mesons, but also single muons from heavy-flavor hadrons and  $W^\pm$  bosons. It is not used for the analysis performed within this thesis and the

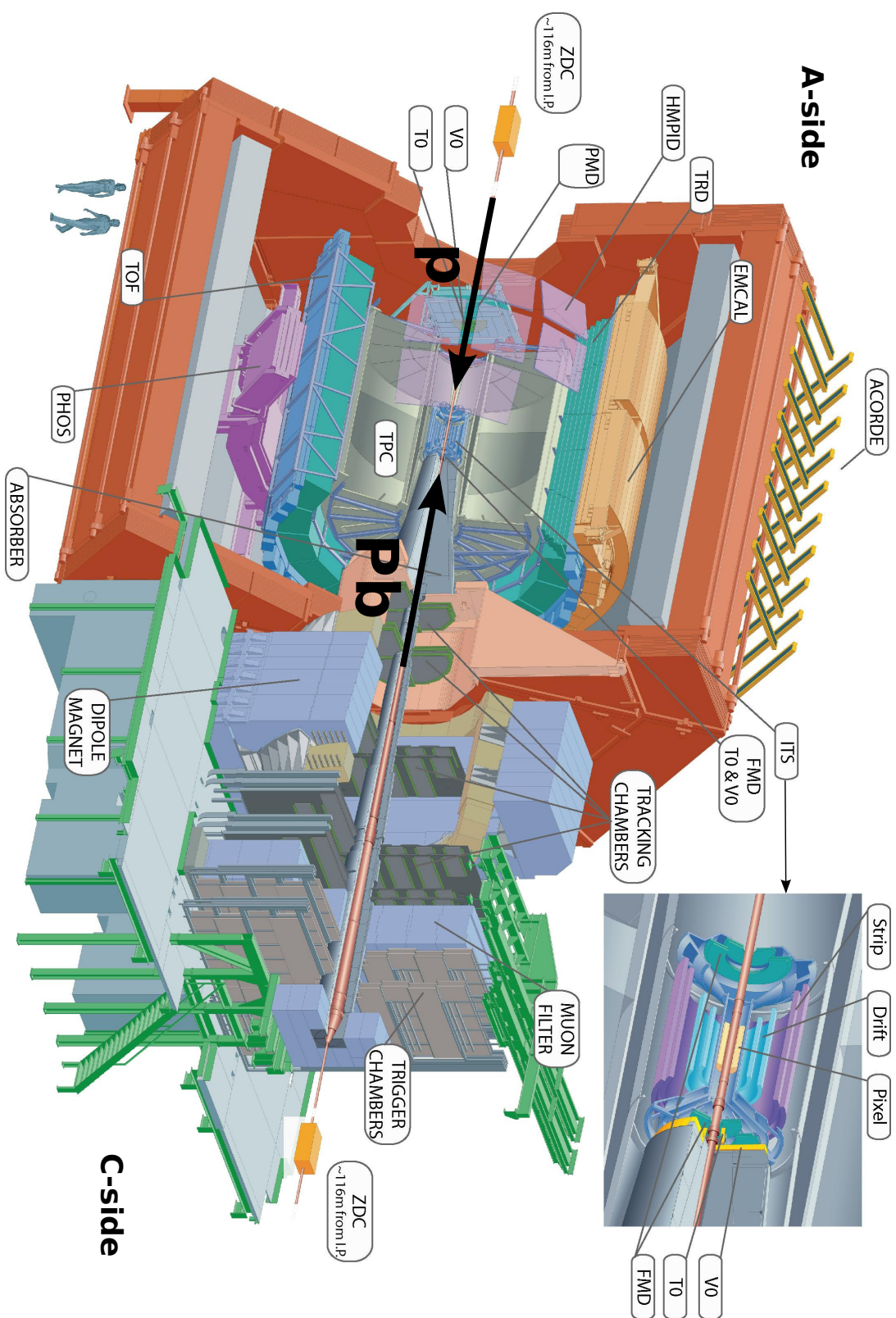


Fig. 3.1.: Sketch of the ALICE detector. Please refer to text for details.



interested reader is referred to [ALICE08]. The central barrel, which is symmetric around the interaction point is embedded in the homogeneous magnetic field of 0.5 T from the L3 magnet (red). In the following sections the sub-detectors in the central barrel, which are most relevant for the analysis in this work will be introduced briefly. For a detailed description of the experiment and the sub-detectors please refer to [ALICE04, ALICE06, ALICE08].

In addition to the central barrel and the muon spectrometer, two *Zero Degree Calorimeters* (ZDC) are installed 116 m from the interaction point at each side of the detector. Each consists of a neutron calorimeter ZNA (ZNC) and a proton calorimeter ZPA (ZPC), which measure the remnants of the colliding nuclei. These signals can not only be used to measure the centrality of the collision, but the arrival time of the nucleons is also used to reduce the background of beam-gas and gas-gas collisions.

During the 2013 p-Pb run the LHC was operated with up to 338 colliding bunches at the ALICE interaction point with a bunch spacing of 200 ns. The mean number of collisions per bunch crossing was required to be  $< 0.05$  to avoid pileup events from the same bunches. This has led to an interaction rate of about 10 kHz of minimum bias collisions. A recent report with details on the running conditions and detector performance can be found in [ALICE14i].

### 3.1. Inner Tracking System

The Inner Tracking System (ITS) is directly located around the interaction region and is shown in the inlay on the top right of Fig. 3.1. It consists of six layers of silicon detectors, with three different technologies: the two innermost are pixel detectors (SPD), then two silicon drift detectors (SDD) and finally two silicon strip detectors (SSD). They cover the full azimuth and  $|\eta| < 0.9$  or more. In particular, SPD layer 1 covers  $|\eta| < 2.0$  and layer 2 covers  $|\eta| < 1.4$ , while both SSD layers cover  $|\eta| < 1.0$ . The ITS is used to reconstruct the primary interaction vertex, but also secondary vertices to allow the identification of quickly decaying particles like D-mesons ( $c\tau(D^\pm) = 311.8 \mu\text{m}$  [PDG12]). In addition, it contributes to the tracking of particles and increases the resolution of the Distance of Closest Approach (DCA) to the vertex with respect to the rather rough approximation of the *Time Projection*

### 3. The ALICE Experiment

*Chamber* (TPC). For tracks with  $p_T > 0.2$  GeV/ $c$  the resolution in the  $xy$ -plane is better than  $170 \mu\text{m}$  and improves down to  $20 \mu\text{m}$  for  $p_T > 10$  GeV/ $c$  in p-Pb collisions [ALICE14i]. Within this thesis this precision is extremely beneficial for the secondary particle subtraction method performed in Sections 5.1.5 and 6.2. With the ITS it is also possible to reconstruct tracks of particles with momenta down to approximately 100 MeV/ $c$ , which do not reach the TPC.

Furthermore, the four outer layers of the ITS, i.e. SDD and SSD, also record the deposited energy per length  $dE/dx$  in silicon. This information can be used to identify those particles that do not reach the TPC and extends the particle identification capabilities of ALICE to lower momenta. This reduces the extrapolation of transverse momentum distributions to lower momenta for the integrated particle yields and thus the systematic uncertainties.

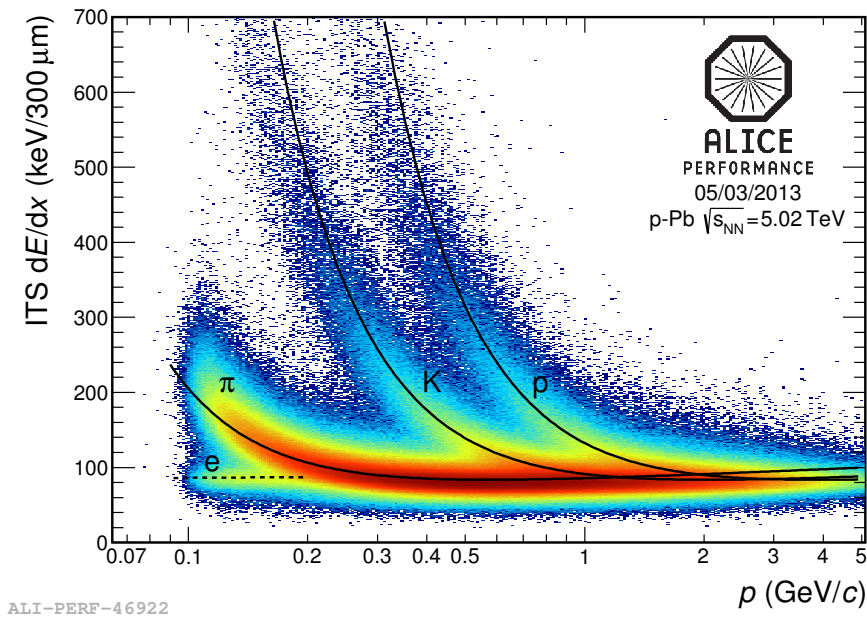


Fig. 3.2.: ITS PID performance in p-Pb collisions. Plotted is the energy loss as a function of the particle momentum. The black lines indicate the parametrizations.

The accessible  $p_T$  range of the particle identification with the ITS gives some overlap with the TPC PID at higher  $p_T$  ( $\approx 300$ – $700$  MeV/ $c$ ) and allows the validation of both methods. This is in particular beneficial, because the ITS PID method uses only the ITS information for the tracking and is in this way independent. Fig. 3.2

shows the performance of the PID with the ITS in p-Pb collisions when combining the four  $dE/dx$  samples. A clean separation is possible at low  $p_T$ . The black lines are the parametrizations for the corresponding particles.

The ITS can also provide a fast trigger signal and is used for the minimum bias trigger in Pb-Pb collisions. For a more detailed description of the ITS design and its performance please refer to [ALICE99, ALICE14i].

## 3.2. Time Projection Chamber

The Time Projection Chamber [AAA<sup>+</sup>10] is the main tracking device of ALICE and is shown in gray in Fig. 3.1. It is build symmetrically around the ITS covering the full azimuth and  $|\eta| < 0.9$ . The TPC has an active drift volume of 90 m<sup>3</sup>, which is filled with a mixture of 90% Ne and 10% CO<sub>2</sub>. It is divided in two halves by the central electrode ( $\eta = 0$ ), which is made out of 22  $\mu\text{m}$  thick mylar foil and is put to a high voltage of 100 kV. The design of the field cage and the chosen potential result in a homogeneous electric drift field of 400 V/cm with respect to the two outer walls. Charged particles, that cross the TPC, ionize the noble gas and the charges are separated by the electric field. The electrons then drift with constant speed up to 2.5 m to the outer walls, where they are read out. From the measured drift time the third dimension of the position of ionization is reconstructed.

The readout is segmented in inner and outer chambers in radial direction and 18 chambers in azimuthal direction per front-end, which gives 72 read-out chambers in total. Currently, the multiplied drift electrons are read out by the pads of multi-wire proportional chambers (MWPC). All readout chambers together contain 557568 pads, which allows to reconstruct up to 8000 charged particles per pseudo-rapidity unit. The TPC has 159 pads in radial direction and each track can thus ideally produce 159 ionization clusters.

For the future high luminosity run 3 at the LHC a collision rate of 50 kHz (cf. 3–4 kHz in run 1) is expected for heavy-ion collisions and an upgrade of the ALICE TPC readout to Gas Electron Multipliers (GEM) to replace the MWPCs is planned. This will allow a continuous readout without triggering and allow the TPC to cope with the increased collision rates. [ALICE13i]

### 3. The ALICE Experiment

The MWPCs are operated at 1500 V, which lies in the proportional region and hence the signal in the readout chambers is proportional to the primary electrons and the energy loss per path length  $dE/dx$  of the ionizing particle traversing the TPC gas. The  $dE/dx$  is characteristic for a given particle species and allows, together with the momentum reconstruction, to measure the mass or identify the type of particle.

Fig. 3.3 shows the  $dE/dx$  signal obtained from p-Pb collisions in 2013 as a function of momentum. Clear bands are visible for the most abundant particles, i.e. pions, kaons and protons, but also light nuclei (deuterons and tritons) can be identified. A clean separation is only possible up to a maximum momentum, where the different particle bands cross each other. Here, other PID methods are needed in addition.

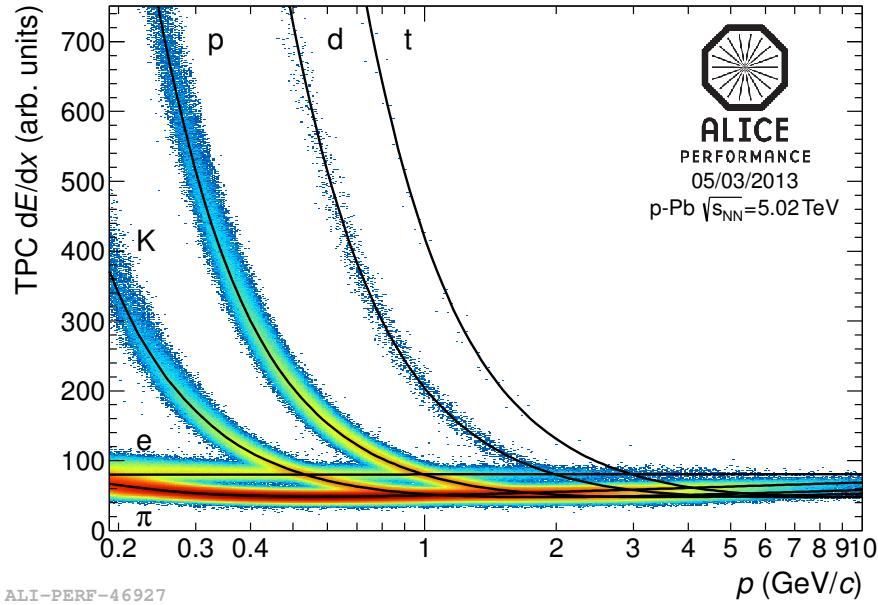


Fig. 3.3.: TPC PID performance in p-Pb collisions. Plotted is the energy loss  $dE/dx$  as a function of momentum. The different particle species are clearly separable up to a maximum  $p_T$  on a track-by-track basis and at high  $p_T$ , i.e. the relativistic rise region, with statistical means. The black lines are the fitted Bethe-Bloch parametrizations.

In the regions of clean separation the energy loss  $dE/dx$  of each particle band is fitted with the ALEPH parametrization [BRR08] of the Bethe-Bloch curve [Blo30]

$$f(\beta\gamma) = \frac{A}{\beta^D} \left( B - \beta^D - \ln\left(C + \frac{1}{(\beta\gamma)^E}\right) \right), \quad (3.1)$$

where  $\beta$  is the particle velocity,  $\gamma$  is the Lorentz factor, and  $A - E$  are free fit parameters. The resulting parametrizations for the p-Pb data taking period is depicted with the black lines in Fig. 3.3. The resolution of the  $dE/dx$  signal is about 5.5 - 6.2 %, depending on the particle multiplicity. In the low  $p_T$  region with good separation the width of the parametrization  $\sigma_{\text{TPC}}$  is used to identify particles on a track-by-track basis (cf. Section 5.1). At high  $p_T$ , i.e. in the relativistic rise region a separation is possible with statistical methods (cf. Section 5.2.3). For further details on the TPC, please refer to [AAA<sup>+</sup>10, ALICE14i].

### 3.3. Time Of Flight Detector

The Time Of Flight detector (TOF) [AAA<sup>+</sup>13] is shown in blue in Fig. 3.1 and is the most outward detector in the central barrel that covers the full azimuth. Like the TPC it covers a pseudo-rapidity region of  $|\eta| < 0.9$ . It consists of an array of Multigap Resistive Plate Chambers (MRPC) [ZCH<sup>+</sup>96, A<sup>+</sup>00], which are segmented in eighteen (in azimuth) times five modules (parallel to the beam line). Each module contains 15–19 MRPC strips, depending on the length of the module and each strip contains 96 readout pads. This gives a total of about 157000 readout channels.

The TOF requires a start signal, which corresponds to the time the collision takes place, to measure the time-of-flight of particles. By default, the start time is provided by the T0 detector, which consists of two arrays of Cherenkov detectors at  $-3.28 < \eta < -2.97$  and  $4.61 < \eta < 4.92$ . Each array holds 12 detectors equipped with a quartz radiator and photo multiplier tube. When requiring a hit in both arrays a time resolution of 25 ps (40 ps) is reached for Pb-Pb (pp) collisions. For the 60 % most central Pb-Pb collisions the T0 is fully efficient, but drops to about 50 % efficiency in pp collisions.

If at least three particles hit the TOF, the resolution can be increased by computing the arrival times with a combinatorial algorithm based on a  $\chi^2$  minimization between

all possible mass hypotheses. This method is also used if a T0 signal is not available and increases the start time efficiency especially for low multiplicity events.

The total time-of-flight resolution reached is  $\sigma_{TOF} \approx 80$  ps in the high multiplicity limit of p-Pb collisions ( $dN_{ch}/d\eta \gtrsim 30$ ). It is slightly worse for lower multiplicities: for example, if five tracks are available for the start time the resolution is  $\sigma_{TOF} \approx 95$  ps. [ALICE14i]

Together with the momentum, the time-of-flight measurement can be used to calculate the mass of a particle. Fig. 3.4 shows the performance of the TOF PID. Plotted is the relativistic  $\beta$  as a function of momentum. The particle bands for pions, kaons, protons and deuterons are clearly separated. However, particle identification with the TOF suffers from mismatched tracks, because a TOF hit can be associated to a wrong track, which means that a wrong time-of-flight is assigned to the track. To subtract this background several methods are available. In this thesis, the mismatch

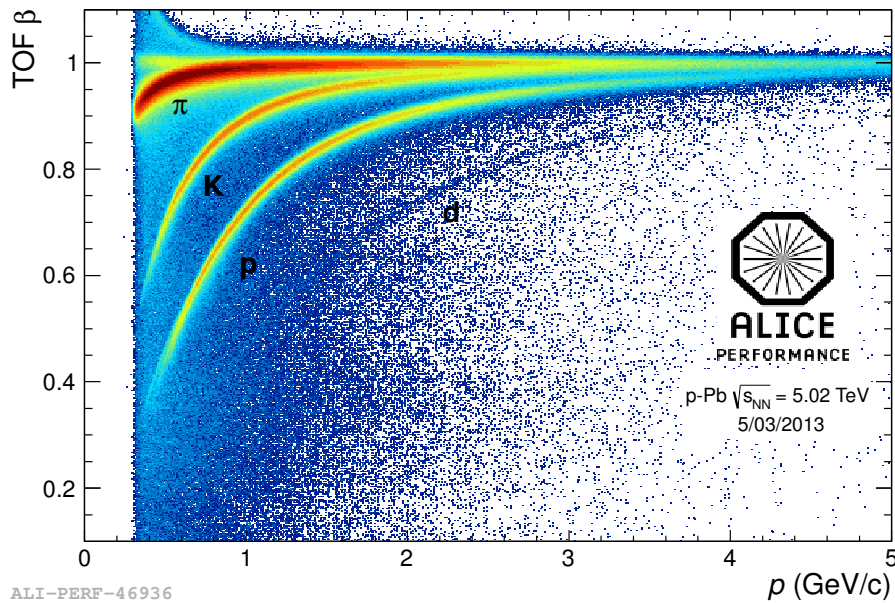


Fig. 3.4.: TOF PID performance in p-Pb collisions. The separation power of the TOF extends to high  $p_T$ . For example, it can be used on a track-by-track basis with  $3\sigma$  separation up to 2 GeV/c for protons. With statistical methods, this range can be extended up to 4 GeV/c. However, the background from mismatched tracks has to be taken into account. This is in particular important for rare particles like deuterons.

is suppressed by requiring an additional quality cut on the TPC PID signal (cf. Section 5.1). Another approach is to fit the TOF signal with the detector response and to include a template for mismatched tracks, when doing particle identification on a statistical basis (cf. Section 5.2.2). Mismatched tracks require special attention especially for rare particles like deuterons, because the signal to background ratio is more affected (cf. Section 6.3).

For more detailed information on the TOF detector please refer to [AAA<sup>+</sup>13, ALICE14i].

### 3.4. V0 Detector

The V0 detector consists of two scintillator arrays at forward ( $2.8 < \eta < 5.1$ ) and backward rapidity ( $-3.7 < \eta < -1.7$ ), which are called V0A and V0C, respectively. Each array is divided into four rings, which are split into eight segments each.

The V0 is used as a fast trigger input. For example, in the 2013 p-Pb run a coinciding hit in both V0A and V0C was required as a minimum bias trigger. It can also select on the event centrality or multiplicity, since the number of particles registered in the V0 and the number of emitted primary particles behave monotonously. It is thus also used as a fast online trigger to select high multiplicity events. In a similar way, the signal can be processed offline with more precision and is commonly used to define the centrality classes in Pb-Pb collisions and more importantly for this thesis, provides the multiplicity classes in p-Pb collisions (cf. Section 5.1.2). Furthermore, the V0 is used to discriminate background like beam-gas events by the arrival time.

### 3.5. Additional Detectors

Several subsystems of the ALICE detector are not directly used in this thesis and will only be introduced very briefly here. The *transition radiation detector* (TRD) is located in the central barrel between the TPC and the TOF. It improves the global tracking performance and can identify high- $p_T$  electrons and positrons with transition radiation. The two electromagnetic calorimeters PHOS and EMCal cover part of the central barrel acceptance and are mainly used to measure photons. The

HMPID is a *Ring Imaging Cherenkov Detector* (RICH) and is used for high momentum particle identification. It covers only part of the central barrel acceptance. The interested reader is referred to [ALICE08], which also contains references to the individual technical design reports.

## 3.6. ALICE Software

The software used in the ALICE experiment is bundled in the *AliRoot* framework [ALI14a], which is an extension to the commonly used *ROOT* software [Roo14]. It is written in C++, except for large existing external libraries and some legacy code. AliRoot is used for the offline processing of the data, which includes the simulation, reconstruction and analysis. A major feature of AliRoot is that it does not focus on particular packages, but provides interfaces for them, which allows the usage of several event generators, transport models and other modules within the AliRoot framework.

To handle the huge amount of data recorded by the ALICE detector of about 3-4 MB per p-Pb minimum bias event, the data is copied to the *large computing grid* [E<sup>+</sup>05], where it is processed utilizing massive parallelization. This is possible, because each event is independent and can be reconstructed and (in most cases) analyzed event by event. The user interface of the AliRoot software to the grid is the *Alice Environment* (AliEn) [Ali14b].

### 3.6.1. Event and Track Reconstruction

The reconstruction of the ALICE data is done event by event, where the global run calibration is taken into account. The reconstructed information is then stored in so called *Event Summary Data* objects (ESD), which contain global properties like the magnetic field configuration and event specific information, like the vertex position and the multiplicity. In addition, it contains the information on all reconstructed particle tracks of the event, like the track momentum and the energy loss in the TPC.

Only a short summary on the event and track reconstruction of the detailed description in [ALICE14i] will be given here. Fig. 3.5 shows schematically the reconstruction



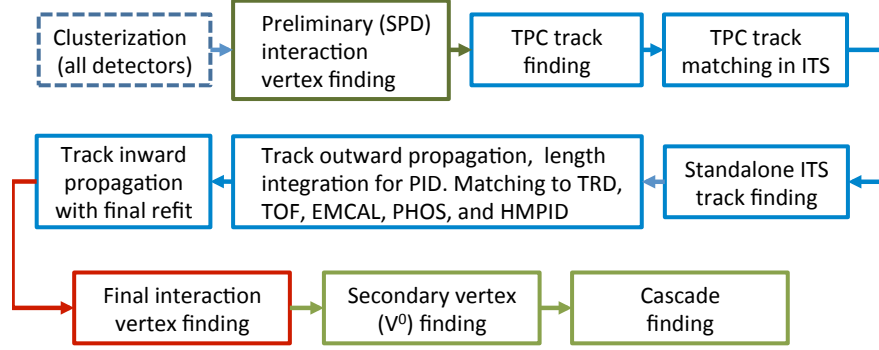


Fig. 3.5.: The reconstruction scheme of ALICE data in the central barrel. For details please refer to the text. Figure from [ALICE14i].

process of ALICE data in the central barrel. The first step is the clusterization of the detector raw data. Next, a preliminary vertex is obtained with the SPD information, which will be used for the track reconstruction, before the final vertex is reconstructed. After a preliminary vertex was found the track finding and fitting is performed in the TPC and ITS with a Kalman filter technique [Fru87].

The tracking is performed in three stages, following an *inward-outward-inward* scheme. The track finding starts at the outer edge of the TPC, where track seeds are built out of two clusters constrained to the vertex and then three clusters without vertex requirement. The seeds are propagated inward and are updated at each step with the nearest cluster, given that it is within a maximum distance. In addition, quality cuts are applied, which avoid extensive cluster sharing. Before propagating the TPC tracks to the ITS, a preliminary particle identification of pions, kaons and protons is performed, based on the energy loss in the TPC. This information is used in the following tracking steps to account for the energy loss of the particle in the detector. In case a PID can not be assigned, the pion mass is assumed (cf. Section 6.1.1).

The TPC track is propagated to the outer layer of the ITS, where it is used as a seed for the ITS tracking. This is performed in a similar fashion by updating the track

candidate information at each ITS layer. Please note that layers may be skipped, which is in particular important, when dead channels are present. Clusters, which are unused by the TPC-ITS tracking are now used to reconstruct low momentum particles that do not reach the TPC.

All tracks are now propagated to their point of closest approach to the vertex and are refitted by the Kalman filter in outward direction, while using the clusters found in the previous iteration. Once the edge of the TPC is reached the tracks are matched with the TRD, TOF and in a second step with EMCal, PHOS and HMPID. The final step, is the propagation from the outer edge of the TPC inward, where the tracks are refitted again with the previously found clusters. The resulting tracks are called *ITS-TPC tracks* or *global tracks*.

After removing outliers with respect to the beam line, the final vertex is reconstructed by a fit to the global tracks. The found tracks are mainly primary tracks and a dedicated algorithm, which searches for secondary particles and secondary vertices, is used.

#### 3.6.2. Simulation

Simulations of particle collisions are a three step process. In a first step an event generator produces the primary particles of the collision, which are then propagated through a simulation of the detector with a transport model in a second step. Within this process, secondary particles are produced and the simulated raw data of the detectors is generated. The last step is the reconstruction, which is performed in the same way as described above for data.

#### Monte Carlo Event Generators

Several event generators are available within the AliRoot framework for pp, p-A and A-A collisions [ALICE11c]. The two most relevant and common for p-Pb collisions in ALICE will be briefly introduced here.

HIJING (heavy-ion jet interaction generator) [Wan91] uses a Glauber model approach to model the initial conditions of p-A and A-A collisions and it combines perturbative QCD inspired models for multiple jet production with low  $p_T$  multi-string phenomenology. HIJING does not include any final state effects, except an

effective energy loss model for jet quenching. The phenomenological parameters are adjusted to reproduce essential measured features of pp collisions, like the jet production cross-section and the charged particle multiplicity. HIJING has been designed for RHIC and has since then been widely used for simulations in the RHIC and LHC era.

DPMJET [RER00] is based on the dual-parton model [CSTT94], which can be used for pp, p-A, A-A collisions, but also photon-hadron and photon-nucleus collisions. The nuclear cross-sections are modeled with a Glauber-Gribov approach to account for initial stage fluctuations, while PHOJET [ER96] is used for the elementary hadron-hadron (photon-photon and hadron-photon) interactions. For the soft particle production Reggeon field theory is used and perturbative QCD for hard interactions.

### Monte Carlo Transport Models

Transport models are used to model the geometry and the material of a detector and its support structure. Then the interaction of a particle that traverses the detector is simulated, where a number of physical processes can be considered. These usually include electromagnetic and hadronic processes. Particles that interact with a sensitive detector region create a hit. From these hits, digits are computed, which correspond to a detector output like a trigger signal of an ADC signal. These digits are then digitized by the AliRoot framework in several steps and finally processed as clusters by the reconstruction algorithm.

As already mentioned, AliRoot can utilize several transport models. The technical implementation is done with the *Virtual Monte Carlo* (VMC), which is an abstract layer between the detector description and the transport code. It has been developed in close cooperation with the ROOT collaboration and a detailed description is available in [ALICE03]. Originally, VMC modules were available for Geant 3 [BCG94], Geant 4 [GEANT03] and FLUKA [BMS<sup>+</sup>07a], but FLUKA VMC development has been discontinued by now.

Currently, Geant 3 is the default for ALICE Monte Carlo productions. However, Geant 4 has been tested extensively and is used for systematic cross checks. In addition, it follows a more sophisticated way to calculate the absorption cross-section

of light anti-nuclei at low momenta (1-10 GeV/ $c$ ), which is also used for this thesis (cf. Section 6.4.1).

#### 3.6.3. Analysis Tasks

The goal of an analysis task is to filter the relevant information from the reconstructed particle collisions data saved in the ESD objects. A task can be run on the grid over a given data sample. It is divided automatically in sub-tasks, which run only over a few events on any node within the grid. With this parallelization reasonable turn-around times of the order of hours to one day are possible. The output data of the sub-tasks is then collected, combined and usually post-processed on a local machine. Within this work two analysis tasks:

- PWGLF/SPECTRA/PiKaPr/TPCTOFpA/AliAnalysisTPCTOFpA.cxx
- PWGLF/SPECTRA/Nuclei/deuteronpA/AliAnalysisDeuteronpA.cxx

have been developed and included in AliRoot to measure the deuteron and pion, kaon and proton production. The tasks collect the relevant information in multi-dimensional histograms to perform the particle identification and corrections, which are described in Chapters 5 and 6.

## 4. Glauber Models

In heavy-ion collisions it is of fundamental interest to study observables as a function of centrality, i.e. how much the colliding nuclei overlap, since some observables are only visible or more pronounced in certain centrality ranges. A prominent example is elliptic flow, which is strongest for medium centralities, where an *almond-shaped* fireball is created. On the other hand, effects caused by the strongly interacting medium like high  $p_T$  suppression are more visible for the most central events, which correspond to a larger volume of the created medium.

Usually, the centrality is defined with the impact parameter  $b$ , which is the distance between the centers of the colliding nuclei. Unfortunately, this quantity can not be measured directly in the experiment, since the violent collision takes place on the femtometer scale. It is however possible to relate the measured charged-particle multiplicity with geometrical quantities like the impact parameter in heavy-ion collisions with Glauber models. They simplify the collision of the nuclei by assuming a superposition of  $N_{\text{coll}}$  independent nucleon-nucleon collisions and  $N_{\text{part}}$  participating nucleons.

Glauber models have been introduced to heavy-ion collisions by [BBC76, EKL89] and a more recent review of Glauber modeling can be found in [MRSS07]. In general, one has to distinguish between optical and Monte Carlo Glauber models. Optical models assume a constant nucleon density in the colliding nuclei and can be solved analytically. Monte Carlo models on the other hand simulate many events and distribute the nucleons randomly with a probability function within the nucleus for each event. This has the advantage that also the fluctuations of the geometrical quantities can be calculated. However, the mean values of both approaches are in very good agreement [MRSS07].

Both models make some common assumptions to simplify the complex process of a heavy-ion collisions. Nucleons are assumed to travel on straight lines parallel to the

beam axis and collisions are modeled by independent nucleon-nucleon collisions. By definition, this does not take any cold nuclear matter effects or interaction with the quark-gluon plasma into account. On the other hand, this allows to identify these effects by comparing measured pp collisions with measured heavy-ion collisions. Please note that shadowing can be included with the *Glauber-Gribov* approach, which is an extension to the original Glauber model [AKST10].

The nucleon density is usually parametrized with a Woods-Saxon distribution

$$\rho(r) = \rho_0 \cdot \frac{1 + w(r/R)^2}{1 + \exp(\frac{r-R}{a})}, \quad (4.1)$$

where  $R$  is the radius,  $a$  is the skin depth of the nucleus and  $w$  is an additional parameter to account for deviations of the radial symmetry of the nucleus.  $\rho_0$  is a normalization parameter or more qualitatively: the density at the center of the nucleus. The integral over the density distribution has to be equal to the number of nucleons  $N_A$  of the nucleus under consideration for the optical model. For Monte Carlo Glauber models it is irrelevant, because the density function is only used to randomly distribute the fixed number of nucleons within the nucleus for each event.

### 4.1. Optical Glauber Model

Fig. 4.1 shows the geometry of two nuclei A and B, which collide with impact parameter  $b$  at relativistic speeds. The nuclear thickness function  $T_A$  is defined as

$$T_A(s) = \int_{-\infty}^{\infty} \rho_A(r = \sqrt{s^2 + z^2}) dz, \quad (4.2)$$

when considering a slice in the nucleus A in z-direction at position  $\vec{s}$ . The thickness function  $T_B$  is defined analogous. This allows to calculate the so called nuclear overlap function by multiplying the two functions and integrating over  $d^2s$

$$T_{AB}(b) = \int T_A(\vec{s}) T_B(\vec{s} - \vec{b}) d^2s. \quad (4.3)$$

This gives then the total number of nucleon-nucleon collisions

$$N_{\text{coll}} = T_{AB}(b) \cdot \sigma_{NN}, \quad (4.4)$$

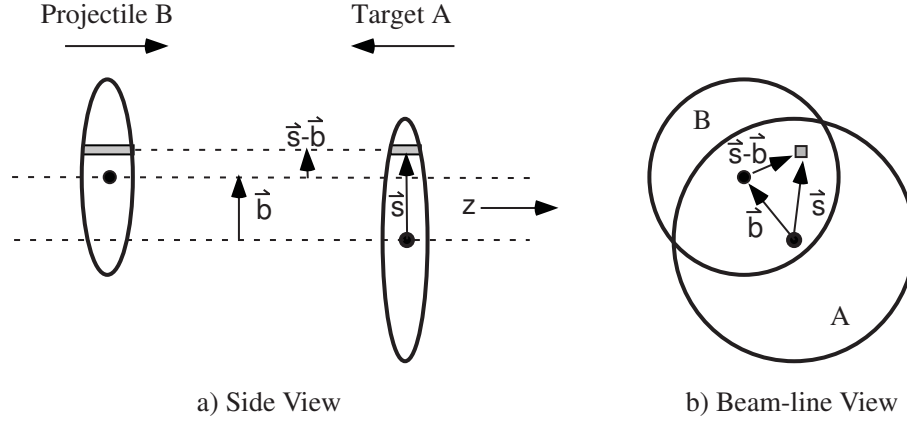


Fig. 4.1.: Geometry for Glauber calculations in the side view (a) and the beam-line view (b). The impact parameter  $b$  is defined as the distance between the centers of the two colliding nuclei. Figure from [MRSS07].

where  $\sigma_{NN}$  is the inelastic nucleon-nucleon cross-section. The number of wounded or participating nucleons is defined as the number of nucleons, which have undergone at least one inelastic collision and can be calculated with

$$N_{\text{part}}(b) = \int T_A(\vec{s}) \left[ 1 - \left( 1 - \frac{T_B(\vec{s} - \vec{b})}{N_B} \sigma_{NN} \right)^{N_B} \right] d^2s + \int T_B(\vec{s} - \vec{b}) \left[ 1 - \left( 1 - \frac{T_A(\vec{s}) \sigma_{NN}}{N_A} \right)^{N_A} \right] d^2s, \quad (4.5)$$

where  $(1 - \frac{T_I \sigma_{NN}}{N_I})^{N_I}$  is the probability of a nucleon with a given impact parameter to pass through the nucleus without interacting hadronically. Please note that each nucleon is allowed to interact multiple times.

## 4.2. Monte Carlo Glauber Model

In contrast to the optical model, the Monte Carlo Glauber model distributes the nucleons within the nucleus for each event according to the density function defined in Formula 4.1.

For each event a random impact parameter is drawn from the following distribution

$$d\sigma/db = 2\pi b. \quad (4.6)$$

To avoid many events without interaction, a maximum impact parameter  $b_{\max}$  can be defined. Then for each randomly distributed nucleon it is checked if it interacts with a nucleon from the other nucleus with the requirement that the transverse distance  $d$  between the two nucleons is smaller than the radial nucleon-nucleon cross-section

$$d \leq \sqrt{\sigma_{NN}/\pi}. \quad (4.7)$$

Please note that the nucleon-nucleon cross-section  $\sigma_{NN}$  is assumed to be independent of how many interactions a nucleon has previously undergone. This implies that each nucleon can collide with more than one nucleon. Calculating the number of binary collisions and number of participants for each event remains a simple matter of counting. By simulating many collisions, mean values and their fluctuations can be calculated. The nuclear overlap function is in principle a concept from the optical Glauber model, but it is useful to calculate the nuclear modification factor, since the uncertainty of the nucleon-nucleon cross-section partially cancel in it. It can be calculated with  $T_{AB}(b) = N_{coll}/\sigma_{NN}$ .

To connect the Glauber calculations to an experimentally measured multiplicity distribution several approaches exist. For Pb-Pb collisions in ALICE [ALICE13c], the number of ancestors  $N_{anc} = f \cdot N_{part} + (1 - f) \cdot N_{coll}$  is calculated. Here,  $f$  is a free parameter, which adjusts the ratio of soft and hard particle production. Each ancestor is an independently emitting source of particles, which is parametrized as a negative binomial distribution (NBD). The parameters of the NBD and  $f$  are obtained with an iterative fit to the experimental multiplicity distribution with a  $\chi^2$ -minimization procedure. This connects each Monte Carlo Glauber event with a multiplicity and the mean geometrical quantities and fluctuations can be calculated for a given multiplicity interval or vice versa.



### 4.3. Glauber Simulation for p-Pb Collisions with ALICE

For p-Pb collisions, Glauber calculations can be set up in the same way, as described above, but some difficulties arise for the last step, which connects the geometrical quantities to an experimentally accessible quantity, i.e. a measured multiplicity. The main difficulties are biases that are also present but negligible in heavy-ion collisions. In particular, the multiplicity fluctuations at a fixed  $N_{\text{part}}$  are sizable with respect to the width of the  $N_{\text{part}}$ -distribution in p-Pb, while for Pb-Pb collisions the dynamic range of  $N_{\text{part}}$  is much larger. In addition, the selection of low multiplicity events introduces a veto on events that contain a jet. A centrality estimator independent bias arises by the lower mean number of multiple parton interactions for peripheral events, which is caused by a larger mean impact parameter for nucleon-nucleon collisions. For a detailed discussion and new approaches to define centrality in p-Pb collisions with ALICE please refer to [ALICE14c].

However, it is possible to perform the calculations for the minimum bias event sample, which allows to compare p-Pb collisions to pp and Pb-Pb collisions, with the mean number of participants and number of binary collisions.

Within this thesis the existing code in AliRoot, which is bundled in the *PWGGlauber* class was set up and used. The parameter values with their systematic uncertainties are summarized in Table 4.1

Parameter	Value	Description
$R_{\text{Pb}}$	$6.62 \pm 0.06$ fm	Radius of Pb nucleus
$a_{\text{Pb}}$	$0.546 \pm 0.010$ fm	Skin depth of Pb nucleus
$w_{\text{Pb}}$	0	Sphericity of Pb nucleus
$d_{\text{Pb}}$	$0.4 \pm 0.4$ fm	Hard sphere exclusion distance
$R_{\text{p}}$	$0.6 \pm 0.2$ fm	Radius of proton
$\sigma_{NN}$	$70 \pm 5$ mb	Nucleon-nucleon cross-section

Table 4.1.: Parameters for p-Pb Glauber calculations. Skin depth and sphericity of the proton is not applicable since it consists of one nucleon only. The cross-section has been extrapolated from measured ALICE data. Please refer to the text for more details.

The nucleon-nucleon cross-section has been taken from [ALICE13f]. The calculations have been repeated for the lower and upper limits of the systematic uncertainties for each parameter to evaluate the systematic uncertainty of the mean number of binary collisions and mean number of participants. The individual systematic uncertainties have been summed quadratically. This gives  $\langle N_{\text{part}} \rangle = 7.8835 \pm 0.5643$ ,  $\langle N_{\text{coll}} \rangle = 6.8835 \pm 0.5643$  and  $\langle T_{\text{pPb}} \rangle = 0.09834 \pm 0.00338 \text{ mb}^{-1}$  for minimum bias collisions. Statistical uncertainties are negligible since one million events have been generated for each setup.

These calculations have already been used in ALICE publications for the charged particle pseudo-rapidity density [ALICE13h] and for the nuclear modification factor of all charged particles [ALICE12b]. Within this thesis, they will be used for the nuclear modification factor of identified particles (cf. Section 5.3.4).

## 5. Production of Pions, Kaons and Protons in p–Pb Collisions

In this chapter the production of the most abundant particles ( $\pi$ , K, and p) in p–Pb collisions at  $\sqrt{s_{\text{NN}}} = 5.02$  TeV as a function of multiplicity will be discussed. Within this thesis the transverse momentum distributions of pions, kaons and protons at intermediate  $p_{\text{T}}$  have been measured with the TPC-TOF method, which will be discussed in detail in Section 5.1. The measurement was extended to lower and higher  $p_{\text{T}}$  with different PID approaches, which will be introduced briefly in Section 5.2. The low and high  $p_{\text{T}}$  part of the spectra have not been measured within this thesis, but resulted together with this work in a common publication that covers a wide  $p_{\text{T}}$  range and also includes strange particles ( $K_{\text{S}}^0$ ,  $\Lambda$  and  $\bar{\Lambda}$ ). The comprehensive results of  $\pi^{\pm}$ ,  $K^{\pm}$ ,  $K_{\text{S}}^0$ ,  $p(\bar{p})$  and  $\Lambda(\bar{\Lambda})$  have been reported in [ALICE14h] and this chapter is widely based on this publication. Results of  $\pi$ , K, and p production in p–Pb collisions at the LHC have also been reported by the CMS collaboration [CMS14b].

### 5.1. Particle Identification at Intermediate Transverse Momenta

To identify  $\pi$ , K, and p at intermediate  $p_{\text{T}}$  the energy loss of the particles in the gas of the TPC and the time-of-flight measured with the TOF detector is used (cf. Section 3). The TPC-TOF method has been introduced for the measurement of pions, kaons and protons in Pb–Pb collisions in [Kal12, ALICE12a]. With this method a wide  $p_{\text{T}}$  range (specified below) can be covered with a track-by-track identification.

Fig. 3.3 shows the measured energy loss  $dE/dx$  as a function of particle momentum in minimum bias p–Pb collisions recorded in 2013. The black lines superimposed

to the data represent the Bethe-Bloch parametrization. Clean separation of pions (kaons, protons) for momenta lower than 0.6 GeV/ $c$  (0.35 GeV/ $c$ , 1 GeV/ $c$ ) is possible by applying a cut of  $3\sigma_{TPC}$  around the expected energy loss. Here  $\sigma_{TPC}$  is the resolution of the  $dE/dx$  signal in the TPC and it is of the order of 5%. The  $p_T$  range of kaons, accessible with the TPC  $3\sigma$ -cut, can be extended to 0.55 GeV/ $c$  by subtracting the contamination from electrons, which will be discussed in Section 5.1.5. To be able to go to higher momenta the time-of-flight information of the TOF is used in addition to the cut on the TPC signal, which provides a good pre-selection reducing mismatched tracks to a negligible amount ( $< 1\%$ ). The performance of the TOF PID has already been presented in Fig. 3.4, which shows the relativistic  $\beta$  as a function of particle momentum. By requiring an additional cut of  $3\sigma_{TOF}$  around the expected time-of-flight a clean separation is possible up to 1.5 GeV/ $c$ , 1.3 GeV/ $c$  and 2.0 GeV/ $c$  for pions, kaons and protons, respectively. Here,  $\sigma_{TOF}$  corresponds to the time resolution of the TOF detector, which is as small as 80 ps in high multiplicity  $p$ -Pb collisions (cf. Section 3.3).

An advantage of the TPC-TOF method is the track-by-track identification, which also allows further measurements like two-particle-correlations of identified particles [ALICE13d]. In addition, it is very robust with respect to non-perfect parametrizations of the energy loss in the TPC. In case the resolution is underestimated by 20% or the parametrization is shifted by  $0.5\sigma_{TPC}$  the systematic error amounts to approximately 1%.

With the TPC-TOF method it is possible to measure pions (kaons and protons) at momenta as low as 200 MeV/ $c$  (300 MeV/ $c$  and 500 MeV/ $c$ ). Below these momenta a measurement with global tracks is not feasible, because the global tracking becomes very inefficient. The spectra can be extended to lower  $p_T$  by using the ITS tracking and PID exclusively. At high  $p_T$  the TPC-TOF method is limited by the track-by-track separation power of the TOF. Other methods that use a statistical identification approach with unfolding, are more advantageous in this region (cf. Section 5.2).

### 5.1.1. Event Selection

Transverse momentum distributions have been obtained from the  $p$ -Pb run at  $\sqrt{s_{NN}} = 5.02$  TeV, which took place in 2013. For this analysis a minimum bias data

sample (ALICE internal identifier: *run 195483*) was used, which contains about 15 million events after all the following event selection cuts.

During the data taking, a minimum bias trigger (ALICE internal identifier: *INT7*) was used that requires a coinciding hit in both V0 detectors, which are placed at forward rapidity on the A- and C-side (cf. Section 3). This removes contamination from single-diffractive and electromagnetic events. The time resolution is better than 1 ns, allowing a discrimination of beam-beam collisions from background events, e.g. produced by beam-gas collisions. The trigger selection and timing cut is repeated in the offline analysis. Furthermore the time information from the ZDCs is used to further suppress the background.

In addition to this selection, only events that have a reconstructed vertex are considered for the analysis. The vertex reconstruction efficiency for non-single-diffractive (NSD) events was estimated to 98.5% and the total reconstruction efficiency of NSD events was estimated to 96.4%. Taking the differences of the selection in Monte Carlo and data with respect to events without a vertex into account the total efficiency is 97.9% for minimum bias collisions [ALICE13h]. The transverse momentum distributions in this work are not corrected for the reconstruction efficiency. They are reported as fractions of the visible V0A cross-section. However, the correction is applied to calculate the  $R_{pPb}$  (cf. Section 5.3.4).

### 5.1.2. Multiplicity Selection

The measurement of the transverse momentum distributions of  $\pi$ , K, and p is presented in several multiplicity classes. For p-Pb collisions a definition of centrality is very challenging, because the dynamic range in charged-multiplicity is much smaller compared to heavy-ion collisions and the correlation between multiplicity in a given pseudorapidity range and the impact parameter is weak. The transverse momentum spectra are therefore presented as a function of V0A multiplicity classes, which are defined as slices in the detector amplitude and are not directly connected to the collision geometry. Please note that V0A is positioned at the Pb-going side in p-Pb collisions and therefore measures the remnants of the nucleus and not of the incoming proton. In this thesis only minimum bias data with this beam setup is considered. In case of Pb-p collisions, the different acceptance window of V0C with respect to V0A has to be taken into account.

Event class	V0A range (arb. units)	$\langle dN_{\text{ch}}/d\eta \rangle_{ \eta_{\text{lab}}  < 0.5}$
0–5%	$> 227$	$45 \pm 1$
5–10%	187–227	$36.2 \pm 0.8$
10–20%	142–187	$30.5 \pm 0.7$
20–40%	89–142	$23.2 \pm 0.5$
40–60%	52–89	$16.1 \pm 0.4$
60–80%	22–52	$9.8 \pm 0.2$
80–100%	$< 22$	$4.4 \pm 0.1$

Table 5.1.: Definition of the event classes as fractions of the analyzed event sample and their corresponding  $\langle dN_{\text{ch}}/d\eta \rangle$  within  $|\eta_{\text{lab}}| < 0.5$ . Only systematic uncertainties are shown, since statistical uncertainties are negligible.

The classes are selected using the standard AliRoot framework, which ensures that the cut boundaries are set as well defined percentiles of the raw multiplicity estimators. The event classes are summarized in Table 5.1 with the V0A multiplicity cuts and the corresponding mean charged particle multiplicity at mid-rapidity in these classes.

### 5.1.3. Track Selection

The track candidates used for the analysis have to pass certain quality cuts that are summarized in Table 5.2 and they correspond mostly to the standard cuts for global tracks in ALICE. For the TPC at least 70 crossed pad rows and a ratio of crossed rows over findable clusters larger than 0.8 is required. The Kalman fit is required to have a smaller  $\chi^2/N_{\text{cluster}} < 4$  ( $< 36$ ) for the TPC (ITS) and a refit of the TPC and ITS is requested (cf. Section 3.6.1). In addition, at least one cluster in the SPD is required. The cut on  $\text{DCA}_{\text{xy}}$  is released with respect to the standard cuts, because the  $\text{DCA}_{\text{xy}}$  distribution is used to subtract the contribution of secondary particles manually from the raw yield. Furthermore, a cut on  $\eta$  was introduced to account for the acceptance of the central barrel.

With these track cuts a good track quality can be obtained, but the tracking is not fully efficient. To correct for the inefficiency a correction based on Monte Carlo

Cut	Value
Number of Crossed Rows in the TPC	$> 70$
Crossed Rows/Findable Ratio	$> 0.80$
TPC Refit Flag	yes
$\chi^2$ / TPC cluster	$< 4$
ITS Refit	yes
ITS Cluster requirement	One cluster in SPD
$\chi^2$ / ITS cluster	$< 36$
DCA <sub>z</sub> to vertex	2 cm
DCA <sub>xy</sub> to vertex	3 cm
Track $ \eta $	$< 0.8$

 Table 5.2.: Track selection cuts for  $\pi$ , K, and p track candidates.

simulations is applied as in Section 5.1.5. The track cuts are varied within reasonable limits to calculate the systematic uncertainty of this selection (cf. Section 5.1.7).

#### 5.1.4. Choice of Rapidity Range

The two-in-one magnet design of the LHC results in an asymmetric beam energy per nucleon for the two beams in p-Pb collisions at  $\sqrt{s_{\text{NN}}} = 5.02$  TeV. Hence, the *center-of-mass system* (c.m.s) moves with  $\Delta y = 0.465$ .<sup>1</sup> Identified particle production in the symmetric collision systems pp and Pb–Pb has been measured around mid-rapidity in ALICE [ALICE11b, ALICE13b, ALICE12a]. There the c.m.s. coincides with the laboratory frame, which means that  $y = 0$  coincides with the center of the central barrel detectors, which cover  $|\eta_{\text{LAB}}| < 0.9$ .

For p-Pb  $y = 0$  is at  $\eta_{\text{LAB}} = 0.465$  for a mass-less particle. Measuring a whole rapidity unit around  $y = 0$ , which corresponds to  $-0.035 < \eta_{\text{LAB}} < 0.965$  results in an acceptance correction based on Monte Carlo simulations. This is even more crucial for particles that carry mass since then  $\eta \neq y$ . To avoid this correction, which would introduce an additional systematic uncertainty, an asymmetric rapidity range of  $-0.5 < y < 0$  was chosen.

In addition, this range has the advantage of a cleaner TPC PID sample at higher  $p_{\text{T}}$ , because the TPC PID energy loss is measured as a function of the total particle momentum. Considering particles that are at the edge of the detector, the contri-

<sup>1</sup>Please note the sign convention: positive rapidity is in the direction of the proton.

bution of the momentum in  $z$ -direction results in a higher total momentum at the same  $p_T$ , when comparing to particles at the center of the detector. This means that the crossings of particle bands for the energy loss in the TPC (compare Fig. 3.3) are at lower  $p_T$  for particles, which are further towards the edge of the detector. By using the center of the detector pure TPC PID can be used to higher transverse momenta, without the need of a contamination correction. This effect is shown in Fig. 5.1 for pions and protons.

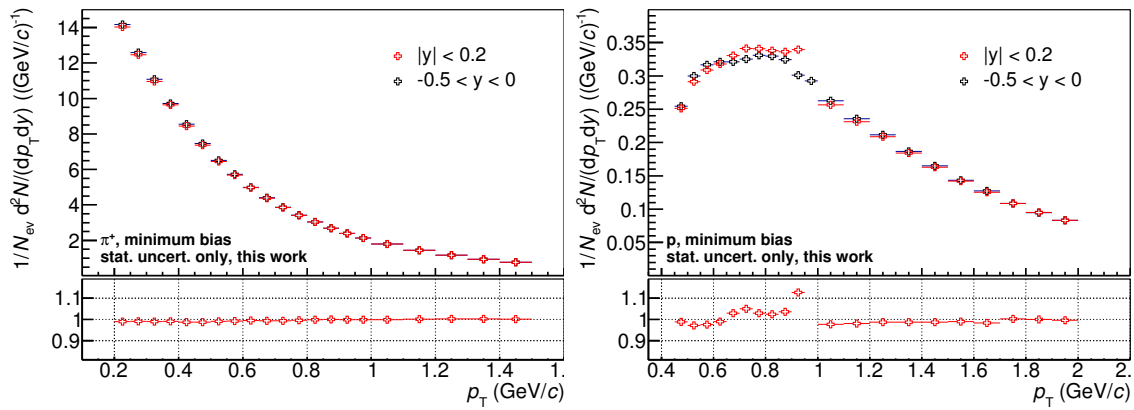


Fig. 5.1.: Effect of different rapidity ranges for pions (left) and protons (right). The difference between the two rapidity ranges is within a few percent. When selecting around mid-rapidity the contamination for pure TPC PID is clearly visible for protons below 1 GeV/c. This effect is not visible for the lighter pions.

Nevertheless, the analysis has been repeated in  $|y_{CMS}| < 0.2$  as a systematic cross check, which results in differences smaller than 2% in the normalization and 3% in the shape of the transverse momentum distributions.

### 5.1.5. Corrections

Once the raw spectra are obtained with the TPC-TOF particle identification method and the cuts described above, they have to be corrected for several effects to get the final transverse momentum distributions of primary identified particles.



### Tracking and TOF Matching Efficiency

Naturally, the tracking algorithm of the offline reconstruction in ALICE is not fully efficient (cf. Section 3.6.1) and a correction for the inefficiency of the global tracking has to be introduced. To calculate the efficiency a Monte Carlo simulation (ALICE internal identifier: *LHC13b2.efix*) is used, which was generated with DPMJET and a full ALICE detector simulation with GEANT 3. The efficiency is defined as

$$\epsilon_{tracking}(p_T) = \frac{n_{rec}(p_T)}{n_{gen}(p_T)}. \quad (5.1)$$

where  $n_{rec}$  is the number of correctly reconstructed particles and  $n_{gen}$  the number of generated particles in a given  $p_T$ -bin and within the track quality and kinematic cuts introduced above.

The resulting tracking efficiency of particles (left) and anti-particles (right) is shown in Fig. 5.2 for two multiplicity classes each. At low  $p_T$  the tracking is inefficient, because of energy loss and multiple scatterings with the detector material. At high  $p_T$  the efficiency slightly decreases, because for high  $p_T$  particles the curvature induced

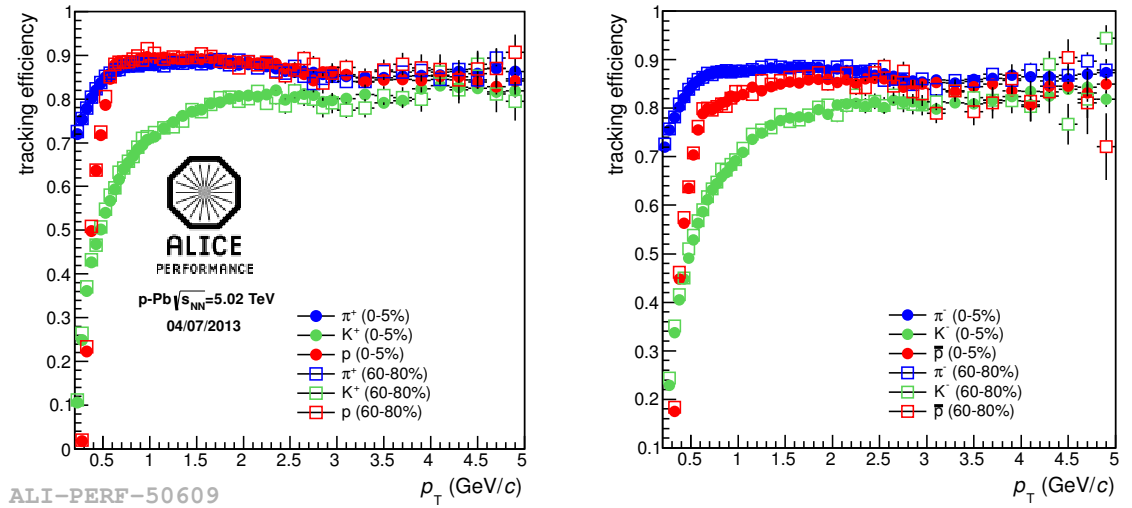


Fig. 5.2.: Global tracking efficiency of particles (left) and anti-particles (right) for  $\pi$ , K, and p for a low and high multiplicity class. No (small) multiplicity dependence is observed for pions and protons (kaons). The lower efficiency of  $\bar{p}$  with respect to the efficiency of p is due to absorption.

by the magnetic field is smaller with respect to lower momentum particles. For straighter tracks the dead zones between two readout chambers is more relevant, because the clusters of two neighbouring chambers are further apart and can not be connected as easily.

In general, a multiplicity dependence of the global tracking efficiency is not observed and the minimum bias efficiency is used for all multiplicity classes. For kaons a small deviation is seen at very low  $p_T$ , which is taken into account for the systematic uncertainties of the tracking.

In case the time-of-flight measurement of the TOF detector is used for particle identification, the global track has to be matched with a hit in the TOF. To account for the inefficiency of this matching a TOF matching efficiency is extracted from Monte Carlo simulations. There is no multiplicity dependence observed and the minimum bias efficiency is used for all multiplicity classes, which is shown for pions, kaons and protons in Fig. 5.3. The absorption of anti-particles, which manifests in a lower efficiency, is more pronounced than for global tracking efficiency since the material of the TRD is crossed by the particles to reach the TOF.

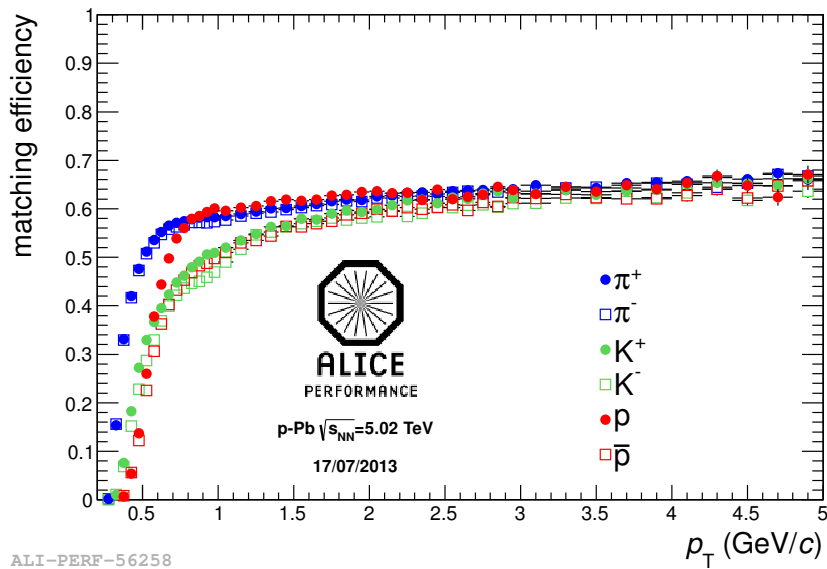


Fig. 5.3.: TOF matching efficiency of  $\pi^\pm$ ,  $K^\pm$  and  $p(\bar{p})$  for minimum bias events.

### Absorption Correction

The default transport code for ALICE simulations GEANT 3 is known to not reproduce the absorption of anti-matter due to hadronic interactions [ALICE13b]. Therefore the  $K^-$  and  $\bar{p}$  raw yields have to be corrected with a dedicated FLUKA simulation, which describes the available measurements much better at low momenta [ALICE10].

For the simulations used to extract the efficiencies in this work GEANT 3.21 [MO97] was used, which incorporates a more realistic parametrization of the  $\bar{p}$  inelastic cross-section. However, for  $K^-$  a correction as in [ALICE13b, ALICE12a] needs to be applied. The correction is about 3% at low momenta and less than 5% when TOF matching is required. It is higher when using the TOF, because the additional material of the TRD has to be crossed.

### Secondary Correction

The inclusive yields of pions and protons include primary particles from the initial collision, but also secondary particles from decays and material interactions, which need to be subtracted from the raw yield. In ALICE, primary particles are defined as particles produced in the collision, including all decay products, except products from weak decays of light flavor hadrons and of muons. The secondary correction is not necessary for kaons, because they are not produced by the interaction of particles with the detector material and only particles with very low abundances like the  $\Omega^-$  or the  $D^0$  feed into the kaon yield. For example, the  $\Omega^-$  is about a factor 200–400 less abundant than the  $K^-$  for high to low multiplicity p-Pb collisions [ALICE14l]. In addition, only two thirds of the  $\Omega^-$  feed into the  $K^-$ -yield, because the branching ratio is about 67.8% [PDG12].

A common way to subtract the contribution from secondary particles is to calculate the secondary and primary fraction from Monte Carlo simulations. For this analysis a data-driven approach as in [ALICE13b, ALICE12a] was chosen, because:

- The strange particle production is vastly underestimated in common generators like HIJING and DPMJET, but for example  $\Lambda$ s feed into the proton and pion yield.

- The cross-section for the production of secondary particles from interaction with the detector material is underestimated in GEANT 3, as explained before.

For each contribution to the inclusive yield a  $DCA_{xy}$ -template is extracted from the Monte Carlo simulation: primary particles, secondary particles from weak decays and secondary particles from the interaction with the detector material. Each template has a very distinguishable shape, which allows a clear separation. The  $DCA_{xy}$ -distribution from data is then fitted with the Monte Carlo templates by the ROOT class *TFractionFitter*. This fit method takes the statistical errors of each template and the data distribution into account and allows the fit results of each  $p_T$ -bin to vary in those limits. An example for the fit is shown in Fig. 5.4 for protons with  $450 \text{ MeV}/c < p_T < 500 \text{ MeV}/c$ . The contribution from the detector material is negligible for pions and anti-protons and thus only a primary template and a template for secondaries from weak decays are considered.

To minimize the size of the correction and the systematic uncertainty, that is introduced with the correction, the fit is performed in  $\pm 3 \text{ cm}$ , but the fraction of

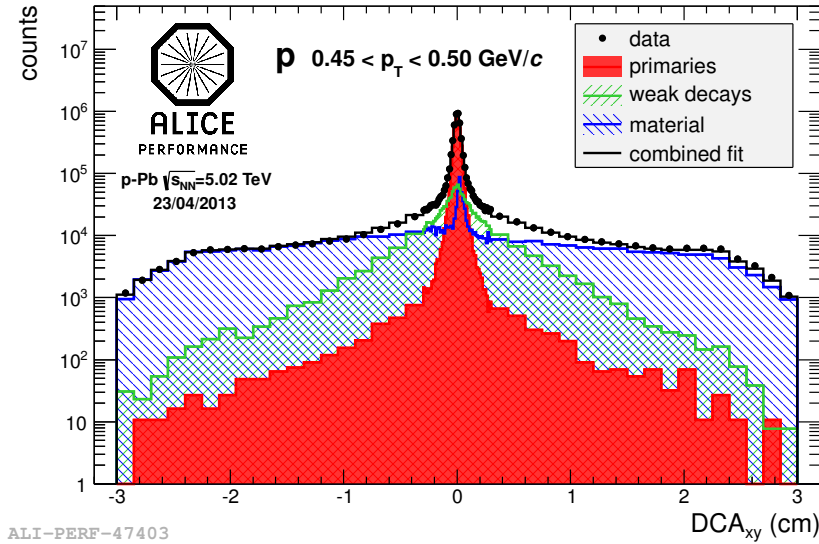


Fig. 5.4.: Secondary fit of protons with  $450 \text{ MeV}/c < p_T < 500 \text{ MeV}/c$ . The three templates show a very distinguishable shape and the fit quality is good for all  $p_T$ -bins and particles.

primaries is calculated in a smaller  $\text{DCA}_{xy}$ -range, which is given by the following  $p_T$ -dependent functional form:

$$0.0105 + \frac{0.0350}{p_T^{1.1}} \quad (5.2)$$

This includes nearly all primaries ( $> 95\%$  at low  $p_T$ , negligible loss at intermediate  $p_T$ ) and removes most secondaries. The small fraction of primaries that is cutted is corrected based on Monte Carlo information. By applying this cut the correction at low  $p_T$  is reduced from 14% to 5% for pions and from 55% to 18% for protons. It drops quickly for higher  $p_T$ .

The secondary correction is independent of the multiplicity class. Therefore the minimum bias correction is used for all multiplicities.

### Correction for electron contamination in kaon signal

As mentioned before the hadronic cross-section of  $K^-$  is described poorly in GEANT 3. Hence, for the measurement of  $K^-$  it is advantageous to use a PID method, where as little material as possible is crossed by the particle. This is in particular important for low  $p_T$  particles.

Within the TPC-TOF method it is therefore beneficial to use the pure TPC PID, i.e. TOF matching is not required, to momenta as high as possible. In Fig. 3.3 the limitation of a clean kaon signal without contamination can be identified as the pion and electron bands. Here, the electron band crosses the kaon band at lower momenta and gives the usual limitation of about 350 MeV/c. With an approach similar to the secondary subtraction it is possible to remove the electron contamination and use the TPC PID up to transverse momenta of 550 MeV/c, where the pion and kaon band cross. The majority of the electrons stem from conversions and have a characteristic  $\text{DCA}_{xy}$  distribution, which allows a separation of the electrons from the kaons. The templates are extracted from Monte Carlo and are fitted to the data as in the previous section. An example is shown in Fig. 5.5. The procedure is identical for  $K^+$  and  $e^+$ .

The reason for the asymmetry of the electron  $\text{DCA}_{xy}$ -distribution lies in the special decay kinematics of conversion electrons, which dominate the electron yield. The momentum of an electron from a conversion points in radial direction, i.e. the direc-

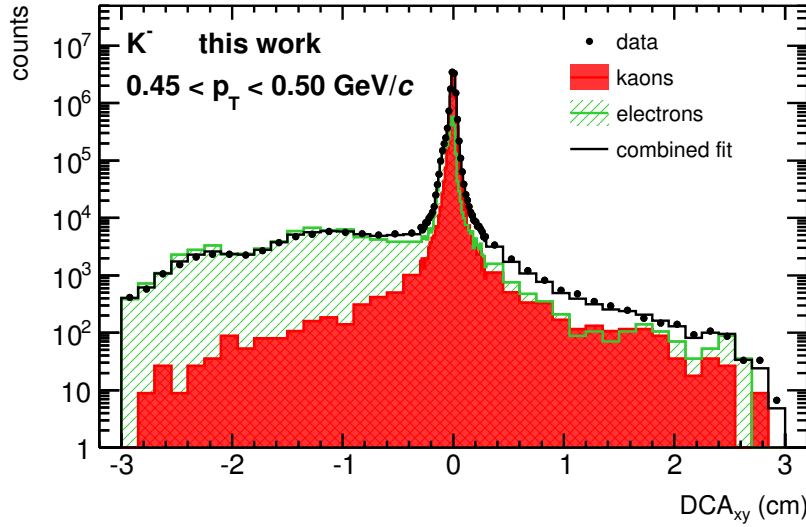


Fig. 5.5.: Fit to  $DCA_{xy}$ -distribution to remove electron contamination from the kaon signal for  $450 \text{ MeV}/c < p_T < 500 \text{ MeV}/c$ . The electron yield is dominated by conversion electrons. Please note the asymmetry of the electron template, which stems from the decay kinematics of conversions. For positrons the sign of the asymmetry is switched. Please refer to the text for more details.

tion of the photon and the electron and positron are separated by the magnetic field in the ALICE central barrel. By propagating the bended tracks back to the vertex a systematic shift to positive  $DCA_{xy}$  for positrons and to negative  $DCA_{xy}$  for electrons is evident. Please note that this behavior obviously depends on the magnetic field sign and must be used with caution, when mixing the magnetic field configurations. The correction ranges from 0% to 20% for  $p_T$  from 250  $\text{MeV}/c$  to 500  $\text{MeV}/c$ .

### 5.1.6. Monte Carlo Closure Test

To check the working principle of an analysis method a Monte Carlo closure test is useful. When using the full analysis chain on simulated data, the spectra should ideally be in agreement with the spectra from the particle generator, which is used as input for the simulation. This check was performed and the spectra from the generator level are reproduced reasonably well as can be seen in Fig 5.6.

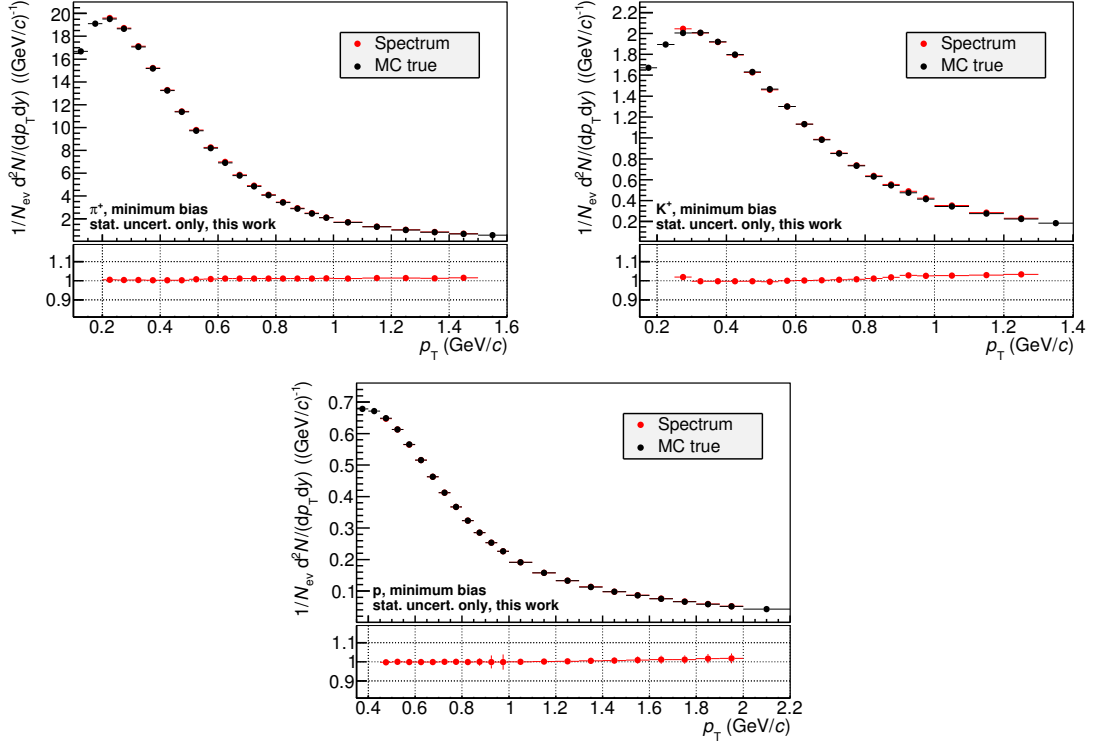


Fig. 5.6.: Monte Carlo closure test for minimum bias pions (top left), kaons (top right) and protons (bottom). The spectra obtained by using the full analysis chain are in good agreement with the generated particle spectra, labeled as MC true. The bottom panels show the ratio of the respective spectrum over the corresponding MC true spectrum.

However, the energy loss and the parametrization in the TPC is different for simulations and data. In particular, the particle band crossings are at lower transverse momenta in Monte Carlo simulations with respect to data. To correct for this contamination, which is not present in data, a template with misidentified particles was added to the feed-down fit and subtracted from the spectra. This affects only the  $p_T$  regions, where the TPC PID is used exclusively and there only for higher  $p_T$ . The closure test is only shown for  $\pi^+$ ,  $K^+$  and p for minimum bias collisions here, but it is consistent with unity for all multiplicities and all particles.

### 5.1.7. Systematic Uncertainties

There are several systematic uncertainties that have to be considered for the measurement of the identified particle transverse momentum distributions. Some can be taken from similar analysis, whereas others like the uncertainty on the tracking efficiency are calibration dependent and have been re-evaluated for this analysis. In the following all relevant systematic uncertainties are discussed.

#### Tracking

The systematic uncertainty was obtained by varying the default track cuts in the following ways:

- The minimum number of crossed rows: 50/70(default)/100
- The ratio of findable clusters over crossed rows: 0.6/0.8(default)/0.95

To the uncertainty from those variations a 3% constant error is added quadratically for the matching of TPC and ITS tracks, which was computed in [ALICE12b]. Analogous to the ITS-TPC matching a systematic uncertainty of 4% for the TPC-TOF matching is added to the tracking uncertainty. This uncertainty was computed with the TOF fits particle identification method, which will be introduced in Section 5.2. The tracking efficiency is independent of multiplicity for pions and protons, but for kaons a small multiplicity dependence of the efficiency at very low  $p_T$  is observed, which is added to the tracking uncertainty. It is shown for all particles in Fig. 5.7 on the top left.

#### Secondary correction

The fit quality of the  $DCA_{xy}$ -fits for the secondary correction is comparably good, nevertheless it relies on Monte Carlo information to some extent. Several checks have been performed to estimate the uncertainty of the procedure:

- The scaled sum of the templates is compared to the data distribution.
- The composition of particles that feed into the protons was changed, leading to a change in the shape of the weak template, due to the different  $c\tau$ . In particular the  $\Sigma/\Lambda$  ratio was changed by a factor  $\pm 3$ .



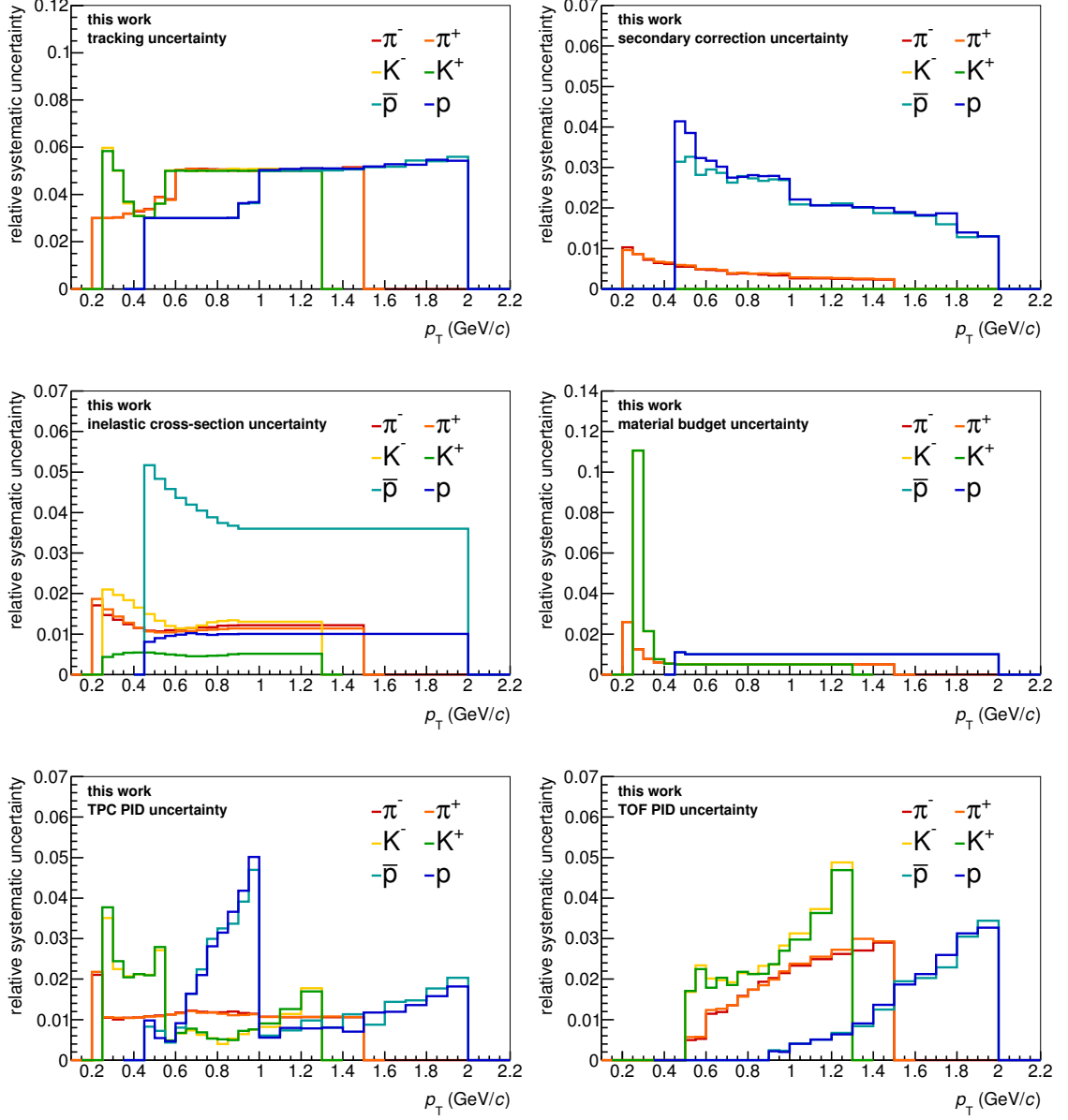


Fig. 5.7.: Sources of systematic uncertainties. Going from left to right and top to bottom the following sources of systematic uncertainties have been considered: tracking, secondary correction, inelastic cross-section, material budget, TPC PID and TOF PID.

- The fit range of the  $DCA_{xy}$  fit was changed from  $DCA_{xy} < \pm 3$  to  $DCA_{xy} < \pm 2$ ,  $DCA_{xy} < \pm 1$ ,  $DCA_{xy} < 0$  and  $DCA_{xy} > 0$ .

The most significant deviation was found for the first check. Looking at the difference of the summed templates to the data a 20% deviation was found in the shoulders of the DCA distribution. Since the weak decay template is mostly fitted to the shoulders, this is conservatively propagated with a 20% systematic uncertainty on the secondary correction. The size of the uncertainty is shown in Fig. 5.7 on the top right.

### Particle Identification

To evaluate the systematic uncertainty of the particle identification the  $\pm 3\sigma$  cut on the PID signals is changed to  $\pm 2\sigma$  and  $\pm 4\sigma$  for both the TPC and TOF signal individually. The differences are directly propagated as systematic uncertainties. For kaons an additional uncertainty due to the electron subtraction is added quadratically to the TPC PID uncertainty. The uncertainties are shown in Fig. 5.7 at the bottom left for the TPC (1-5%) and on the right for TOF (2-5%).

### Other Systematic Uncertainties

In addition to the uncertainties discussed above an uncertainty for the material budget and the inelastic cross-section is assigned, which is shown in the middle of Fig. 5.7 on the left and on the right, respectively. They have been taken from the analysis of pion, kaon and proton production in Pb-Pb collisions [ALICE13b, ALICE12a]. The uncertainty on the inelastic cross-section is around 1% for all particles except protons ( $\sim 5\%$ ). The material budget uncertainty is mostly relevant for very low  $p_T$  kaons (11%) and amounts to only about 1% for all other cases.

### Full Systematic Uncertainties

The full systematic uncertainties as function of  $p_T$  are shown in Fig. 5.8 for all particles. The single contributions have been summed quadratically to obtain the full uncertainty. While the uncertainties of pions and kaons are dominated by the tracking and PID, the secondary correction also contributes significantly for protons and anti-protons. For anti-protons the uncertainty on the inelastic cross-section is

also significant. In total, the systematic error is around 4-7% for all particles over the majority of the  $p_T$ -range.

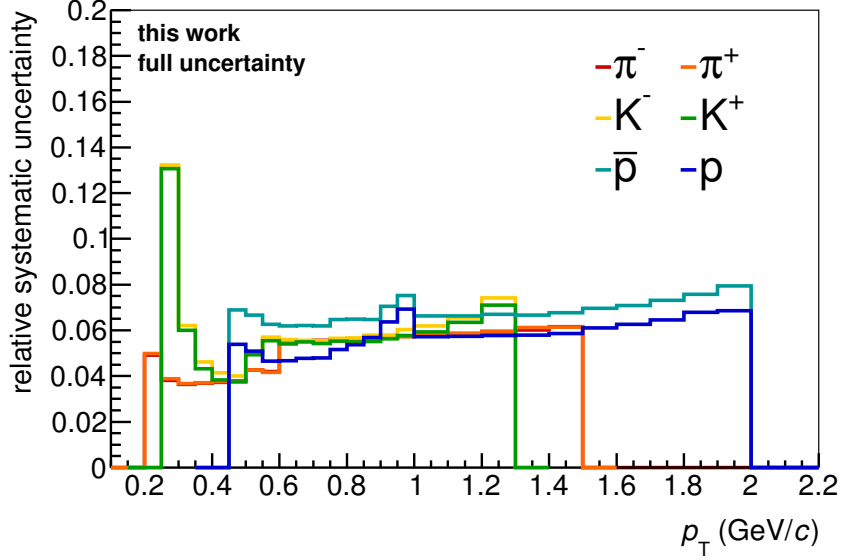


Fig. 5.8.: Full systematic uncertainties of  $\pi^\pm$ ,  $K^\pm$  and  $p(\bar{p})$  as a function of  $p_T$ .

Most uncertainties that have been calculated are partly or fully correlated over the different multiplicity classes. To be able to interpret the change of the spectral shape and particle yields with multiplicity better, the uncorrelated uncertainties have been calculated as well by normalizing with the minimum bias spectra. The uncorrelated uncertainty on the yield  $N$  of one  $p_T$ -bin in a given multiplicity bin introduced by changing the value of a parameter from the default  $A$  to  $B$  is given by the double ratio

$$\Delta_{uncorr} = \frac{\frac{N_B}{N_{B,minbias}}}{\frac{N_A}{N_{A,minbias}}} \quad (5.3)$$

The uncorrelated uncertainties have been calculated for all the contributions above and are in particular important for the interpretation of the spectral shape evolution with multiplicity, when looking at the particle ratios  $p/\pi$  and  $K/\pi$  in Section 5.3.1.

## 5.2. Other Particle Identification Methods Used in ALICE

In this section other PID methods, which cover different  $p_T$  ranges than the TPC-TOF method, are introduced. The transverse momentum spectra obtained with the different methods have been combined and published in [ALICE14h].

### 5.2.1. ITS Standalone Analysis

With the *ITS standalone* method (ITSsa) it is possible to identify particles with transverse momenta as low as 100 MeV/ $c$ . This requires an independent track reconstruction, that relies on ITS information only, because these low momentum particles do not reach the TPC.

As discussed in the detector introduction (cf. Section 3.1) four of the six ITS layers give a  $dE/dx$  signal. The most probable PID is assigned to a track by combining the layer responses. Details can be found in [ALICE12a].

Fig. 3.2 shows the  $dE/dx$  distribution measured with the ITS as a function of the particle momentum. The bands for different particles are clearly visible. Reconstruction and separation are possible between 100–700 MeV/ $c$ , 200–600 MeV/ $c$  and 300–650 MeV/ $c$  for  $\pi$ , K and p, respectively. This gives some overlap at low  $p_T$  with the TPC-TOF method (about 150–500 MeV/ $c$ ) and therefore allows to validate both methods in this region.

### 5.2.2. Statistical Identification with TOF

This method is based on the time-of-flight measured with the TOF detector. The TOF performance has already been shown in Fig. 3.4. The method relies on a statistical identification of particles by fitting the time-of-flight signal with detector response templates. As mentioned earlier this allows to go to higher transverse momenta, but has the drawback that particles can not be identified on a track-by-track basis.

Fig. 5.9 shows an example for a fit of the TOF signal for  $2.4 < p_T < 2.5$  GeV/ $c$ . In this case the kaon mass is assumed and the signal is plotted as a function of number of sigmas for the kaon mass hypothesis. The expected signal shapes for pions, kaons,

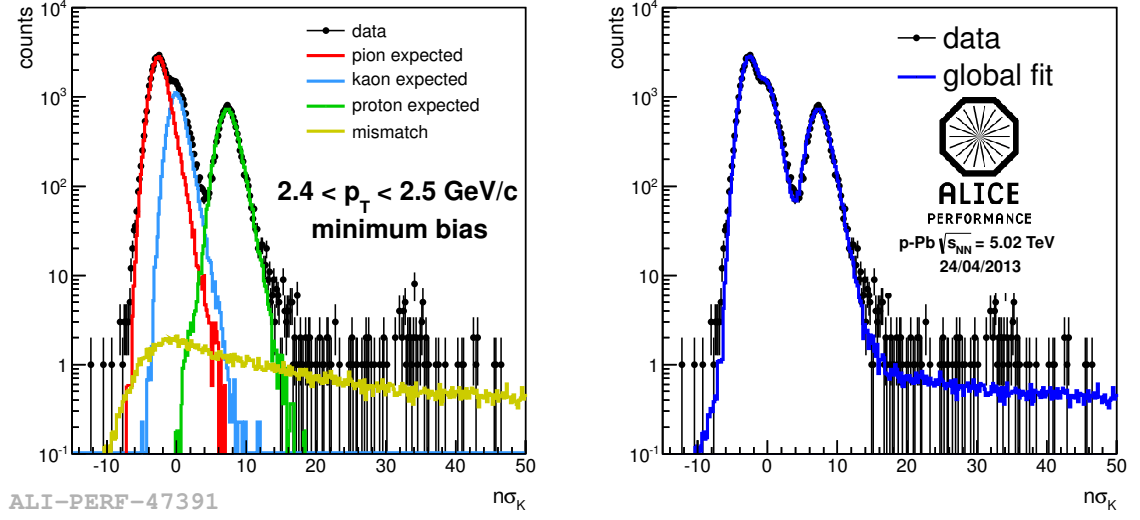


Fig. 5.9.: Example for a TOF signal fit. In this case the kaon hypothesis is used and the signal is plotted as a function of number of sigmas with respect to the kaon hypothesis. The signal is fitted with detector response templates for pions, kaons, protons and mismatched particles. On the right the resulting fit is shown.

and protons are then fitted to the signal. In addition a template for mismatched tracks has to be taken into account. On the right side of the figure the fit result is shown. A good separation is possible between 0.5–3.0 GeV/ $c$ , 0.5–2.5 GeV/ $c$  and 0.5–4.0 GeV/ $c$  for  $\pi$ , K and p, respectively. This gives some overlap at intermediate  $p_T$  with the TPC-TOF method and allows to validate both methods.

### 5.2.3. Statistical Identification with TPC

Like the TOF signal, the TPC signal can also be used for a statistical identification of particles. The method is called *relativistic rise TPC* and uses an unfolding method applied in the relativistic rise region of the Bethe-Bloch energy loss. Momenta as high as 20 GeV/ $c$  can be reached with this approach. At low  $p_T$  (2 GeV/ $c$  for pions, 3 GeV/ $c$  for kaons and protons) it is limited by the separation power of the  $dE/dx$  signal. The overlap between the three particles in the energy loss distribution is significant and a careful tuning and knowledge of the TPC parametrization is necessary to perform this analysis (compare Fig.5.10 on the left).

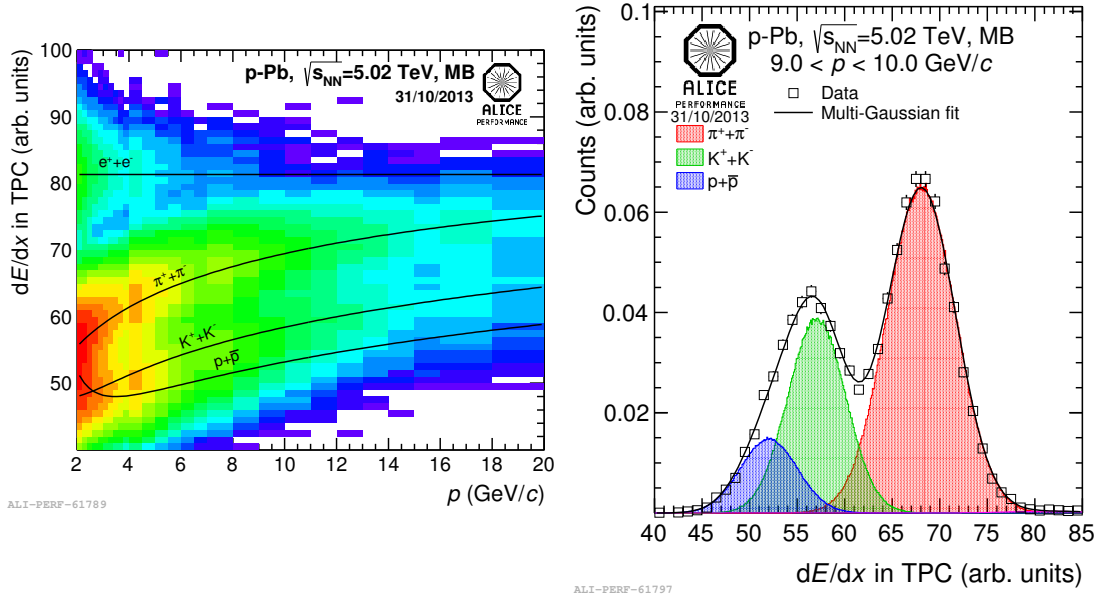


Fig. 5.10.: Particle identification with the TPC in the relativistic rise region of the energy loss. On the left is the TPC signal as a function of momentum zoomed into high  $p_T$ . The black lines indicate the parametrizations, i.e. the expected signal for a given particle. On the right an example of the fit with multiple Gaussians is shown.

The TPC signal is fitted for each  $p_T$ -bin with multiple Gaussians to extract the fractions of each particle (compare Fig.5.10 on the right). The fractions and the measured transverse momentum distribution of all charged particles are then used to calculate the particle yield in the corresponding  $p_T$ -bin. For more details please refer to [ALICE14j].

### 5.3. Transverse Momentum Distributions of Pions, Kaons and Protons

The measurement of the transverse momentum distributions of pions, kaons and protons with the TPC-TOF method, which was performed within this work, was extended to very low  $p_T$  with the ITS standalone method and to high  $p_T$  with the

TOF fits method. This resulted in the common publication [ALICE14h] together with the transverse momentum distributions of strange particles ( $K_S^0$ ,  $\Lambda$  and  $\bar{\Lambda}$ ).

For the combination of the spectra parts from the different analysis it is advantageous that the ITS standalone method as well as the TOF fit method have an overlap with the TPC-TOF spectra. To combine the spectra in these overlap regions the points are weighted with their systematic uncertainties.

The TPC-TOF and TOF fit methods are based on the same track sample, i.e. global tracks, and share all sources of systematic uncertainties, except on the PID method. To combine these two partial spectra only the error on the PID method is used as a weight. All common systematic uncertainties are then assigned after the combination. The ITS standalone method is based on a completely different tracking, much less detector material is crossed and the secondary subtraction is done individually. Therefore the full systematic uncertainties are used as weights to combine the TPC-TOF and ITS standalone spectra. The agreement between the different methods is very good and is well within the systematic uncertainties.

As expected for collisions at LHC energies, the particle and anti-particle abundances are consistent and the measured particle and anti-particle spectra are identical, because no or very little baryon transport to mid-rapidity is predicted. Therefore the final spectra are presented as the sum of particle and anti-particle. This observation was already made for the measured spectra in Pb-Pb collisions [ALICE13b, ALICE12a]. Dedicated studies of anti-baryon to baryon ratios have been published in [ALICE10, ALICE14q] and are consistent with unity or very close to unity at the LHC, regardless of the collision system.

The final  $p_T$ -invariant spectra are shown in Fig. 5.11 for the six multiplicity classes, which have been defined in Section 5.1.2. A hardening of the spectra with increasing multiplicity and particle mass is visible, which becomes more evident when looking at particle ratios. They will be discussed in the following subsection.

Also shown is an individual fit to the spectra with the Blast-Wave function [SSH93] (cf. Section 5.3.3) to extrapolate to high and low  $p_T$  for the integrated yields  $dN/dy$  and  $\langle p_T \rangle$ . The systematic uncertainty consists of two components: the fit variation within the systematic uncertainties and the extrapolation to low and high  $p_T$ .

The fit variation is performed by shifting the central data points in each  $p_T$ -bin to the low and high edges of the systematic uncertainties. For the  $\langle p_T \rangle$  the spectral

## 5. Production of Pions, Kaons and Protons in $p$ -Pb Collisions

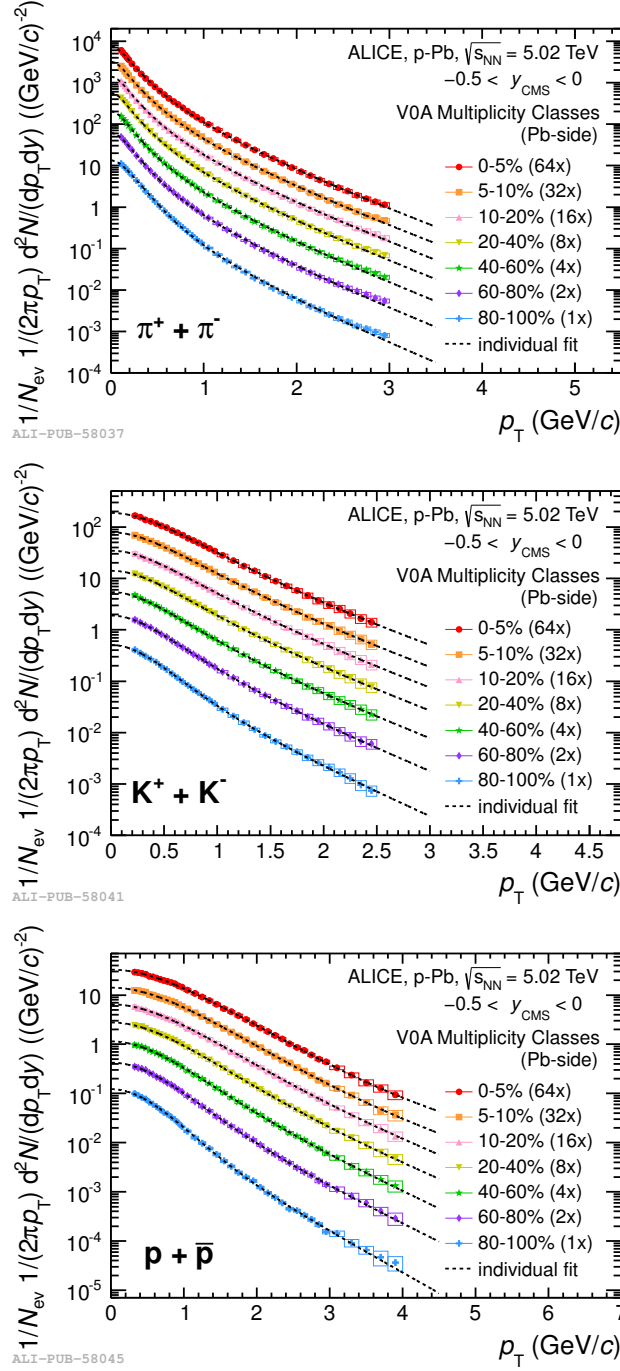


Fig. 5.11.: Invariant  $p_T$ -differential yields of pions, kaons and protons for six multiplicity classes. Shown are statistical uncertainties (bars) and systematic uncertainties (boxes). A hardening of the spectra with increasing multiplicity and particle mass is visible. The black dotted lines indicate individual Blast-Wave fits to extrapolate to low and high  $p_T$ . The spectra have been scaled with  $2^n$  for visibility. Also published in [ALICE14h].



### 5.3. Transverse Momentum Distributions of Pions, Kaons and Protons

<b>Pions (<math>\pi^+ + \pi^-</math>)</b>				
Multiplicity	dN/dy	statistical	systematic	uncorrelated
0-5%	40.807	$\pm 0.018$	$\pm 1.985$	$\pm 1.074$
5-10%	33.084	$\pm 0.016$	$\pm 1.586$	$\pm 0.848$
10-20%	28.056	$\pm 0.011$	$\pm 1.330$	$\pm 0.708$
20-40%	21.748	$\pm 0.007$	$\pm 1.010$	$\pm 0.543$
40-60%	15.290	$\pm 0.006$	$\pm 0.708$	$\pm 0.382$
60-80%	9.455	$\pm 0.004$	$\pm 0.440$	$\pm 0.230$
80-100%	4.314	$\pm 0.003$	$\pm 0.195$	$\pm 0.106$

<b>Kaons (<math>K^+ + K^-</math>)</b>				
Multiplicity	dN/dy	statistical	systematic	uncorrelated
0-5%	5.836	$\pm 0.012$	$\pm 0.500$	$\pm 0.258$
5-10%	4.636	$\pm 0.010$	$\pm 0.367$	$\pm 0.179$
10-20%	3.890	$\pm 0.006$	$\pm 0.300$	$\pm 0.140$
20-40%	2.954	$\pm 0.004$	$\pm 0.218$	$\pm 0.100$
40-60%	2.027	$\pm 0.003$	$\pm 0.142$	$\pm 0.065$
60-80%	1.219	$\pm 0.002$	$\pm 0.078$	$\pm 0.035$
80-100%	0.529	$\pm 0.001$	$\pm 0.032$	$\pm 0.017$

<b>Protons (<math>p + \bar{p}</math>)</b>				
Multiplicity	dN/dy	statistical	systematic	uncorrelated
0-5%	2.280	$\pm 0.004$	$\pm 0.159$	$\pm 0.070$
5-10%	1.854	$\pm 0.004$	$\pm 0.128$	$\pm 0.055$
10-20%	1.577	$\pm 0.003$	$\pm 0.108$	$\pm 0.045$
20-40%	1.222	$\pm 0.002$	$\pm 0.082$	$\pm 0.033$
40-60%	0.862	$\pm 0.001$	$\pm 0.056$	$\pm 0.023$
60-80%	0.534	$\pm 0.001$	$\pm 0.034$	$\pm 0.014$
80-100%	0.231	$\pm 0.001$	$\pm 0.015$	$\pm 0.007$

Table 5.3.: Integrated yields dN/dy of pions, kaons and protons. The sum of particle and anti-particles are shown, since they are in agreement with each other. In addition to the statistical and full systematic uncertainties the multiplicity uncorrelated systematic uncertainties are shown.

shape is varied by shifting the central values at low  $p_T$  to the high (low) uncertainty edge and at high  $p_T$  to the low (high) edge. These maximum deviations are then divided by  $\sqrt{3}$  to obtain the root mean square uncertainty.

To evaluate the uncertainty on the extrapolation several fit functions [STAR09] have been tested: Boltzmann,  $m_T$ -exponential,  $p_T$ -exponential, Tsallis-Levy, Fermi-Dirac and Bose-Einstein. Fit functions that fail to describe the data over the full  $p_T$ -range, have been limited to low  $p_T$ . The differences of the various extrapolations is then propagated as the systematic uncertainty, which amounts to about 2%. For high (low) multiplicity the fraction of the extrapolated yield amounts to 8% (9%), 10% (12%) and 7% (12%) for  $\pi^\pm$ ,  $K^\pm$  and  $p(\bar{p})$ , respectively.

The statistical uncertainty on the yield is obtained by shifting the central value of each bin randomly with a Gaussian distribution within the statistical uncertainty. This procedure is repeated 1000 times and the resulting distribution of yields is fitted with a Gaussian, too. The width of this Gaussian is then propagated as the statistical uncertainty of the yield  $dN/dy$ .

The integrated yields  $dN/dy$  of pions, kaons and protons are listed in Table 5.3 with the statistical, full systematic and the multiplicity uncorrelated uncertainties. The sum of particle and antiparticle is shown.

The published spectra have been extended to  $p_T$  as high as 15 GeV/ $c$  by preliminary results obtained with the TPC relativistic rise method [ALICE14r].

### 5.3.1. Particle Ratios

The particle chemistry of p-Pb collisions can be studied by comparing the abundancies of the different particles. The integrated proton and kaon yields  $dN/dy$  normalized to the integrated pion yield as a function of charged multiplicity at mid-rapidity are shown in Fig. 5.12. The results from p-Pb collisions are compared to d-Au collisions from STAR and heavy-ion collisions from the LHC and RHIC [STAR09, PHENIX04b, BRAHMS05a, ALICE13b, PHENIX13b].

For p-Pb collisions the multiplicity uncorrelated systematic uncertainties have been plotted in addition to the full systematic errors. There is no multiplicity dependence for the  $p/\pi$  ratio in p-Pb collisions. For Pb-Pb collisions an indication for a small decrease of the ratio at high multiplicity could be argued. For the  $K/\pi$  ratio there

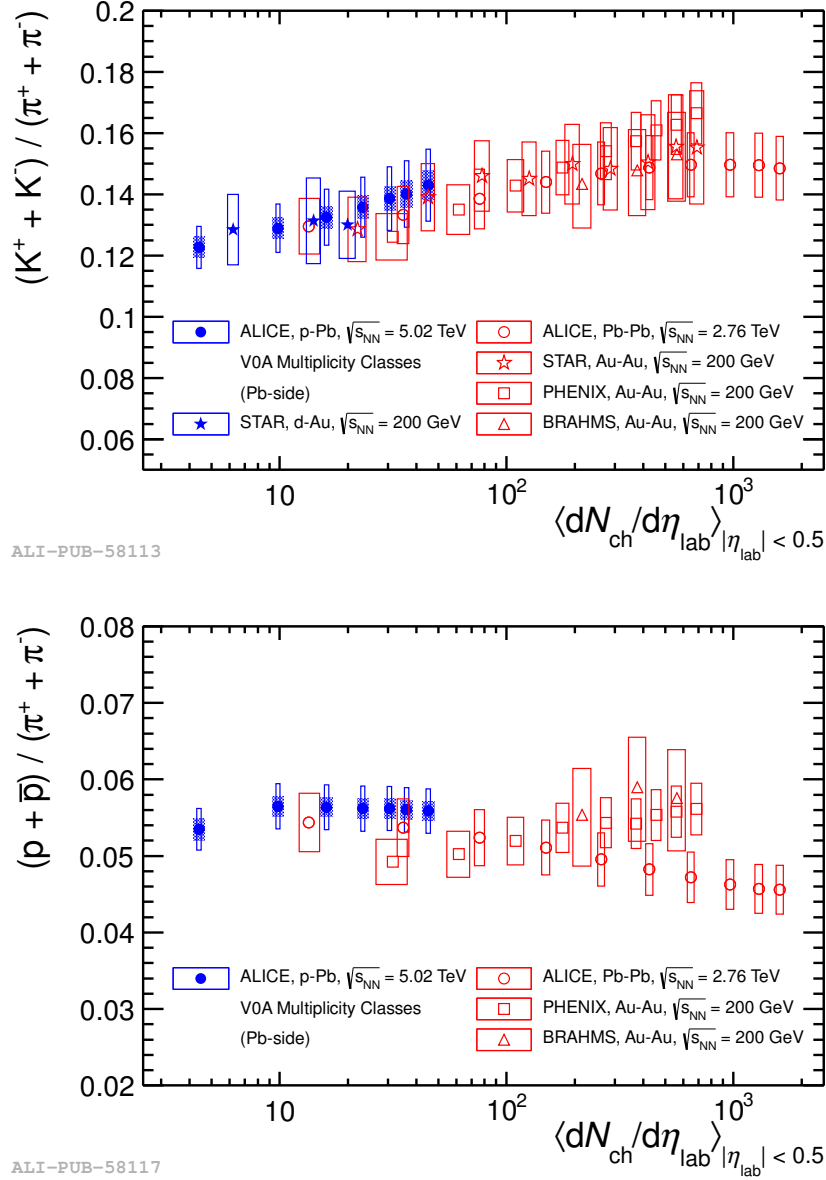


Fig. 5.12.: Integrated kaon and proton yield  $dN/dy$  normalized to the pion yield as a function of charged particle multiplicity at mid-rapidity for different collision systems and energies (see the text for references). For p-Pb the multiplicity uncorrelated systematic uncertainties have been drawn as shaded boxes in addition to the full systematic uncertainties. For the  $p/\pi$  ratio no evolution with multiplicity is observed in p-Pb, but for the  $K/\pi$  ratio a small increase is observed as in the other systems. Also published in [ALICE14h].

is a small increase with multiplicity for  $p$ -Pb collisions, which becomes in particular visible due to the uncorrelated uncertainties. The increase with multiplicity is also compatible with the ratios from heavy-ion collisions and d-Au collisions and is typically attributed to a reduced canonical suppression of strangeness production in larger freeze-out volumes [SBRS98] or to an enhanced strangeness production in a quark-gluon-plasma [LR07]. The increase of strange particles normalized to pions is also observed for  $\Lambda$ s [ALICE14h] and multi-strange baryons [ALICE14k] in  $p$ -Pb collisions at the LHC.

As discussed before the hardening of the spectra with multiplicity is stronger for heavier particles. This can be made more visible by looking at the particle ratios  $K/\pi$  and  $p/\pi$  as a function of  $p_T$  for different multiplicity classes. This is shown in Fig. 5.13, where the ratio is plotted for a low and a high multiplicity (centrality) class for  $p$ -Pb and Pb-Pb collisions. For  $p$ -Pb collisions the multiplicity uncorrelated uncertainties are plotted again as shaded boxes. When comparing the high to the low multiplicity ratio a clear enhancement at intermediate  $p_T$  is seen. In addition, for the  $p/\pi$  ratio a corresponding depletion at low  $p_T$  is evident. This indicates a push of protons from low momentum to intermediate  $p_T$  in high multiplicity events. This is also supported by the constant integrated  $p/\pi$  ratio. The same effect is observed in Pb-Pb collisions, although the effect is much stronger there. In heavy-ion collisions this is interpreted as a signature of collective flow or quark recombination [FMNB03, Boz12b, MSW12].

With the extension to higher  $p_T$  [ALICE14r] the ratios have been presented up to 15 GeV/ $c$ , which show that the shift in the spectral shape for heavier particles is a low to intermediate  $p_T$  effect, since the ratios converge to the same value for all multiplicities at high  $p_T$ . For  $p/\pi$  the ratio drops to roughly 0.1 above 8 GeV/ $c$  for all multiplicities in  $p$ -Pb and Pb-Pb and the  $K/\pi$  ratio rises and then saturates at roughly 0.5 above 6 GeV/ $c$ . Please note that the same enhancement with the corresponding depletion is observed for the  $\Lambda/K_S^0$  ratio [ALICE14h], which points towards a mass dependence and not a dependence on the valence quark flavor.

The observed effects in  $p$ -Pb collisions do not depend strongly on the multiplicity selection. As an alternative to the V0A multiplicity selection, the number of clusters in the first ITS layers, the sum of V0A and V0C and the energy deposited in the ZNA have been tested. While the  $p/\pi$  ratio is essentially the same for the

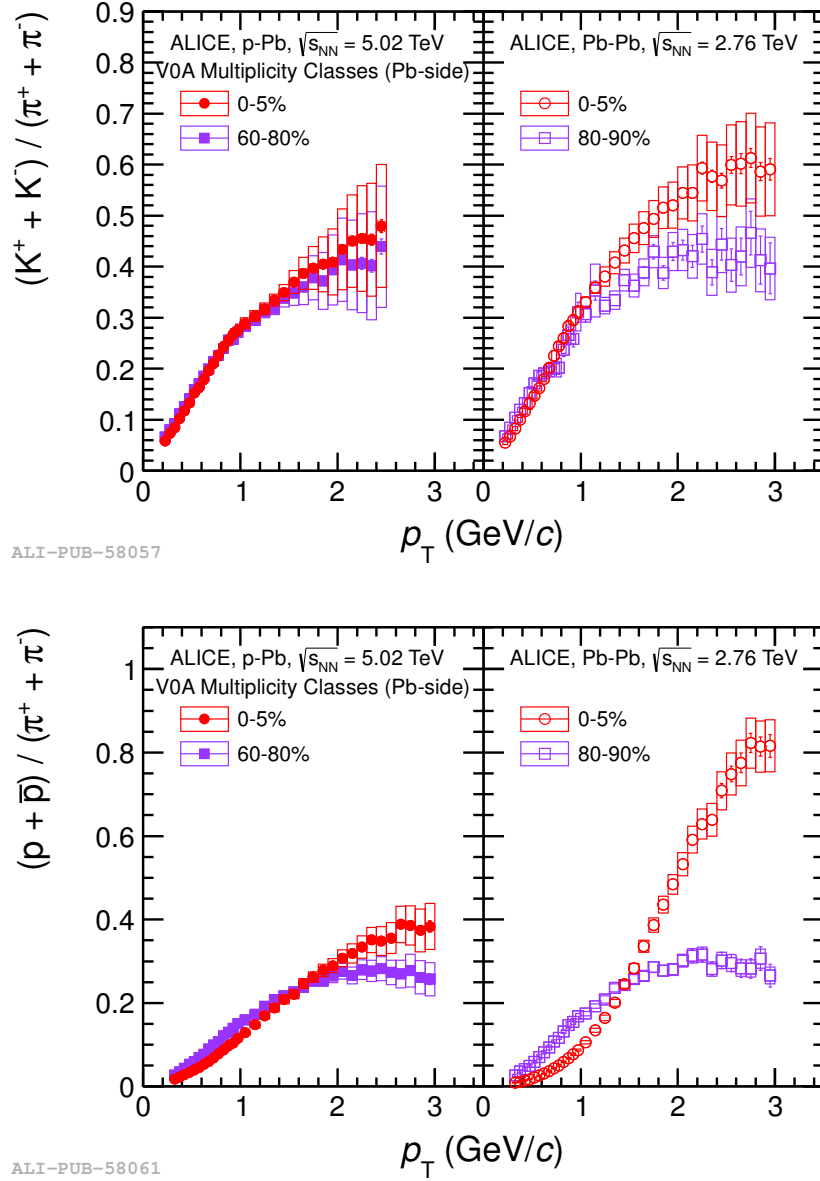


Fig. 5.13.: Kaon and proton to pion ratio as function of  $p_T$  for a high and a low multiplicity class in p-Pb on the left and a high and low centrality class in Pb-Pb on the right. Multiplicity uncorrelated uncertainties are drawn as filled boxes, which are mostly covered by the markers (not available for Pb-Pb). In p-Pb a clear enhancement of the ratios at intermediate  $p_T$  is visible for high multiplicities with respect to low multiplicities. For the  $p/\pi$  ratio a corresponding depletion at low  $p_T$  is also visible. The same qualitative effect is observed for Pb-Pb collisions. Also published in [ALICE14h].

0-5% multiplicity classes, the 60-80% class selected with ZNA is  $\sim 15\%$  higher at  $p_T \sim 3$  GeV/ $c$  with respect to the default selection with the V0A. This does not change the overall picture of the enhancement at intermediate  $p_T$ . One reason for the observed difference is given by the mild correlation of events at forward and central rapidity: the lowest multiplicity class selected with ZNA leads to a larger multiplicity at mid-rapidity than the corresponding class selected with V0A.

### A More Quantitative Approach

To be able to compare the different collision systems in a more quantitative way, the proton over pion ratio has been plotted as a function of charged particle multiplicity at mid-rapidity for each  $p_T$ . In Fig. 5.14 in the top panel this is shown for p-Pb and Pb-Pb and three selected  $p_T$ -bins. The dotted lines are individual power-law fits as function of multiplicity corresponding to the functional form

$$y = A \cdot \langle dN_{ch}/d\eta_{lab} \rangle^B \quad (5.4)$$

Remarkably, the  $p/\pi$  ratio seems to follow the same power-law behavior for the same  $p_T$  in p-Pb and Pb-Pb collisions as a function of charged multiplicity. This is shown in Fig. 5.14 in the middle, where the exponent  $B$  from the fit is plotted as a function of  $p_T$  for the two systems. Within the uncertainties the extracted  $B$  is in good agreement for the two systems over the whole  $p_T$ -range, which suggests that the driving force of the  $p/\pi$  ratio seems to be the charged multiplicity at mid-rapidity.

The same scaling behavior is observed for the  $\Lambda/K_S^0$  ratio, which was reported in the common transverse momentum distribution publication [ALICE14h]. For  $\Lambda$  and  $K_S^0$  preliminary data from pp collisions at  $\sqrt{s_{NN}} = 7$  TeV as a function of multiplicity are available and the same procedure has been applied to the spectra. The extracted exponent  $B$  for the  $\Lambda/K_S^0$  ratio for all three collision systems is shown in Fig. 5.14 at the bottom. The pp data is compatible with the same scaling behavior as for p-Pb and Pb-Pb collisions.

Please note that the multiplicity of the pp data has been selected at mid-rapidity, i.e. in the same pseudorapidity-region the measurement is performed in. It is known from generator studies that this can introduce an auto-correlation bias. This has to

### 5.3. Transverse Momentum Distributions of Pions, Kaons and Protons

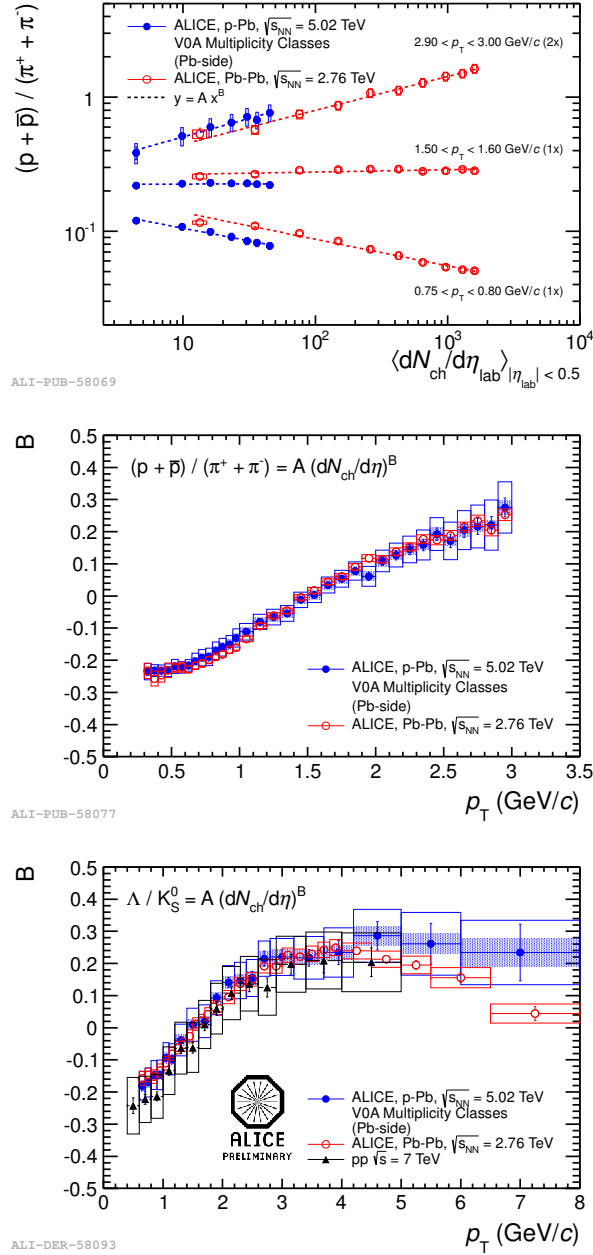


Fig. 5.14.: The top plot shows the  $p/\pi$  ratio for three selected  $p_T$ -bins as a function of charged particle multiplicity at mid-rapidity for p-Pb and Pb-Pb collisions. They have been fitted with a power-law and the exponent  $B$  is then plotted as a function of  $p_T$  in the middle plot. The exponent is in good agreement for the two collision systems. In the bottom plot the same is shown for the  $\Lambda/K_S^0$  ratio, where also preliminary pp data is available, which is also compatible with the other two systems. Top and middle figure are also published in [ALICE14h]. Bottom figure published in [ALICE14n]

be kept in mind, when interpreting the results of transverse momentum distributions as a function of multiplicity from pp collisions.

### 5.3.2. Mean Transverse Momentum

The mean transverse momentum  $\langle p_T \rangle$  of identified particles can be studied to estimate the hardness of a spectrum in first order. In pp [CMS12d] and Pb-Pb collisions [ALICE13b] a mass ordering of  $\langle p_T \rangle$  was observed. This means that  $\langle p_T \rangle$  is higher for heavier particles at the same multiplicity, but also rises at a steeper rate with multiplicity. The same behavior is observed for p-Pb collisions, which is shown in Fig. 5.15 for pions, kaons, protons and lambdas. This is an indication that a mass-dependent effect pushes particles to higher transverse momenta.

The  $\langle p_T \rangle$  of pions, kaons and protons as a function of charged particle multiplicity in p-Pb collisions is also compared to heavy-ion collisions in Fig. 5.15 on the top right and the bottom [PHENIX04b, BRAHMS05a, ALICE14h, STAR09]. In general, the  $\langle p_T \rangle$  in p-Pb is higher compared to heavy-ion collisions at the same charged multiplicity. It is also worth noting that the  $\langle p_T \rangle$  of protons in high multiplicity p-Pb collisions is lower than the one in the most central Pb-Pb collisions, while this is not the case for pions, but could be argued for the kaons. Please note that selecting high multiplicity events in p-Pb could bias the selection towards events that contain hard collisions.

### 5.3.3. Blast-Wave Fits

In heavy-ion collision the behavior of the transverse momentum distributions, i.e. the hardening of the spectra with multiplicity and the mass ordering, are typically discussed within the collective radial expansion of the collision system. Several hydrodynamic models, like the Kraków model [BWP12], HKM [KSW13], EPOS [WKB<sup>+</sup>12] and VISH2+1 [SHHS11], have been developed to predict and describe the data in heavy-ion collisions. The spectra of this work will also be compared to some of the models in Section 5.3.5.

A comparably simple tool to test the hydrodynamic picture with identified particle spectra is the Blast-Wave model [SSH93]. It assumes a hard sphere uniform density particle source with temperature  $T$ , which undergoes an instantaneous common



### 5.3. Transverse Momentum Distributions of Pions, Kaons and Protons

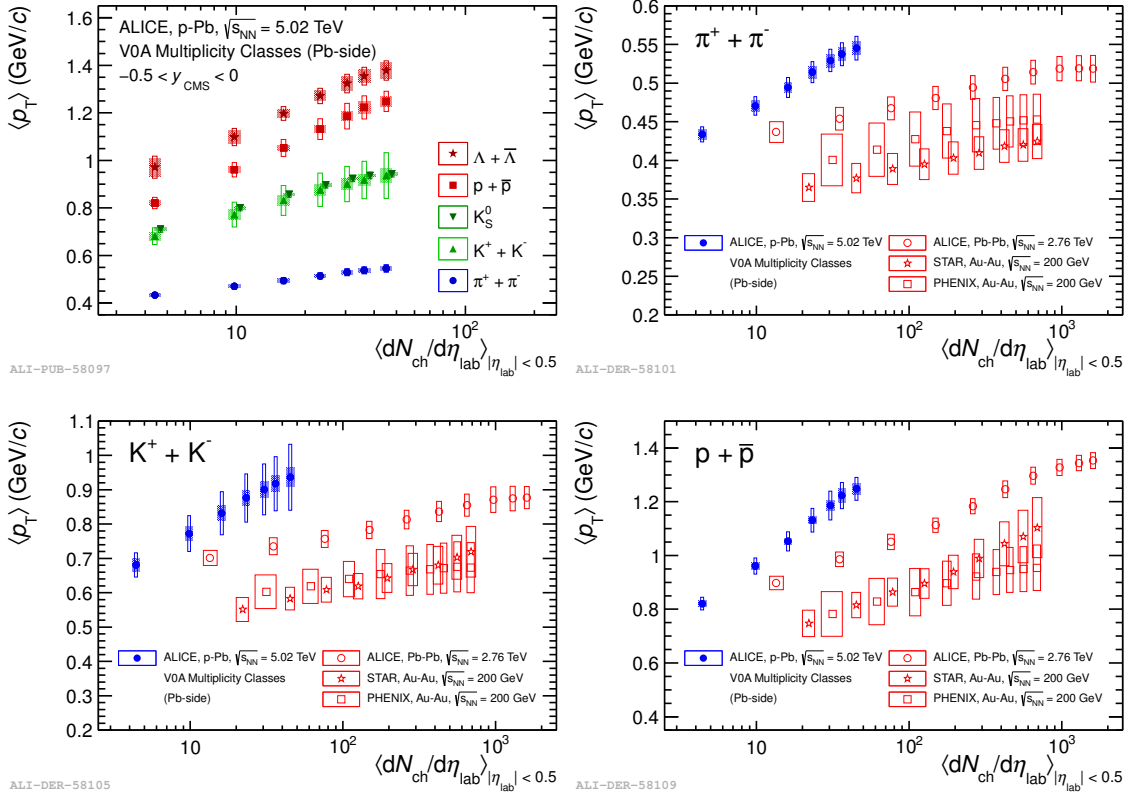


Fig. 5.15.: On the top left the  $\langle p_T \rangle$  of pions, kaons, protons and lambdas as a function of charged particle multiplicity is shown. In general the  $\langle p_T \rangle$  rises with multiplicity. Also, a clear mass ordering is seen, i.e. the  $\langle p_T \rangle$  is higher for heavier particles and rises at a steeper rate with multiplicity. The  $\langle p_T \rangle$  of pions (top right), kaons (bottom left) and protons (bottom right) are also compared to heavy-ion collisions from RHIC and the LHC. The multiplicity uncorrelated uncertainties are plotted as shaded boxes. Top left figure also published in [ALICE14h]. Top right and bottom figures are derived from the sources mentioned in the text.

freeze-out and a collective transverse radial flow velocity  $\beta$ . The transverse velocity distribution  $\beta_r(r)$  for  $0 < r < R$  is parametrized with the velocity  $\beta_s$  at the surface ( $r = R$ ) of the medium and the velocity profile  $n$ :

$$\beta_r(r) = \beta_s \left( \frac{r}{R} \right)^n \quad (5.5)$$

The resulting spectrum is the superposition of the individual thermal components, each boosted with the boost angle  $\rho = \tanh^{-1} \beta_r$ .

$$\frac{1}{p_T} \frac{dN}{dp_T} \propto \int_0^R r \, dr \, m_T \, I_0 \left( \frac{p_T \sinh \rho}{T_{\text{kin}}} \right) K_1 \left( \frac{m_T \cosh \rho}{T_{\text{kin}}} \right) \quad (5.6)$$

Here  $I_0$  and  $K_1$  are the modified Bessel functions and  $T_{\text{kin}}$  is the kinetic freeze-out temperature. This leaves the three free parameters  $T_{\text{kin}}$ ,  $\beta_s$ ,  $n$  and a normalization parameter.

This functional form has already been used to extrapolate the yield  $dN/dy$  of the spectra to low and high  $p_T$ . If it is used to fit all particle species simultaneously it can provide insight into the kinetic freeze-out properties of the collision system under investigation. Although the Blast-Wave model makes some general assumptions and has obvious limitations, like the substantial dependence on the chosen fit range [ALICE13b], it is a practical tool, which allows to compare transverse momentum distributions from different collision systems with a small set of parameters.

The pion, kaon and proton spectra have been fitted in all multiplicity classes with the Blast-Wave functional form introduced above. For the fits performed here, the same fit ranges as in [ALICE13b, ALICE12a] were chosen, i.e. 0.5–1.0 GeV/ $c$ , 0.2–1.5 GeV/ $c$  and 0.3–3.0 GeV/ $c$  for pions, kaons and protons, respectively. They have been defined on the basis of the availability of low  $p_T$  data points and in case of pions very low momenta are not considered, because of feed-down from resonances. At high  $p_T$  the ranges are limited by the agreement with the data. This is justified by the fact that hydrodynamics mostly affects low to intermediate  $p_T$  and the underlying assumptions of the Blast-Wave model are not expected to be valid at high  $p_T$ .

An example of the model fit and the fit quality is shown in Fig. 5.16 on the left for the 0-5% multiplicity bin. Within the fit ranges good agreement between the data and the model fit can be observed in the ratio plots at the bottom. The fit quality is reasonable for all multiplicity bins, although they are not shown here. On the right the spectra of  $K_S^0$ ,  $\Lambda$ ,  $\Xi$  and  $\Omega$  have been added to the common fit, which causes negligible differences in the extracted fit parameters. In fact, the Blast-Wave fit to pions, kaons and protons can be used to predict the strange particle spectra by using the parameters from the fit and plugging in the masses of the strange particles.

### 5.3. Transverse Momentum Distributions of Pions, Kaons and Protons

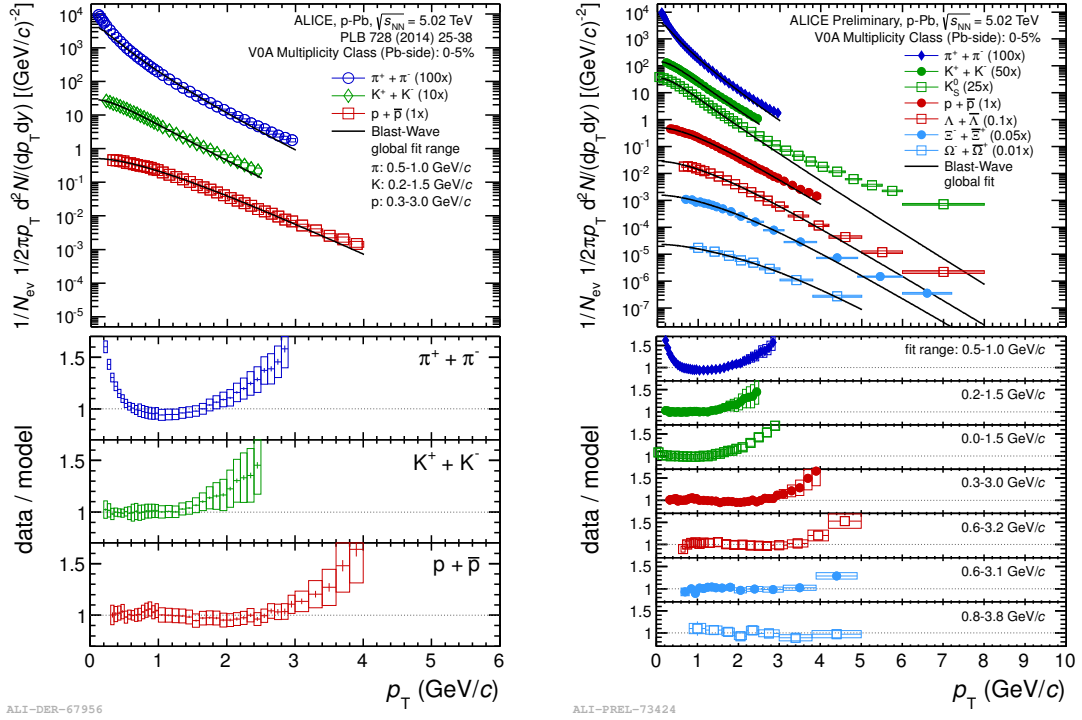


Fig. 5.16.: Blast-Wave fit to pions, kaons and protons from p-Pb collisions (left). The fit quality is good within the fit ranges and deviations are seen at higher  $p_T$  as expected. On the right strange and multi-strange particles have been added to the common fit, which has a negligible effect on the extracted fit parameters. The left Figure was also published in [ALICE14h] and the right one is from [ALICE14k].

Furthermore, it is evident that the Blast-Wave model fit can describe the particle spectra of heavier particles up to higher transverse momenta.

For the variation of the fit ranges as in [ALICE13b, ALICE12a] shifts of about 10% of the fit parameters are observed. While these differences seem to be large, one has to keep in mind that they are largely correlated across multiplicity, which means that observations about the trend with multiplicity are not or only little affected.

The results of Blast-Wave fits to the Pb-Pb data at  $\sqrt{s_{NN}} = 2.76$  TeV have already been presented in [ALICE13b] and are shown exemplary on the left for the most central Pb-Pb collisions in Fig. 5.17. For pp collisions preliminary spectra as a function of multiplicity are available and have also been fitted. As an example the fit of the events with the highest multiplicity are shown in Fig. 5.17 on the right. The event

## 5. Production of Pions, Kaons and Protons in p-Pb Collisions

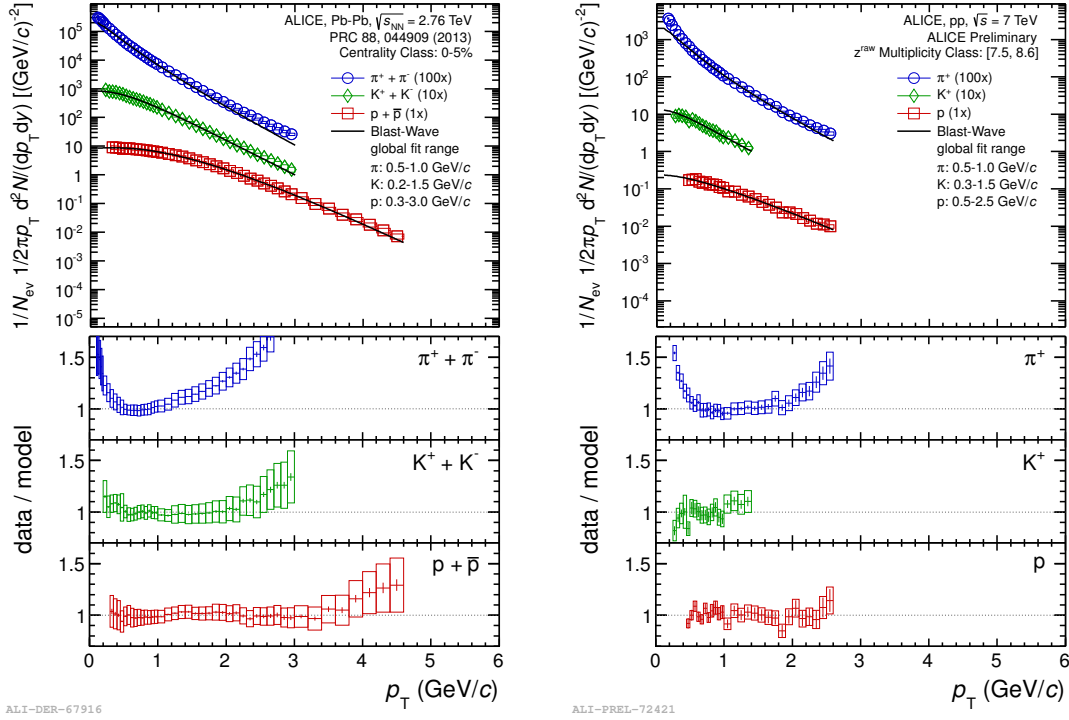


Fig. 5.17.: Blast-Wave fit quality for pp and Pb-Pb collisions. In pp a high multiplicity event class, which corresponds to a multiplicity that is 7.5 to 8.6 times higher than minimum bias pp collisions, was fitted. For Pb-Pb the fit to the 5% most central events is shown. Figures from [ALICE13b, ALICE14m].

class contains all events that have a 7.5 to 8.6 higher multiplicity at mid-rapidity than minimum bias pp collisions at  $\sqrt{s_{NN}} = 7$  TeV. The multiplicity  $N_{ch}^{raw}$  is measured in a window of  $|\eta| < 0.8$  and the following classes are defined: 7-12, 13-19, 20-28, 29-39, 40-49, 50-59, 60-71 and 72-82. As for the particle ratios, please note that a potential selection bias might be introduced due to the multiplicity selection. Also, the preliminary spectra are not available in the same  $p_T$  ranges as the p-Pb and Pb-Pb spectra. As a consequence the fit ranges are slightly different. They are indicated in the figure.

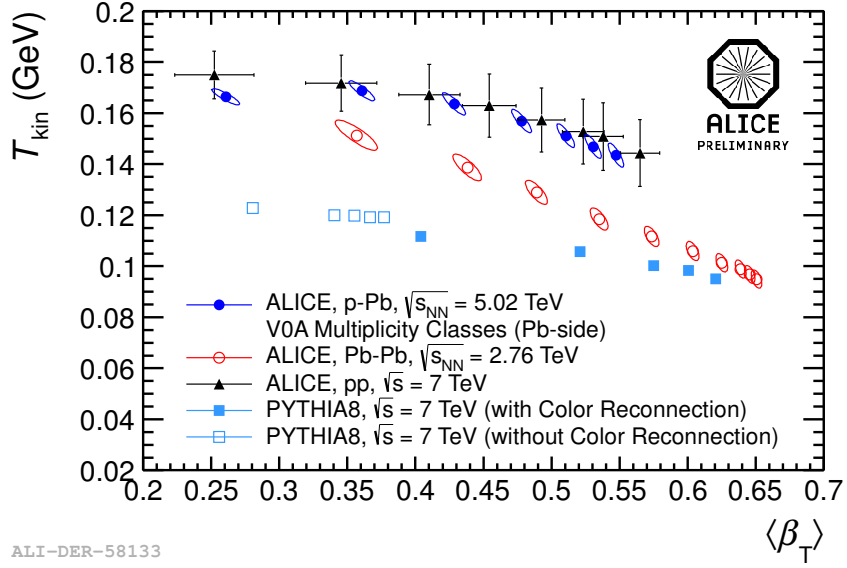


Fig. 5.18.: Blast-Wave parameter for different collision systems and PYTHIA 8. Each point represent one multiplicity class. In general, the multiplicity increases with  $\langle\beta_T\rangle$ . The trend seen in Pb-Pb collisions as a function of centrality is also observed for the parameters from the Blast-Wave fit to p-Pb and pp spectra as a function of multiplicity. The fits to the spectra generated with PHYTIA show only a similar behavior, when the color reconnection mechanism is used. Also published in [ALICE14n]

Fig. 5.18 shows the extracted parameters for p-Pb and Pb-Pb collisions. Plotted is the kinetic freeze-out temperature  $T_{\text{kin}}$  as a function of the mean transverse flow  $\langle\beta_T\rangle$  for the different multiplicity (centrality) classes. Here,  $\langle\beta_T\rangle$  is defined as

$$\langle\beta_T\rangle = \frac{2}{2+n}\beta_s. \quad (5.7)$$

For low multiplicities higher freeze-out temperatures and less radial flow is found as for high multiplicity (centrality) classes. The parameters show a similar trend for p-Pb as for Pb-Pb, which is consistent with radial flow in p-Pb collisions within the limitations of the Blast-Wave model. When comparing the parameters as a function of charged particle multiplicity  $\langle dN_{\text{ch}}/d\eta \rangle$  a higher mean radial flow  $\langle\beta_T\rangle$  can be observed for p-Pb collisions with respect to Pb-Pb collisions at the same multiplicity, whereas the freeze-out temperatures are compatible within systematic

uncertainties. The higher radial flow values in p-Pb collisions could find its natural explanation in higher pressure gradients, due to the smaller system size, as suggested in [SZ13].

As already discussed in Section 2.3.1, the elliptic flow coefficient  $v_2$  for p-Pb collisions shows a characteristic mass ordering for  $\pi$ , K, and p [ALICE13d]. This is consistent with the expectation of the hydrodynamic picture and can be tested by a combined Blast-Wave fit of the particle spectra and the flow coefficients with the extension of the Blast-Wave model introduced in [HKH<sup>+</sup>01]. The fit results differ by about 2% with respect to the previous fit and describes the  $v_2$  of pions, kaons and protons relatively well, although the fit quality is slightly worse compared to similar fits in Pb-Pb collisions [ALICE14h].

The Blast-Wave model has also been used to fit the pion, kaon and proton spectra from  $\sqrt{s_{NN}} = 7$  TeV pp collisions as a function of multiplicity and the resulting fit parameters are also plotted in Fig. 5.18. Remarkably, they seem to follow the same trend as for p-Pb and Pb-Pb collisions.

To test this picture further, pion, kaon and proton spectra generated with PHYTIA 8 [SMS08] pp collisions at  $\sqrt{s_{NN}} = 7$  TeV have also been divided in multiplicity classes at mid-rapidity  $|\eta_{LAB}| < 0.3$  (0-4, 4-9, 10-14, 15-19 and  $>19$ ) and fitted with the Blast-Wave model. This has been done with (closed symbols) and without (open symbols) the color reconnection mechanism (CR) [SW07, SS11]. CR is a mechanism, where strings from independent parton interactions can fuse before hadronization. This final state effect results in a collective particle production from the fragmentation of these boosted strings within the PYTHIA hadronization model. It is needed in PHYTIA 8 to describe the  $\langle p_T \rangle$  of all charged particles as a function of multiplicity in pp collisions at the LHC [ALICE13g]. The trend of the extracted Blast-Wave parameters is much closer to the one seen for data of pp, p-Pb and Pb-Pb collisions when CR is switched on. Since PHYTIA 8 does not include radial flow, this shows that the observed pattern can also be reproduced by other mechanisms than radial flow.

### 5.3.4. Nuclear Modification Factor of Pions, Kaons and Protons

A common way to compare the yield  $dN/dy$  of a particle in heavy-ion collisions to pp collisions and make possible effects of the QGP more visible is the nuclear

modification factor  $R_{AA}$ . This concept can also be applied to p-Pb collisions and the nuclear modification factor  $R_{pPb}$  is defined as:

$$R_{pPb}(p_T) = \frac{d^2 N^{pPb}/dydp_T}{N_{\text{coll}} d^2 N^{pp}/dydp_T} = \frac{d^2 N^{pPb}/dydp_T}{\langle T_{pPb} \rangle d^2 \sigma^{pp}/dydp_T} \quad (5.8)$$

Here  $d^2 N^{pPb,pp}/dydp_T$  is the invariant yield of the particle under consideration in p-Pb and pp collisions. The invariant yield from pp collisions is scaled with the number of binary collisions  $N_{\text{coll}}$  in p-Pb, which can be obtained from Glauber calculations (cf. Section 4.3). For the calculation of  $R_{pPb}$  it is more advantageous to use the mean nuclear overlap  $\langle T_{pPb} \rangle = \sigma_{NN}/N_{\text{coll}} = 0.0983 \pm 0.0034 \text{ mb}^{-1}$  instead of the number of binary collisions, because some uncertainties of  $\sigma_{NN} = 70 \pm 5 \text{ mb}$  and  $N_{\text{coll}} = 6.9 \pm 0.6$  cancel. To convert invariant yields to cross-sections the measured cross-sections from [ALICE13f] are used.

The nuclear modification factor is expected to be unity, if p-Pb collisions are superpositions of pp collisions, i.e. no cold nuclear or hot matter effects are present. The  $R_{pPb}$  of all charged particles has been published in [ALICE12b, ALICE14b] and is consistent with unity, but a hint of a small Cronin-peak at 2-6 GeV/c is visible. The Cronin peak is historically explained by multiple scatterings of the proton off the nucleons of the nucleus and has already been introduced in Section 2.4.

As input for  $R_{pPb}$  the pion, kaon and proton spectra from [ALICE14r] have been used. Please note that for the high  $p_T$  part ( $>2 \text{ GeV}/c$  for  $\pi$ ,  $>2.8 \text{ GeV}/c$  for K and  $>3 \text{ GeV}/c$  for p) of the spectra a different rapidity range, i.e.  $|y_{\text{cms}}| < 0.3$  instead of  $-0.5 < y_{\text{cms}} < 0$ , has been used. As already discussed above, the choice of the rapidity range has little effect on the measured spectra and a combination is reasonable. Since the spectra have been published in multiplicity bins the minimum bias spectra are calculated by summing the multiplicity classes. The correction for the trigger and vertex inefficiency, which has already been discussed in Section 5.1.1, is now applied.

In addition, a pp reference at the same collision energy, i.e.  $\sqrt{s_{NN}} = 5.02 \text{ TeV}$  is necessary. Unfortunately, spectra of pions, kaons and protons have only been measured in pp collisions at  $\sqrt{s_{NN}} = 2.76 \text{ TeV}$  and  $\sqrt{s_{NN}} = 7 \text{ TeV}$ . The low to intermediate  $p_T$  spectra are published in [ALICE14d, ALICE14g], while at high  $p_T$  preliminary data are available. These spectra have been used to interpolate to the

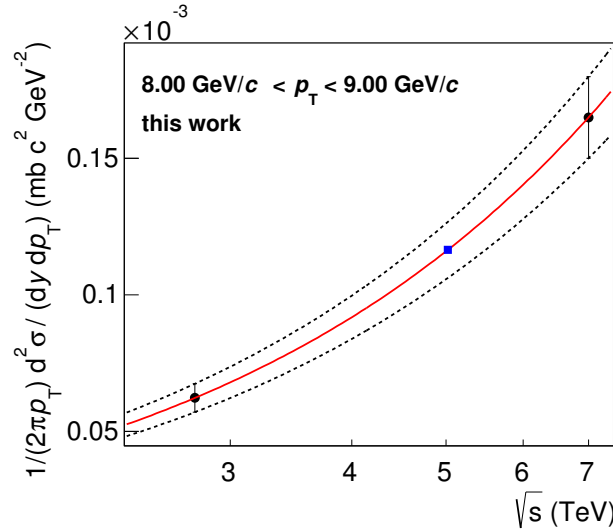


Fig. 5.19.: Exemplary fit of the proton yield with  $8 \text{ GeV}/c < p_T < 9 \text{ GeV}/c$  as a function of the collision energy to demonstrate the interpolation procedure. The power-law fit  $\sqrt{s_{NN}}^\alpha$  is performed to the central values, but also to the low and high edges of the systematic uncertainty to obtain the yield and the uncertainty at  $\sqrt{s_{NN}} = 5.02 \text{ TeV}$ .

energy of  $p$ -Pb collisions with a power-law fit for each  $p_T$ -bin. An example for this fit is shown in Fig. 5.19 for pions with  $8 \text{ GeV}/c < p_T < 9 \text{ GeV}/c$ . In addition to the central values, the low and high edges of the uncertainties have been fitted to estimate the systematic error at  $\sqrt{s_{NN}} = 5.02 \text{ TeV}$ .

The results are shown in Fig. 5.20. From the left to right and top to bottom the nuclear modification factors are shown as a function of  $p_T$  for pions, kaons and protons. As a comparison the  $R_{pPb}$  of all charged particles is shown in grey on each plot. For pions and kaons no modification is seen in the Cronin-peak region at low and intermediate  $p_T$ . For protons a significant deviation to  $R_{pPb} > 1$  is seen, which could suggest that the effect has a mass dependence. To make this effect more visible the  $R_{pPb}$  of pions and protons is compared in the bottom right panel of Fig. 5.20. The  $R_{pPb}$  of  $\Xi$  [ALICE14p], which is heavier than the proton ( $m_\Xi = 1321 \text{ MeV}/c^2$  [PDG12]), shows a higher  $R_{pPb}$  than the proton, which is consistent with the mass dependence picture. On the other hand, the results of the  $\phi$ -meson are in contradiction with a pure mass dependence, since its mass of about



### 5.3. Transverse Momentum Distributions of Pions, Kaons and Protons

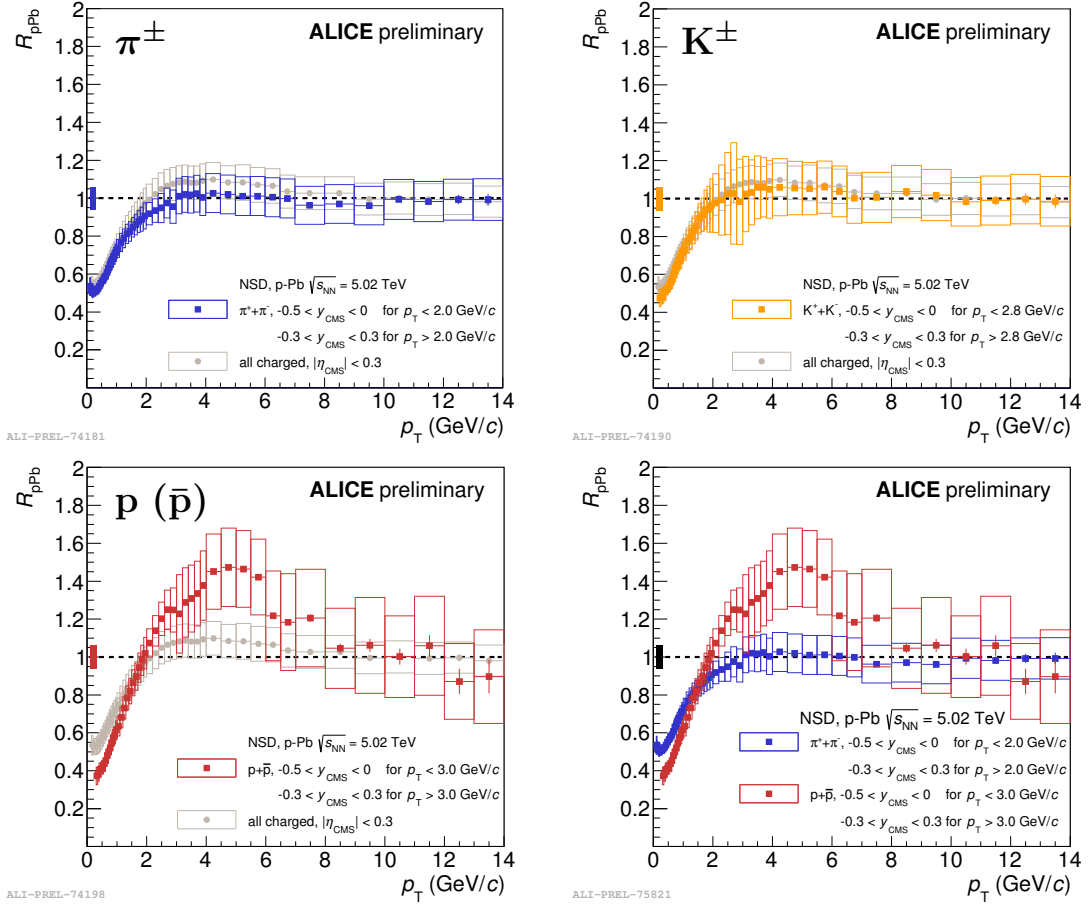


Fig. 5.20.: The nuclear modification factor of pions (top left), kaons (top right) and protons (bottom left) are shown.  $R_{pPb}$  of all charged particles [ALICE14b] is drawn as a reference in gray and exhibits a small Cronin peak, which appears to have a strong dependence on the particle type. It is not seen for pion and kaons, but very significant for protons. In the bottom right panel the nuclear modification factor of protons is compared to the one of pions. A mass dependence of the Cronin-peak is compatible with these results. The normalization uncertainty is shown as a bar on the left of each figure. Also published in [ALICE14p]

1020 MeV/ $c^2$  [PDG12] is comparable to the one of the proton, but the Cronin peak is less pronounced [ALICE14o].

A similar Cronin peak for all charged particles at intermediate  $p_T$  has also been observed at RHIC for d-Au collisions. The behavior of pions, kaons and protons in minimum bias collisions is qualitative similar to the observations in ALICE, i.e. no deviation from unity is seen for pions and kaons, but a visible Cronin peak for

protons is measured [STAR06, PHENIX13b]. It is also found that the Cronin peak is absent or only very small for the  $\phi$ -meson, similar to the LHC observation. This shows that a simple mass ordering is not sufficient to explain the data of both colliders.

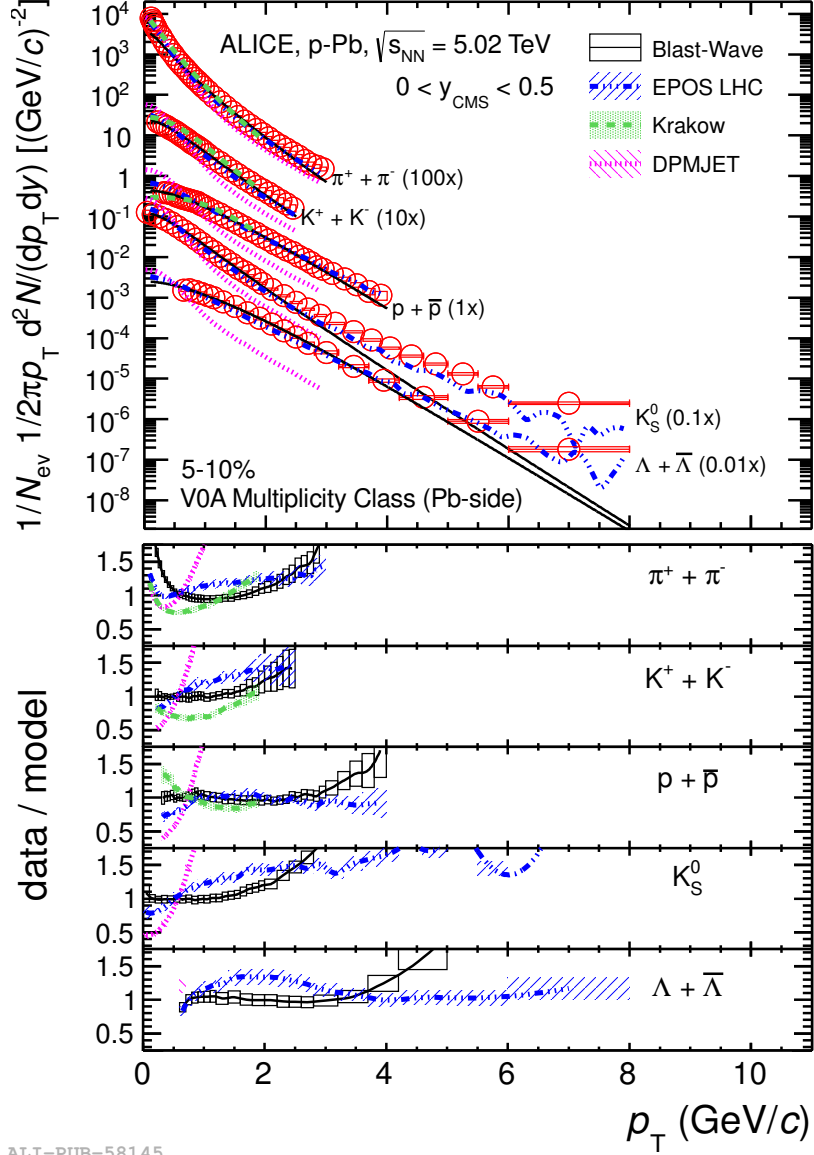
In addition to the minimum bias  $R_{\text{dAu}}$  STAR and PHENIX have also reported the  $R_{\text{dAu}}$  as a function of centrality, and state that the effect grows with centrality. By the time of writing, ALICE did not yet report this, because it is difficult to extract a meaningful centrality for  $p$ -Pb collisions. This is due to the poor correlation of multiplicity and the geometrical quantities and has already been discussed in Section 5.1.2. The measurements as a function of centrality will follow, once the biases in the centrality selection are better understood.

### 5.3.5. Comparison with Model Calculations

Several models exist that try to predict and describe the transverse momentum distributions of identified particles. In Fig. 5.21 the spectra of pions, kaons, protons and lambdas in the 5-10% multiplicity class are compared to DPMJET, the Kraków model [Boz12a], and EPOS LHC 1.99 v3400 [PKK<sup>+</sup>13].

The QCD-inspired DPMJET generator, which is based on the Gribov–Glauber approach, treats soft and hard scattering processes in an unified way (cf. Section 3.6.2). It successfully describes the charge-particle pseudorapidity density in  $p$ -Pb collisions, which was reported in [ALICE13h], but fails to describe the  $p_{\text{T}}$ -distribution of all charged particles [ALICE12b] and their  $\langle p_{\text{T}} \rangle$  [ALICE13g]. The events have been selected according to the charged-particle multiplicity in the V0A acceptance, to reproduce the experimental multiplicity selection. The identified spectra from DPMJET are softer than the measured ones for all particles. The yield is overestimated at momenta lower than 0.5 - 0.7 GeV/ $c$  depending on the particle type. Above these momenta the yield is underestimated. It could be argued though that the shapes of the DPMJET pion and kaon spectra are closer to the data at high transverse momenta, where the spectra follow rather a power-law behavior.

In the Kraków hydrodynamic model, fluctuating initial conditions are implemented based on a Glauber model using a Monte Carlo simulation. The expansion of the system is calculated event-by-event in a  $3 + 1$  dimensional viscous hydrodynamic approach and the freeze-out follows statistical hadronization in a Cooper–Frye



ALI-PUB-58145

Fig. 5.21.: Comparison of pion, kaon, proton and lambda spectra in the 5-10% multiplicity bin with several models. While DPMJET completely fails to describe the spectra, EPOS LHC and the Kraków model are successful to some extent. The Blast-Wave model has already been discussed. Please see the text for a more detailed discussion. Also published in [ALICE14h].

formalism. The measured spectra are compared to the Kraków predictions with  $10 < N_{\text{part}} < 18$ , since the  $dN_{\text{ch}}/d\eta$  from the model matches best with the measured value in the 5-10% multiplicity class. The Kraków model can reproduce the spectral shape of pions and kaons at low  $p_T$  reasonably well, but it fails for higher  $p_T$ . In terms of hydrodynamics, this could indicate the onset of a non-thermal component in the transverse momentum spectra.

In the EPOS model, founded on parton-based Gribov Regge theory, the initial hard and soft scattering creates flux tubes, which either escape the medium and hadronize as jets or contribute to the bulk matter, described in terms of hydrodynamics. As for DPMJET, the multiplicity class is defined by the multiplicity in the V0A acceptance to match it with the experimental selection. EPOS can describe the spectra of pions and protons within 20% over the full  $p_T$ -range, but is less successful for kaons and lambdas. For the lambdas a deviation of up to 40% at intermediate  $p_T$  ( $\sim 2$  GeV/ $c$ ) is evident, while the description of kaons worsens with higher  $p_T$  and the spectra are softer than the data.

As discussed before a hardening of the spectra with multiplicity and mass is observed, which is generally interpreted as radial flow in heavy-ion collisions. In fact, the Kraków model and EPOS, which incorporate final state effects are more successful in describing the data at low momenta in contrast to DPMJET, where they are missing.

## 6. Production of Deuterons and Anti-Deuterons in p–Pb Collisions

In this chapter the measurement of the transverse momentum distributions of deuterons and anti-deuterons as a function of multiplicity in p-Pb collisions at  $\sqrt{s_{\text{NN}}} = 5.02$  TeV is presented. Heavy-ion collisions but also lighter collision systems provide a suitable environment to produce light (anti-)nuclei, since a large fraction of the available energy is converted in the incident hot and dense medium into (anti-)particles. Measurements from lower energy colliders like AGS and SPS of light nuclei can be found in [NA5203, GSJ+76, B+94].

Comprehensive measurements of light (anti-)nuclei in pp and Pb-Pb collisions at LHC energies have been presented in [ALICE14f], where a qualitative difference of the deuteron over proton ratio has been found for the two collision systems. Studying the production of light nuclei in p-Pb collisions can give more insight into the production mechanisms, since it covers the gap between elementary pp collisions and heavy-ion collisions in terms of charged particle multiplicity and system size.

The results discussed in this work represent the current status of the analysis and are based on the preliminary results shown at various conferences. In particular, multiplicity uncorrelated uncertainties have been added with respect to the preliminary results.

### 6.1. Event and Track Selection

The event and track selection for deuterons follows a similar approach as for pions, kaons and protons. Since the deuterons are much less abundant a larger data sample has to be used and all runs from two run periods (ALICE internal identifiers: *LHC13b* and *LHC13c*) are used for the analysis, which corresponds to the whole minimum

## 6. Production of Deuterons and Anti-Deuterons in p-Pb Collisions

bias data sample recorded by ALICE during the 2013 p-Pb run at  $\sqrt{s_{\text{NN}}} = 5.02$  TeV. Since some runs have been flagged as bad for analysis, due to mis-calibration or non-optimal running conditions only the following runs have been considered:

LHC13b	195344	195351	195389	195391	195478	195479	195480
	195481	195482	195483				
LHC13c	195529	195531	195566	195567	195568	195592	195593
	195596	195633	195635	195644	195673	195675	195677

Table 6.1.: Data used for the deuteron analysis. The run numbers correspond to an ALICE-internal numbering scheme.

As for the  $\pi$ , K, and p analysis a minimum bias trigger (*INT7*), which requires a coinciding hit in V0A and V0C, was used for the online trigger condition and the selection has been repeated in the offline physics event selection, which also applies the quality cuts introduced in Section 5.1.1 to remove background events.

For the vertex selection a new class *AliAnalysisUtils* in *AliRoot* (available since version v5-04-53-AN) has been implemented, which selects all events with a good vertex, but also removes pile-up events. This is important, when using the whole minimum bias sample, because the running conditions are different with respect to run 195483, which was used for the  $\pi$ , K, and p analysis. In particular, the luminosity was increased during the running periods, which leads to a contribution from pile-up events. These are reduced to a negligible amount by the additional quality cuts introduced by the *AliAnalysisUtils* class. After the physics and vertex selection and the pile-up rejection about 106 million good events remain to be analyzed.

The event sample has been divided into five multiplicity classes. The multiplicity estimator used is V0A, which has also been used for the  $\pi$ , K, and p analysis. However, to account for the lower statistics the two lowest and the two highest multiplicity classes have been combined. The resulting classes and the corresponding charged particle multiplicity at mid-rapidity are summarized in Tab. 6.2.

The track selection is the same as in the  $\pi$ , K, and p analysis. It has been introduced in Section 5.1.3.

As already explained in Section 5.1.4 the LHC two-in-one magnet design causes the center-of-mass system of asymmetric collisions to move with respect to the laboratory frame, because the energy per nucleon is different for the two colliding beams.

Class	V0A range (a.u.)	$\langle dN_{\text{ch}}/d\eta \rangle _{ \eta <0.5}$
60–100%	< 52	$7.1 \pm 0.2$
40–60%	52–89	$16.1 \pm 0.4$
20–40%	89–142	$23.2 \pm 0.5$
10–20%	142–187	$30.5 \pm 0.7$
0–10%	> 187	$40.6 \pm 0.9$

Table 6.2.: Default multiplicity bins and the corresponding charged particle multiplicities at mid-rapidity. Only systematic uncertainties are shown, since statistical uncertainties are negligible

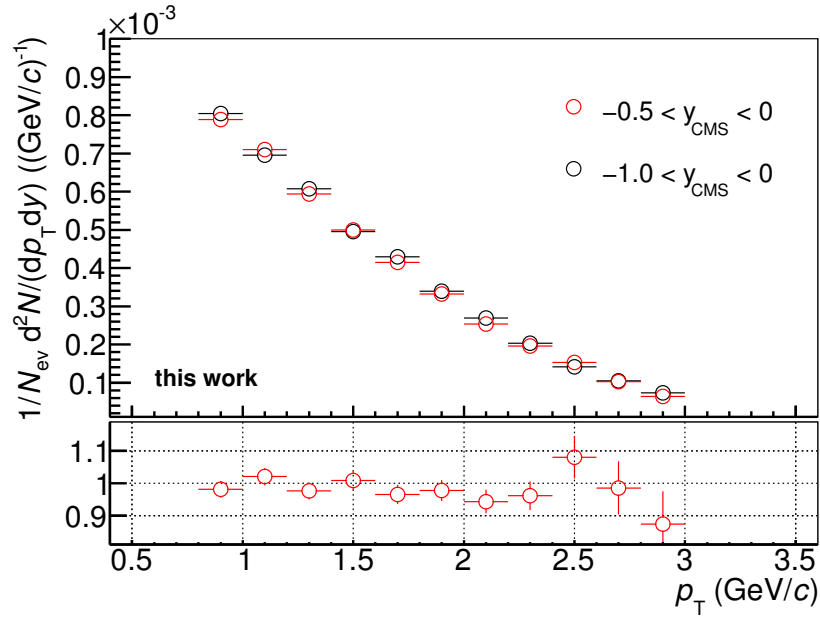


Fig. 6.1.: Deuteron spectra for two different rapidity cuts for the minimum bias event class as a function of  $p_T$ . The bottom panel shows the ratio of spectrum with the  $-0.5 < y < 0$  cut to the spectrum with the  $-1 < y < 0$  cut.

In case of p–Pb collisions the shift in rapidity is  $\Delta y = 0.465$  and an asymmetric rapidity window ( $-0.5 < y < 0$ ) was chosen for the  $\pi$ , K, and p analysis. Since deuterons are much less abundant, the range was extended to  $-1 < y < 0$ , which increases the statistics by a factor of two and has a small or no effect on the resulting spectra.

Fig. 6.1 shows the difference of the two rapidity windows for deuterons in the minimum bias class. The bottom panels show the ratios of the spectra with statistical uncertainties which are compatible with unity. This also applies for anti-deuterons.

### 6.1.1. Momentum Correction

The tracking algorithm takes Coulomb scattering and energy loss into account, but can only use a preliminary PID, which is based on the TPC  $dE/dx$  signal, for this (cf. Section 3.6.1). However, this correction is only supported for pions, kaons and protons. For all other particles the pion mass is assumed to account for the lost energy, which results in a wrongly reconstructed momentum for heavier particles like deuterons. For this reason a correction of the transverse momentum is required. The correction is calculated with Monte Carlo studies by comparing the reconstructed transverse momentum  $p_{T,\text{rec}}$  with the generated transverse momentum  $p_{T,\text{gen}}$ . The momentum correction is defined as  $p_{T,\text{rec}}/p_{T,\text{gen}}$  and fitted with the empirical formula:

$$f(p_T) = A + B \left( 1 + \frac{C}{p_T^2} \right)^D \quad (6.1)$$

where  $A$ ,  $B$ ,  $C$  and  $D$  are free parameters. The resulting fit is shown in Fig. 6.2 on the left. The correction is largest at low momenta and then quickly vanishes, which reflects the expected  $1/\beta^2$ -dependence of the energy loss. On the right of Fig. 6.2 the difference between reconstructed and generated  $p_T$  after applying the correction is shown as a function of  $p_T$ . This shows that the correction works as expected.

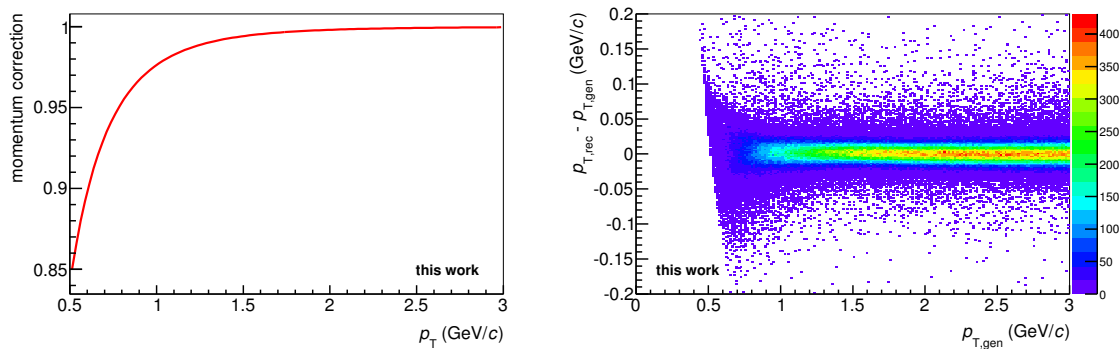


Fig. 6.2.: Transverse momentum correction for deuterons. The correction, which is the result of the fit explained in the text is shown on the left. On the right the difference of the generated and reconstructed  $p_T$  is shown as a function of  $p_{T,\text{gen}}$ , which is as expected distributed around zero.



## 6.2. Monte Carlo Simulation

Common event generators like DPMJET and HIJING do not include primary nuclei, which are heavier than protons, by default and a dedicated Monte Carlo production is required in addition to the standard simulations used for the  $\pi$ , K, and p analysis. It is needed to calculate the tracking efficiency and extract a template of primary deuterons for the secondary correction similar to the one introduced in Section 5.1.5. To include primary deuterons in the production a *cocktail* of several generators was set up. The DPMJET generator was used to generate events as for the standard p-Pb production (*LHC13b2\_efix*). The events have simulated with the running conditions of the run list above and were distributed among the runs according to the available statistics in the data. In addition, four box generators, which generate and add d,  $\bar{d}$ ,  ${}^3\text{He}$  and  ${}^3\bar{\text{He}}$  are used. For each event ten particles of each type are generated with a flat  $p_T$  distribution in  $0 < p_T < 8 \text{ GeV}/c$ , a flat rapidity distribution in  $-1 < y_{LAB} < 1$  and a flat  $\varphi$  distribution in  $0 < \varphi < 2\pi$  and are injected into the DPMJET event. The resulting production contains roughly 250.000 events and is

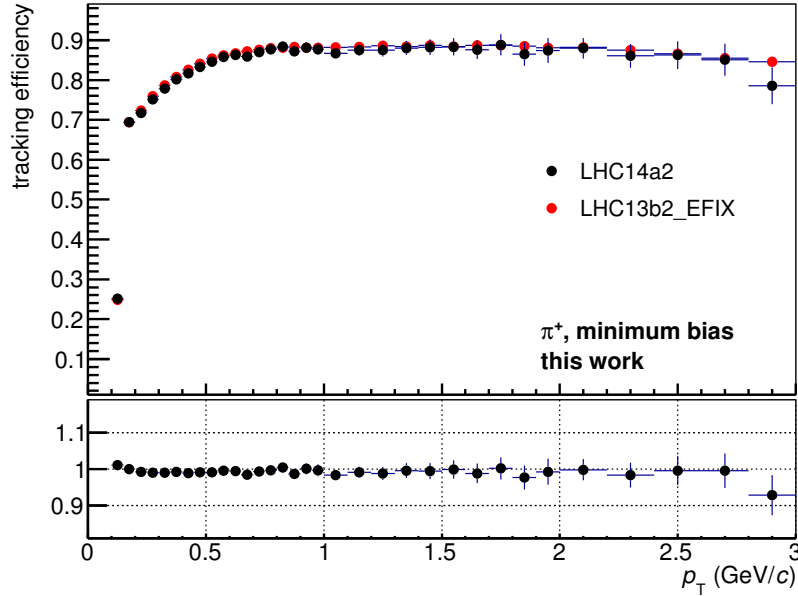


Fig. 6.3.: Comparison of tracking efficiency of pions for LHC14a2 and LHC13b2\_efix. Only statistical uncertainties are shown. The bottom panel shows the ratio, which is in agreement with unity.

labeled *LHC14a2*. To validate the production the tracking efficiency of pions, kaons and protons as a function of  $p_T$  have been compared for the enhanced and the standard DPMJET production. This is shown in Fig. 6.3 for pions. The efficiencies are in good agreement

In addition, the standard Monte Carlo is used to extract a template for secondary deuterons, because it provides much better statistics for the secondary template.

### 6.3. Particle Identification

The particle identification is similar to the one of  $\pi$ , K, and p, but some more caution has to be taken for the TOF signal, because the signal extraction suffers from a large background of mismatched tracks. Fig. 6.4 on the left shows the TPC  $dE/dx$  signal as a function of momentum again (cf. Section 3.2). The deuteron band is clearly visible and a clean track by track separation is possible to momenta as high as 1 GeV/c by applying a  $3\sigma$  cut around the expected signal from the Bethe Bloch parametrization.

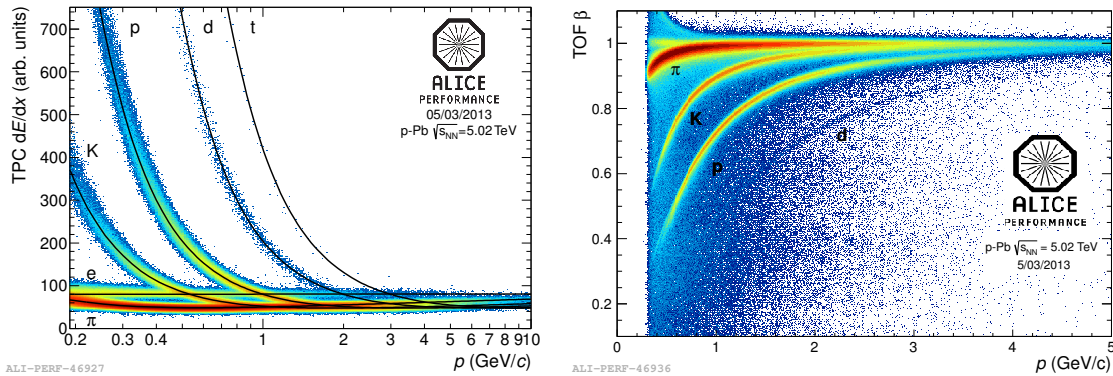


Fig. 6.4.: Performance of the TPC PID. The bands of the different particles are clearly visible. The lines indicate the expected  $dE/dx$  signal for the corresponding particle. A clean identification of deuterons is possible for transverse momenta up to 1 GeV/c. On the right the relativistic  $\beta$  measured with the TOF is shown. While the deuteron band is visible below the proton band, it lies on a large background.

Fig. 6.4 on the right shows the relativistic  $\beta$  as a function of momentum again (cf. Section 3.3). The deuteron band is visible below the proton band, but it is also evident that it lies on top of a large background, which originates from tracks that

have been matched wrongly to a TOF hit. While the pre-selection with the TPC  $3\sigma$  cut removes some of the background at low  $p_T$  a substantial amount of background at high  $p_T$  has to be subtracted.

For this reason, a statistical approach was chosen for the TOF signal. Together with the momentum the relativistic  $\beta$  gives the squared mass of the particle:

$$m_{\text{TOF}}^2 = \frac{p^2}{\gamma^2 - 1} \quad (6.2)$$

where  $\gamma = 1/\sqrt{1 - \beta^2}$  and  $p$  is the total momentum of the particle. The expected squared mass of the deuteron ( $m_d = 1.876 \text{ GeV}/c^2$  [PDG12]) is subtracted from the measured squared mass  $m_{\text{TOF}}^2$ . This way, the deuteron peak in the mass distribution is at  $0 \text{ GeV}^4/c^2$ . The resulting signal  $m_{\text{TOF}}^2 - m_d^2$  is then fitted with a Gaussian plus an exponential tail for the signal and a first order polynomial plus an exponential for the background

$$m_{\text{TOF}}^2 - m_d^2 = \begin{cases} A \cdot e^{-\frac{(x-B)^2}{2D^2}} + E + F \cdot x + G \cdot e^{H \cdot x} & x \leq A + D \\ A \cdot e^{-\frac{(x-B)^2}{2C^2}} \cdot e^{-D \frac{x-D-B}{C^2}} + E + F \cdot x + G \cdot e^{H \cdot x} & x > A + D \end{cases} \quad (6.3)$$

where A-H are free parameters. An example of a fit with this function is shown in Fig. 6.5 for deuterons with  $2.4 < p_T < 2.6 \text{ GeV}/c$  in the 0-10% multiplicity class.

While the fit works very well up to  $3 \text{ GeV}/c$ , the particle identification method is also the limiting factor for higher  $p_T$ , because the signal to background ratio worsens drastically and the statistical uncertainties of the individual  $m_{\text{TOF}}^2$ -bins result in an unstable fit.

## 6.4. Corrections

The raw signal, which has been extracted with the particle identification method has to be corrected for several effects. The hadronic cross-section of anti-nuclei is not very well constrained and a correction for the absorption will be discussed. In addition, the raw spectra have to be corrected for the tracking and TOF matching efficiency and in case of the deuterons the contribution from secondary particles has to be subtracted.

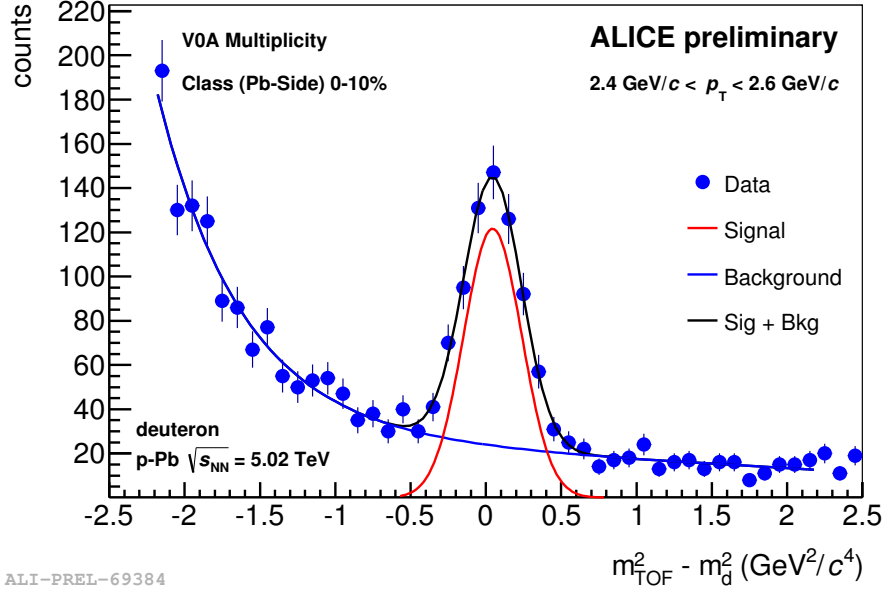


Fig. 6.5.: Fit to the squared mass measured with TOF, where the squared deuteron mass has been subtracted. The blue points are the data with statistical uncertainties, the blue line is the background and the red line is the extracted signal. The fit result is shown in black.

#### 6.4.1. Absorption Correction

Naturally, the absorption cross-section of deuterons is comparably small and is negligible. A good description of the particle traversing through the detector can be accomplished with the standard transport models. For anti-deuterons the knowledge of the cross-section is very limited and the only data, which is available, was published by the U-70 Serpukhov accelerator [DDG<sup>+</sup>71] and is limited to high momenta (13.3 GeV/c). This gives only weak constraints on the cross-section at low momenta, where it is expected to be most relevant.

Two different approaches that try to extrapolate the available data down to low momenta, are described in [ALICE14f] and are summarized here. One way is to use the measured cross-sections of anti-protons  $\sigma_{\bar{p},A}$  and anti-neutrons  $\sigma_{\bar{n},A}$  on nuclei and an empirical formula to combine them:

$$\sigma_{\bar{d},A} = \left( \sigma_{\bar{p},A}^{3/2} + \sigma_{\bar{n},A}^{3/2} \right)^{2/3} \cdot K(A), \quad (6.4)$$

where  $A$  is the mass number of the target material and  $K(A)$  a scaling factor, which is obtained by using the same procedure on measured proton and nuclei cross-sections. This optical model is implemented in GEANT 3, i.e. used for the Monte Carlo production described above. A more sophisticated approach has been chosen for the GEANT 4 transport model. Here, Glauber calculations are used together with the well measured total and elastic  $p\bar{p}$  cross-sections [UAG<sup>+</sup>11]. This approach has already proven successful for the calculation of anti-deuteron on deuteron interactions at  $p_{\bar{d}} = 12.2$  GeV/c [UAG<sup>+</sup>11, and references therein].

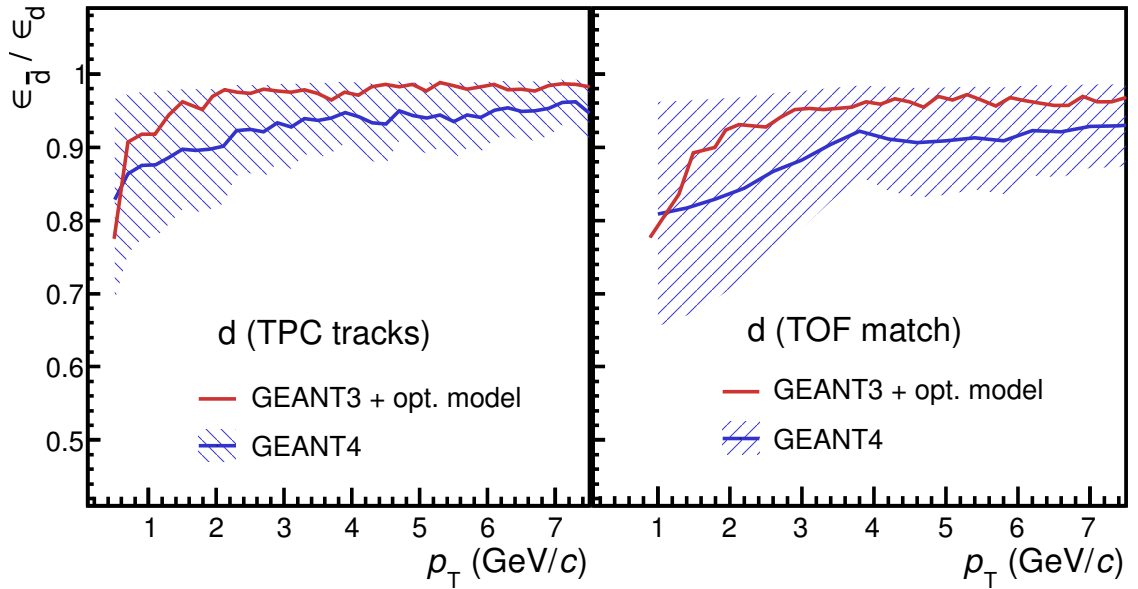


Fig. 6.6.: Absorption correction for tracking and for tracking + TOF matching combined for Geant 3 including the optical model and Geant 4. Figure from [ALICE14f]

In Fig. 6.6 these two approaches are compared. Shown is the anti-deuteron tracking efficiency normalized to the deuteron tracking efficiency for Geant 4 and Geant 3 including the optical model. The same is shown on the right for tracks with a TOF matching requirement. The absorption in Geant 4 is systematically higher than in Geant 3 + optical model. The difference between the two approaches underlines that the knowledge in this momentum region is very poor. As the default correction in this

work the Geant 4 approach was chosen, since it uses the more sophisticated model. The area shaded in blue indicates the systematic error assigned to the correction, which takes the difference with respect to the Geant 3 + optical model approach into account. Please note that the anti-deuteron over deuteron ratio is flat over the whole  $p_T$ -range and compatible with unity (cf. Section 6.6.1), when using the Geant 4 absorption correction.

### 6.4.2. Tracking and Matching Efficiency

The global tracking efficiency and TOF matching efficiency as a function of  $p_T$  of deuterons have been calculated as described for the pion, kaon and proton analysis in Section 5.1.5. The Monte Carlo simulation used to extract the efficiency is *LHC14a2*, which has been set up for this measurement and was described in Section 6.2. To obtain the efficiencies for anti-deuterons, the deuteron efficiency has been scaled with the absorption correction from GEANT 4 introduced in the previous section.

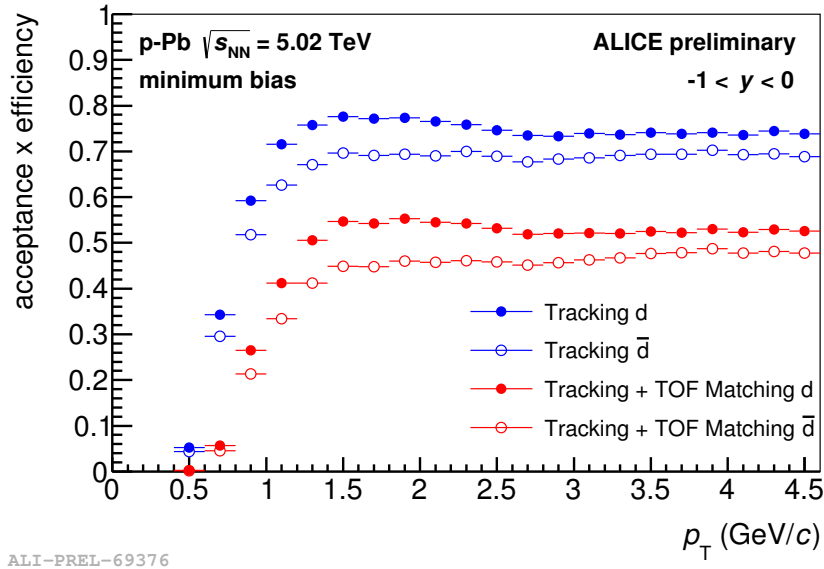


Fig. 6.7.: The tracking (blue) and tracking including TOF matching combined (red) for deuterons (closed symbols) and anti-deuterons (open symbols). The effect of anti-deuteron absorption is clearly visible for the efficiency with respect to the deuteron efficiency.

Since the tracking and TOF matching efficiencies are not multiplicity dependent, the minimum bias efficiencies have been used for all multiplicity classes. They are shown in Fig. 6.7. Here, the effect of the absorption is clearly visible for anti-deuterons with respect to deuterons. In addition, particle and anti-particle efficiencies approach each other at higher  $p_T$ , which is expected, since the absorption cross-section decreases for higher momenta.

The efficiency is the limiting factor for the reach to low  $p_T$  of the transverse momentum distributions of deuterons and anti-deuterons. The average tracking efficiency for 600-800 MeV/ $c$  is roughly 35% for deuterons and is sufficiently high. However, the bin covers efficiencies between 20-50% and one has to be extremely careful to extract a meaningful efficiency, because small differences in the shape and in particular in the rise of the tracking efficiency in data and Monte Carlo can result in large differences in the spectra. In addition, the correction for secondary deuterons, which will be discussed in Section 6.4.3, is quite large ( $> 70\%$ ). For these reasons it was decided to drop this bin and limit the  $p_T$  reach to 800 MeV/ $c$  for this work.

### 6.4.3. Secondary Correction

High momentum particles produced in p-Pb collisions at  $\sqrt{s_{NN}} = 5.02$  TeV interact with the detector material and can knock out secondary deuterons. Since the measurement of deuterons aims at understanding the hadro-chemistry and production mechanism of light nuclei in p-Pb collisions, this contribution has to be subtracted from the raw yield obtained with the particle identification method introduced above.

To calculate the secondary contribution the same data-driven approach as for pions and protons is used. The  $DCA_{xy}$  distribution is fitted with a primary and secondary deuteron template, which are extracted from Monte Carlo for each  $p_T$ -bin. This fit is possible, because primary deuterons originate from the primary vertex, whereas secondary deuterons have a flat  $DCA_{xy}$  distribution, because they originate from interaction of particles with the detector material.

Exemplary the fit is shown in Fig. 6.8 for deuterons with  $0.8 \text{ GeV}/c < p_T < 1 \text{ GeV}/c$  for the minimum bias event sample. Please note that the range used for the fit is  $\pm 0.5$  cm, but the secondary contribution is calculated in the narrower range  $\pm 0.25$  cm. This has the advantage that the size of the correction can be reduced,

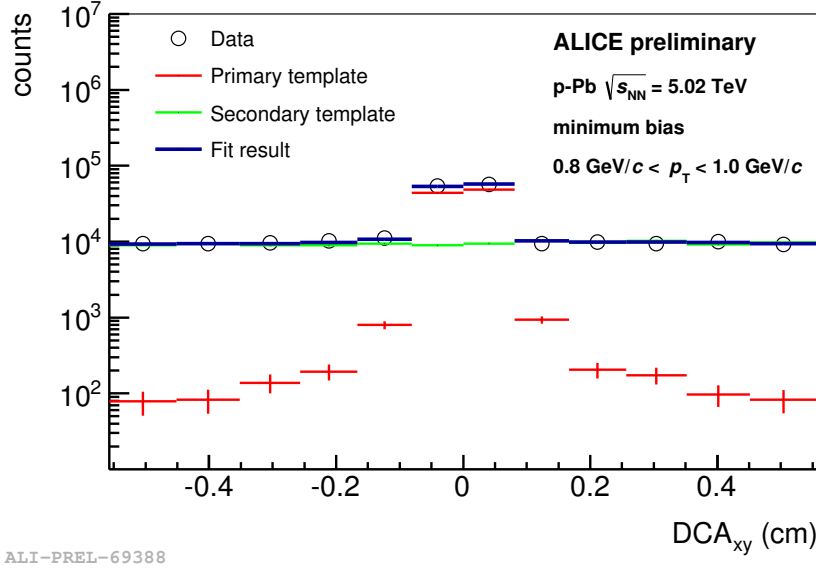


Fig. 6.8.: Fit of the  $DCA_{xy}$  distribution (open circles) with a primary (red markers) and secondary (green markers) template. The fit result is shown in blue. This fit has been performed for all  $p_T$ -bins to subtract the contribution of secondary deuterons from the raw yield.

but at the same time the secondary template can be fitted to the shoulders at  $|DCA_{xy}| > 0.25$  cm.

The secondary correction does not show any multiplicity dependence, which can be seen in Fig. 6.9 on the left. Here, the correction for the 0-10% and the 60-100% multiplicity classes is shown. In the bottom panel the difference of both multiplicity bins is shown. While there are some deviations, a trend or offset in the difference is not visible. The deviations appear to be of statistical origin, but a systematic error, which will be evaluated in Section 6.5, is also assigned. However, a lack of statistics and a resulting unstable fit can be observed for the 60-100% multiplicity class at high  $p_T$ . For this reason the minimum bias correction is used for all multiplicity classes. It is shown in Fig. 6.9 on the right.



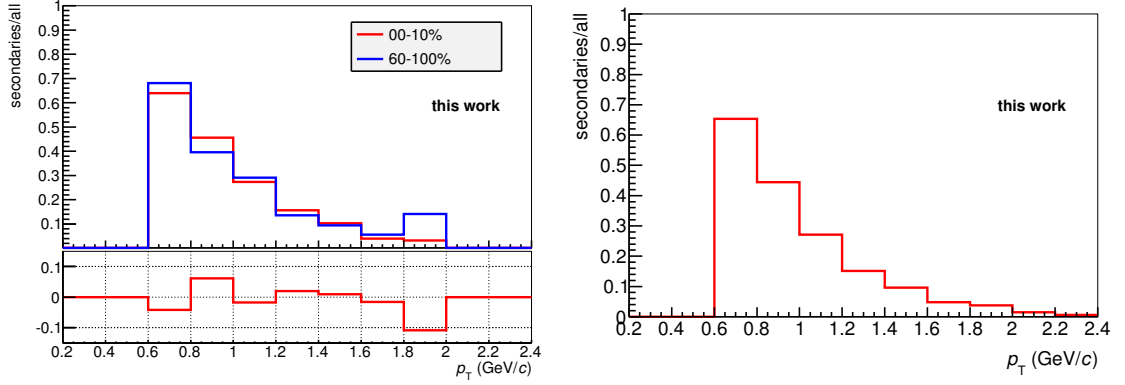


Fig. 6.9.: Secondary correction for deuterons as function of  $p_T$  for a high and low multiplicity class on the left. The bottom panel shows the difference between the two classes, which is compatible with zero. On the right the correction calculated with the minimum bias event sample is shown. It is used for all multiplicity classes.

## 6.5. Systematic Uncertainties

Several sources of systematic uncertainties have been considered. While most uncertainties, like on material budget, TOF matching, absorption correction, and tracking efficiency can be taken from other analysis, the uncertainties on the particle identification and secondary subtraction have to be evaluated for this analysis. The total systematic uncertainty is calculated by adding the individual sources quadratically. The individual sources and the resulting uncertainty is shown in Fig. 6.10 for deuterons and in Fig. 6.11 for anti-deuterons as a function of  $p_T$ . The individual sources are discussed in the following paragraphs.

**Particle identification** To estimate the error on the particle identification the TPC PID and the TOF PID have been tested individually. For the TPC PID the  $n\sigma$  cut has been varied to  $\pm 2$  and  $\pm 4$ . For the TOF PID, the bin counting method was used, i.e. the bin content in the signal region was integrated, after subtraction of the background, and compared to the signal fit. The resulting uncertainties are plotted in Fig. 6.10 and 6.11 in green. While it is small at low  $p_T$  (5%), it rises quickly for higher  $p_T$  (up to 17%), which is due to the decreasing statistics of the signal and

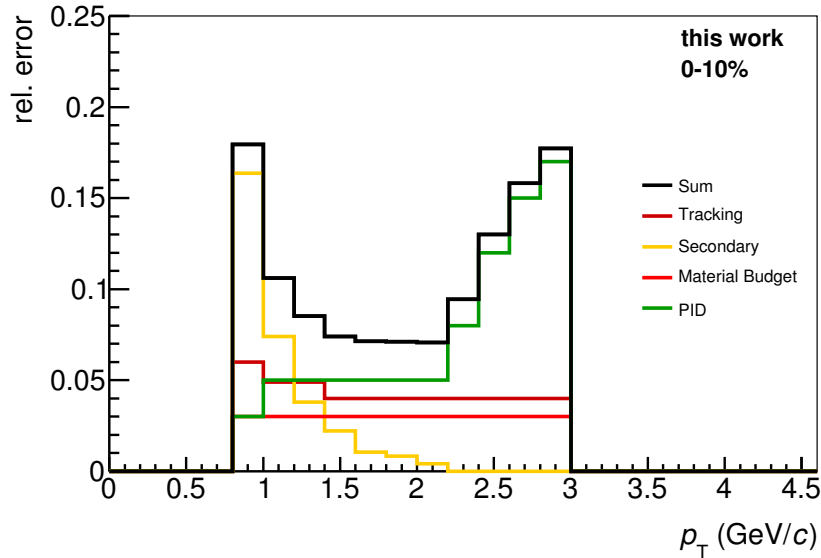


Fig. 6.10.: Systematic uncertainties of deuterons in the 0-10% multiplicity class as a function of  $p_T$ . The individual sources are shown with different colors, whereas the quadratically summed total uncertainty is shown in black. The dominating source is the secondary correction at low  $p_T$  and the particle identification at high  $p_T$ . Please note that the uncertainties are identical for all multiplicity classes, except for the particle identification, which has larger uncertainties at lower momenta for lower multiplicities.

the increasing background of mismatched tracks. For this reason the uncertainty is also multiplicity dependent and rises at lower  $p_T$  for lower multiplicities.

**Secondary correction** As already discussed, the secondary correction is large for low transverse momenta and decreases quickly with increasing momentum. The uncertainty on the correction was estimated by varying the fit range to  $\pm 2$  cm and  $\pm 0.25$  cm. The resulting uncertainty is about 20% of the total correction and is shown in yellow in Fig. 6.10. Due to the size of the correction at low  $p_T$  this uncertainty dominates the total uncertainty of deuterons. This also propagates into the uncertainty on the extrapolation to low  $p_T$  for the total yield  $dN/dy$ , because it is mainly fixed at low  $p_T$ .

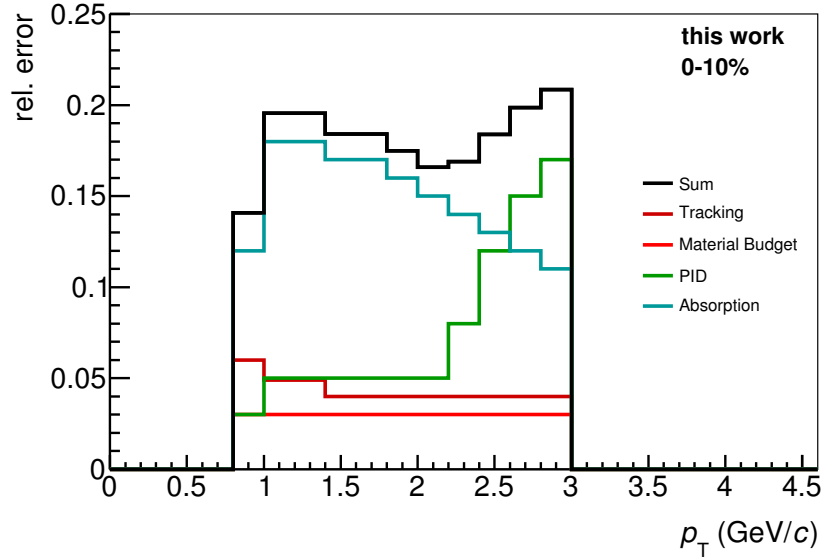


Fig. 6.11.: Systematic uncertainties of anti-deuterons in the 0-10% multiplicity class as a function of  $p_T$ . The individual sources are shown with different colors, whereas the quadratically summed total uncertainty is shown in black. The dominating source is the absorption correction. Please note that the uncertainties are identical for all multiplicity classes, except for the particle identification, which has larger uncertainties at lower momenta for lower multiplicities.

**Absorption** The absorption correction has been described in detail in Section 6.4.1. Since the knowledge of the hadronic cross-section of anti-nuclei is very poor the uncertainty on the absorption correction is sizeable. To calculate it, the differences of Geant 3 + optical model and the Glauber-approach by Geant 4 have been taken into account and in addition the uncertainty was required to be at least 60% of the correction. The resulting uncertainty is shown in Fig. 6.6 with the blue band and in Fig. 6.11 in cyan. The uncertainty decreases with increasing momentum with the exception of the first bin. Here the uncertainty is smaller, because the TOF signal is not used. To reach the TOF detector the particles have to cross the additional material of the TRD, which naturally increases the absorption correction and hence the uncertainty on it. The uncertainty on the hadronic cross-section of deuterons is negligible.

**Tracking efficiency** The tracking efficiency is taken from the analysis of pions, kaons and protons [ALICE14h], where it was estimated to 4%. It has been obtained by varying the track cuts within reasonable limits (see Section 5.1.7) and is shown in red in Fig. 6.10 and 6.11. Please note that 0-2% have been added at low momenta to account for the momentum correction.

**Material budget** While the knowledge of the material budget of the ALICE detector is quite good, simulations with increased and decreased material budget have been performed for the measurement of  $\pi$ , K, and p production in Pb-Pb [ALICE13b, ALICE12a]. The effect on protons has been scaled with the mass for deuterons to get a good estimation, which amounts to 3% and is shown in orange in Fig. 6.10 and 6.11.

### 6.5.1. Multiplicity Uncorrelated Uncertainties

As for the  $\pi$ , K, and p analysis multiplicity uncorrelated uncertainties have been calculated to substantiate the results of multiplicity dependent measurements. They are calculated by normalizing all cut variations to the minimum bias spectra before comparing to the default cut set (cf. Section 5.1.7).

The uncertainties on the material budget and absorption are fully correlated, whereas the remaining uncertainties are partly correlated. They amount to 1% for the tracking uncertainty over the whole  $p_T$  range, 6-0% for the secondary correction and 4-10% for the particle identification from low to high  $p_T$ .

## 6.6. Transverse Momentum Distributions of (Anti-)Deuterons

The  $p_T$ -differential invariant yields of deuterons and anti-deuterons after all corrections are shown in Fig. 6.12 for the five multiplicity classes. The systematic uncertainties have been plotted as boxes, while the statistical uncertainties are shown as bars and are mostly covered by the markers. In addition, the multiplicity uncorrelated uncertainties are drawn as shaded boxes.

The accessible  $p_T$  range has already been discussed in the relevant Sections 6.4.2 and 6.3. The limiting factor at low  $p_T$  is the tracking inefficiency and the secondary correction. At high  $p_T$  it is the particle identification with the fit to the TOF signal that limits the  $p_T$ -reach.

To extrapolate to high and low  $p_T$  to calculate the integrated yield  $dN/dy$  individual Blast-Wave fits (cf. Section 5.3.3) have been used, which are shown as black lines in Fig. 6.12. While several functions (Boltzmann,  $m_T$ -exponential,  $p_T$ -exponential, Tsallis-Levy, Fermi-Dirac and Bose-Einstein) have been tested, the Blast-Wave fit gives the best agreement with the data. The other functions have been used to calculate the systematic uncertainty of the extrapolation. In addition, an uncertainty obtained by shifting the data points to the low and high edge of the systematic uncertainties has been added. The statistical and multiplicity uncorrelated uncertainties have been calculated as described in Section 5.3 for pions, kaons and protons.

<b>Deuterons</b>				
Multiplicity	$dN/dy$ ( $10^{-3}$ )	statistical ( $10^{-3}$ )	systematic ( $10^{-3}$ )	uncorrelated ( $10^{-3}$ )
0-10%	3.174	$\pm 0.051$	$\pm 0.451$	$\pm 0.142$
10-20%	2.311	$\pm 0.046$	$\pm 0.330$	$\pm 0.103$
20-40%	1.679	$\pm 0.033$	$\pm 0.244$	$\pm 0.075$
40-60%	1.057	$\pm 0.027$	$\pm 0.160$	$\pm 0.059$
60-100%	0.408	$\pm 0.011$	$\pm 0.071$	$\pm 0.024$

<b>Anti-deuterons</b>				
Multiplicity	$dN/dy$ ( $10^{-3}$ )	statistical ( $10^{-3}$ )	systematic ( $10^{-3}$ )	uncorrelated ( $10^{-3}$ )
0-10%	2.990	$\pm 0.054$	$\pm 0.414$	$\pm 0.121$
10-20%	2.172	$\pm 0.060$	$\pm 0.302$	$\pm 0.088$
20-40%	1.575	$\pm 0.044$	$\pm 0.222$	$\pm 0.063$
40-60%	1.034	$\pm 0.035$	$\pm 0.146$	$\pm 0.044$
60-100%	0.383	$\pm 0.027$	$\pm 0.027$	$\pm 0.018$

Table 6.3.: Integrated yields  $dN/dy$  of deuterons and anti-deuterons. The systematic uncertainty includes the uncertainty of the extrapolation to low and high  $p_T$ .

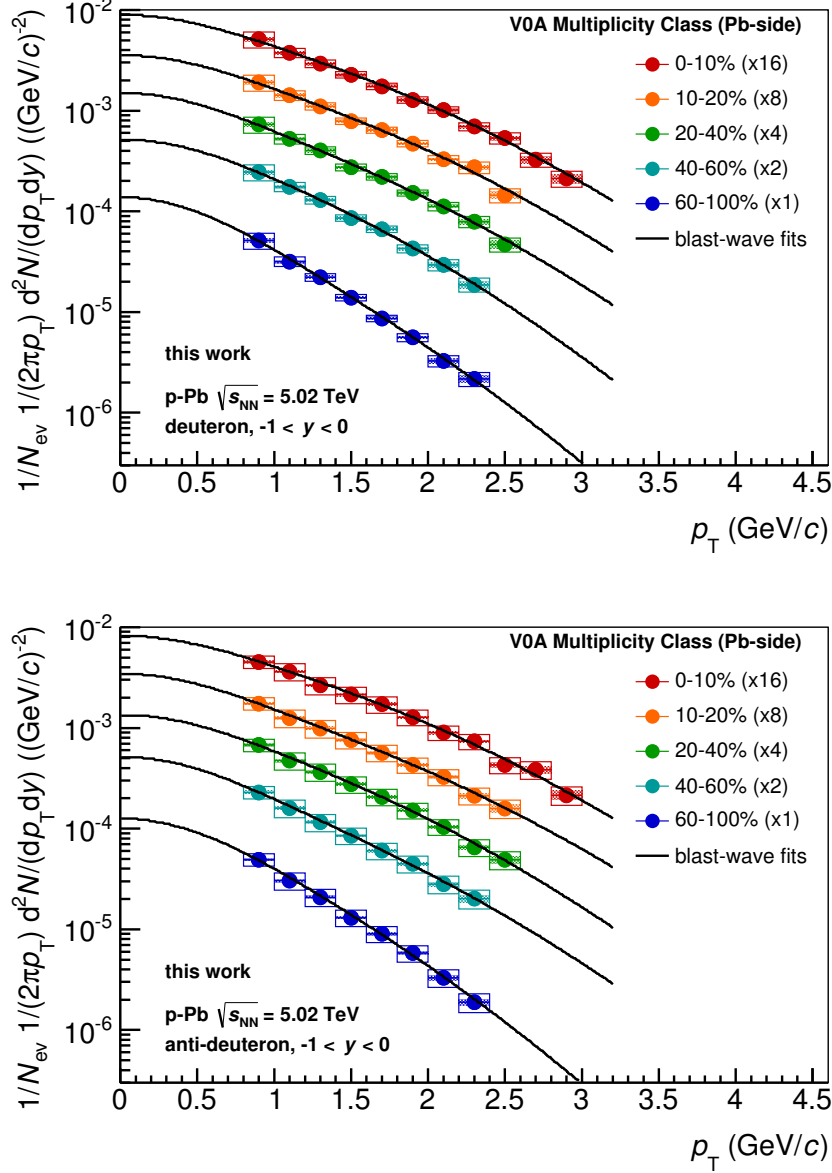


Fig. 6.12.: Deuteron (top) and anti-deuteron (bottom) transverse momentum distributions for the previously defined multiplicity classes. The spectra have been scaled with  $2^n$  to enhance the visibility. Systematic uncertainties are drawn as boxes and statistical uncertainties are mostly covered by the markers. The shaded boxes are the multiplicity uncorrelated uncertainties. The black lines indicate individual Blast-Wave fits to extrapolate to low and high  $p_T$ .

The fraction of extrapolated yield amounts to 21% for the highest and 32% for the lowest multiplicity class and the results are summarized in Table 6.3.

### 6.6.1. Anti-Deuteron to Deuteron Ratio

The deuteron over anti-deuteron ratio  $\bar{d}/d$  strongly depends on the absorption correction, which is quite sizeable, but mostly unknown in the momentum region considered in this work. With the chosen absorption correction from Geant 4, the integrated ratio is consistent with unity within the large systematic uncertainties (compare Table 6.4). However, one has to keep in mind that some of the uncertainties are correlated for deuterons and anti-deuterons.

Multiplicity	$dN/dy$	statistical	systematic
0-10%	0.944	$\pm 0.023$	$\pm 0.187$
10-20%	0.940	$\pm 0.032$	$\pm 0.187$
20-40%	0.936	$\pm 0.032$	$\pm 0.190$
40-60%	0.978	$\pm 0.042$	$\pm 0.202$
60-100%	0.941	$\pm 0.071$	$\pm 0.228$

Table 6.4.: Integrated anti-deuteron to deuteron ratio. Within the large systematic uncertainties, they are compatible with unity. Please refer to the text for more details.

Measurements of the  $\bar{d}/d$  ratio at LHC energies have not been published to this point. However, the anti-baryon to baryon ratio has been measured with high precision for pp, p-Pb and Pb-Pb by ALICE [ALICE14q]. The measured value of the anti-proton over proton ratio at midrapidity is  $\bar{p}/p = 0.980 \pm 0.014$  for p-Pb collisions. If the same value is assumed for the  $\bar{n}/n$  ratio, one can approximate the anti-deuteron over deuteron ratio to  $\bar{d}/d = (\bar{p}/p)^2 = 0.96 \pm 0.028$ . Comparing the integrated values with this expectation, a good agreement is found.

The  $\bar{d}/d$  ratio as a function of  $p_T$  is shown in Fig. 6.13 for the 0-10% and 60-100% multiplicity class. The ratio is flat, which is in agreement with the expectation for the  $\bar{d}/d$  ratio at LHC energies. The red lines in the ratio panels are the integrated results and show that the  $p_T$  bins are distributed around it, i.e. no trend with increasing momentum is observed. Please note that the full systematic uncertainties are drawn, of which some are partly correlated. However, the dominating sources of

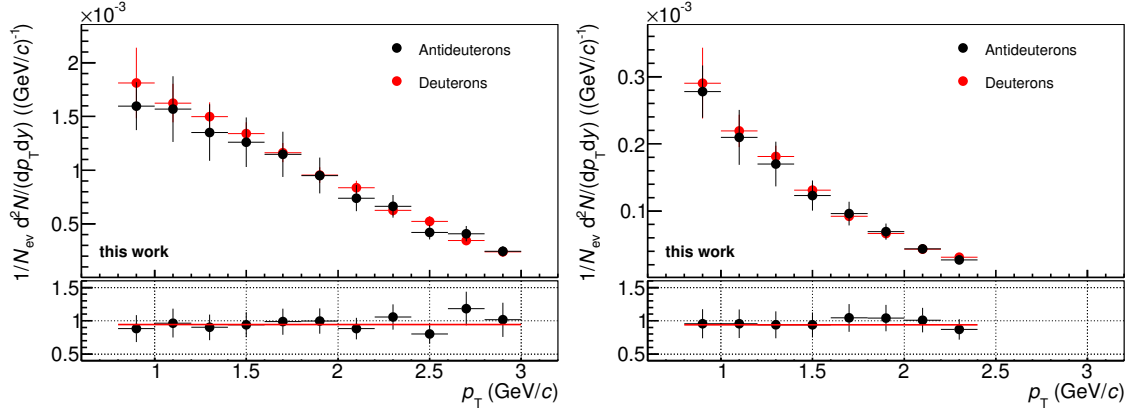


Fig. 6.13.: Anti-deuteron over deuteron spectra and the corresponding ratio for the 0-10% (left) and 60-100% (right) multiplicity class. The red lines indicate the integrated result. The  $\bar{d}/d$  ratios are flat over the  $p_T$  range and compatible with the integrated result. Shown are the full systematic uncertainties.

systematic uncertainty, i.e. secondary correction and absorption correction, are fully uncorrelated.

### 6.6.2. Mean Transverse Momentum

With the extrapolation to low and high  $p_T$  with the individual Blast-Wave fits the mean transverse momentum for each multiplicity class is calculated. To evaluate the uncertainty, the same procedure as for pions, kaons and protons is used (cf. Section 5.3). The results are shown in Fig. 6.14 together with the values from Fig. 5.15.

The mean transverse momentum of deuterons is between the  $\langle p_T \rangle$  of protons and lambdas for all multiplicity classes and the mass ordering appears to be broken for  $p$ -Pb collisions. This is not the case for Pb-Pb collisions, where the  $\langle p_T \rangle$  of deuterons is in agreement with the mass ordering [ALICE14f].

It is interesting to note that the mean  $p_T$  of deuterons in high multiplicity events reaches similar values as in peripheral Pb-Pb collisions, which could point to a multiplicity-driven effect. This is however unique for deuterons as non-composite hadrons have a larger  $\langle p_T \rangle$  with respect to Pb-Pb collisions at similar multiplicities (cf. Section 5.3.2). For a discussion of the  $\langle p_T \rangle$  results in the context of coalescence models please refer to Section 6.7.2.



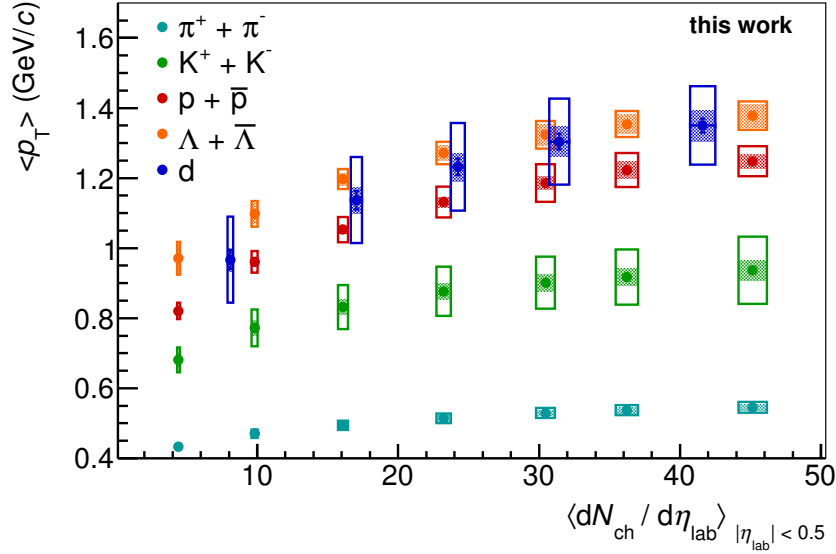


Fig. 6.14.: Mean transverse momentum of deuterons as a function of charged particle multiplicity compared to non-composite hadrons in p-Pb collisions. Please note that the charged particle multiplicities of the deuteron classes have been shifted by one to higher multiplicity to enhance the visibility. Multiplicity uncorrelated uncertainties are drawn as shaded bands.

## 6.7. Deuteron Production Models

The light nuclei abundance in heavy-ion collisions is commonly discussed within two different models: the coalescence model, where deuterons are formed by protons and neutrons, which are close in phase space [BP63, Kap80] and the thermal-statistical model, where the deuteron and all other particle abundances are fixed at the chemical freeze-out. They will be discussed in Section 6.7.2 and Section 6.7.3, respectively, after discussing the results on the deuteron to proton ratio.

### 6.7.1. Deuteron to Proton Ratio

Since the deuteron consists of a proton and a neutron, the deuteron to proton ratio  $d/p$  can shed light on the deuteron production mechanism. It has already been published for pp and Pb-Pb collisions [ALICE14f]. While the ratio is constant in Pb-Pb collisions at  $\sqrt{s_{NN}} = 2.76$  TeV as a function of centrality, it is significantly

smaller for pp collisions at  $\sqrt{s_{\text{NN}}} = 7$  TeV. Since p-Pb collisions are intermediate between these two collision systems in terms of charged particle multiplicity and system size, it is of particular interest to look at the d/p ratio as a function of multiplicity in p-Pb collisions and compare it to the other measured systems.

The ratio has been calculated with the integrated deuteron yields  $dN/dy$  shown in Table 6.3 and the proton yields from [ALICE14h]. Please note that the proton yield for the multiplicity class 0-10% (60-100%) has been calculated as the mean of 0-5% and 5-10% (60-80% and 80-100%). Because of the large absorption correction the anti-deuterons have not been considered. The protons have been published as the sum of proton and anti-proton and hence the d/p ratio corresponds to  $2d/(p+\bar{p})$

The d/p ratio is shown in Fig. 6.15 for pp, p-Pb and Pb-Pb collisions as a function of charged particle multiplicity at mid-rapidity. While the ratio is flat in Pb-Pb within the errors and significantly higher than the ratio in pp collisions, a rise is ob-

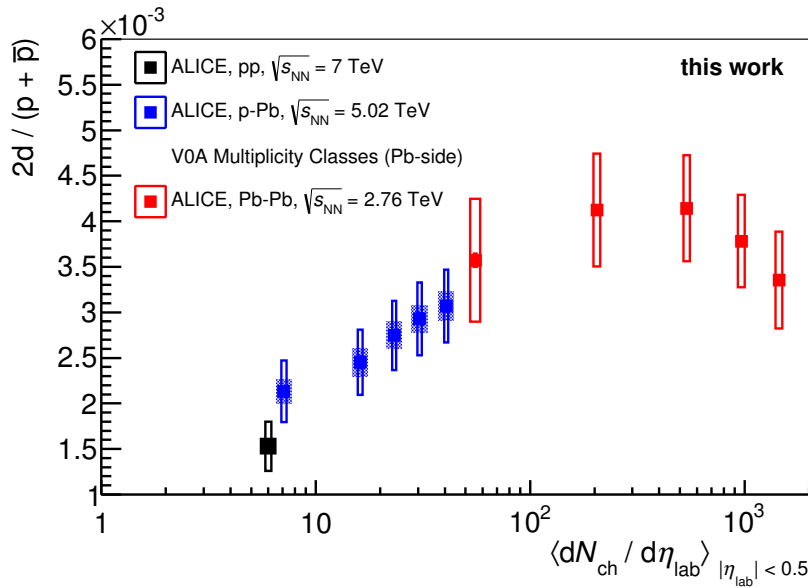


Fig. 6.15.: Deuteron over proton ratio as a function of multiplicity for pp (black), p-Pb (blue) and Pb-Pb (red) collisions. For p-Pb the multiplicity uncorrelated uncertainties are drawn as shaded boxes and underline the increase of the ratio with multiplicity. At low p-Pb multiplicity the ratio is consistent with pp collisions and at high multiplicities it is in agreement with peripheral Pb-Pb results. Please note that the uncorrelated uncertainties may not be used to compare to the other systems.

serverd for the ratio in p-Pb as function of multiplicity. In addition, low multiplicity p-Pb events are in agreement with pp collisions and high multiplicity p-Pb events are in agreement with peripheral Pb-Pb collisions. This means that the deuteron production increases stronger than the proton production with the charged particle multiplicity in p-Pb, but seems to be saturated at the multiplicities reached in Pb-Pb collisions, with respect to the proton production.

If one interprets Fig. 6.15 in terms of the two models introduced above in a qualitative way, one could argue that the increase of the d/p ratio in p-Pb is in agreement with the coalescence model, which predicts larger deuteron production rates for larger proton yields (densities). When looking at the higher multiplicities of Pb-Pb collisions a saturation of the d/p ratio is reached, which is in agreement with the thermal model freeze-out temperatures of about 156MeV/c [Flo14]. This is in itself quite surprising, when taking the low binding energy of deuterons into account. An introduction to the two models and a discussion in the context of the presented results is given in the following.

### 6.7.2. Coalescence Model

The coalescence model is a simple model in which deuterons and other light nuclei are formed by nucleons that are close in phase space [BP63, Kap80]. An increased deuteron production rate is expected for an increased proton (and neutron) production. Since neutrons are experimentally not as accessible as protons, the neutron multiplicity and transverse momentum distribution are assumed to be identical to the one of protons.

The relation between proton and deuteron transverse momentum distributions in the coalescence model is given by the coalescence parameter  $B_2$ :

$$E_d \frac{d^3 N_d}{(dp_d)^3} = B_2 \left( E_p \frac{d^3 N_p}{(dp_p)^3} \right)^2, \quad (6.5)$$

where  $p_d = 2 \cdot p_p$ . Here,  $B_2$  has been calculated for the five multiplicity classes and is shown in Fig. 6.16 as function of  $p_T$ . Please note that the 0-10% (60-100%) proton spectra have been calculated as the average of the 0-5% and 5-10% class (60-80% and 80-100%). Within the coalescence model a flat  $B_2$  as a function of  $p_T$  is expected,

## 6. Production of Deuterons and Anti-Deuterons in p-Pb Collisions

because the shape of the proton and deuteron spectra are expected to be the same at the corresponding momentum. This expectation is met for the current reach in transverse momentum and for all multiplicity classes measured in p-Pb. Please note that a deviation from the flat  $B_2$  was observed for the most central Pb-Pb collisions at high  $p_T$ , which is qualitatively explained by the position-momentum correlations caused by a radially expanding source [ALICE14f].

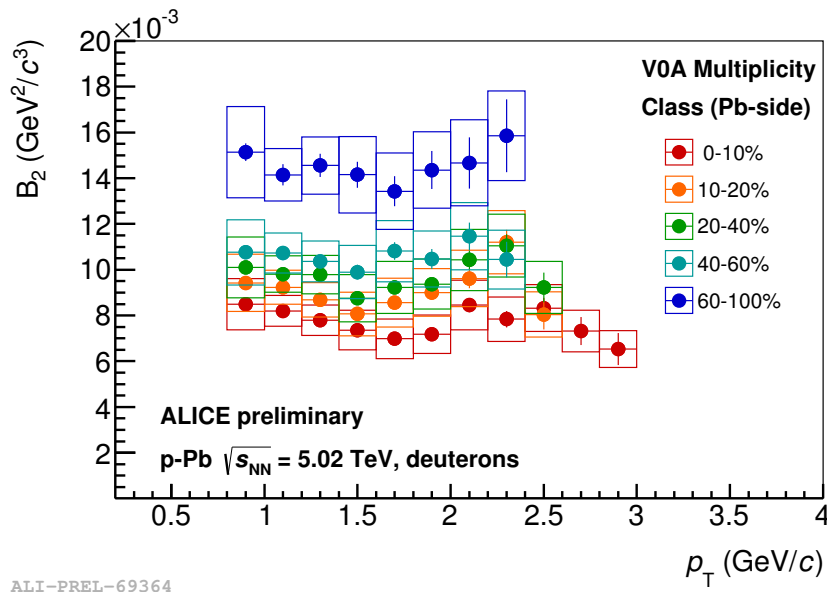


Fig. 6.16.: Coalescence parameter  $B_2$  of p-Pb collisions as a function of  $p_T$  and multiplicity. While it is constant over the whole  $p_T$  range, a decrease with multiplicity is observed. This is commonly explained with an increasing source volume.

As in Pb-Pb collisions, the  $B_2$  decreases with multiplicity. This behaviour is explained as an increase in source volume when going from low to high multiplicity events, which leads to a proton density that does not increase as fast as the proton multiplicity. In fact, the coalescence model in [SH99] predicts a  $B_2$  which is governed by the same homogeneity volume as the HBT radii and is compatible with the data in Pb-Pb collisions [ALICE14f].

At first look, the  $\langle p_T \rangle$  of deuterons, which is only slightly above the one of protons and the flat  $B_2$  may appear to be in contradiction in terms of coalescence models. In the most naive way, one could assume that the mean  $p_T$  of deuterons is twice as large as the mean  $p_T$  of protons, when  $B_2$  is flat. However, this strongly depends on

the spectral shape. In fact, if  $B_2$  is flat in  $p_T$  and the spectral shape of protons and deuterons is assumed to be exponential, the same  $\langle p_T \rangle$  is expected for both particles, because of the fundamental property of the exponential function

$$(\exp(x/a))^a = \exp(x), \quad (6.6)$$

where  $a = 2$  for deuterons. This exponential shape is a rough but reasonable approximation. The transverse momentum distributions of protons and deuterons have been fitted with a  $p_T$ -exponential form to evaluate the systematic uncertainty of the extrapolation (cf. Sections 5.3 and 6.6) and they describe the spectra within 15% in the relevant  $p_T$ -ranges of 0.4–1.5 GeV/ $c$  for protons and 0.8–3.0 GeV/ $c$  for deuterons.

The increasing trend of the d/p ratio shown in Fig. 6.15 is compatible with the coalescence model. For the low multiplicities in pp and p-Pb collisions an increasing proton density leads to an increased deuteron production. In the multiplicity region of Pb-Pb a saturation is reached. This can be explained with the increased source volume, which leads to a larger distance between produced protons and neutrons. In other words, the saturation of the d/p ratio could actually point to a saturation of the proton density, reached in the hot and dense fireball of Pb-Pb collisions.

### 6.7.3. Thermal-Statistical Model

Thermal-statistical models are very successful in describing not only the hadron production [BMRS03, ABMS06], but also the production of light nuclei for different collision systems at different energies [ABMSS11, CKK<sup>+</sup>11, ABMRS11]. They assume that the medium created in heavy-ion collisions can be described with statistical physics, when the hadro-chemistry is fixed at the chemical freeze-out, which requires that the medium is locally thermalized.

Several implementations of the thermal model have been published that follow different approaches, but for all of them the starting point is the partition function. The partition function depends on the statistical ensemble one considers, which depends on the collision system and size. For heavy-ion collisions the grand-canonical ensemble is appropriate, which ensures the conservation of the quantum numbers and

energy in a volume  $V$  on average through the temperature  $T$  and chemical potential  $\mu_i$ . The logarithm of the partition function for particle species  $i$  is given by:

$$\ln Z_i^{GC}(T, V, \mu_i) = \frac{g_i V}{\pi^2} \int_0^\infty p^2 \ln \left( 1 \pm e^{-\frac{E_i - \mu_i}{T_{ch}}} \right) dp, \quad (6.7)$$

where  $g_i$  is the spin degeneracy,  $E_i = \sqrt{p^2 + m_i^2}$  the energy and  $m_i$  is the particle mass. The plus sign is for fermions, whereas the minus sign is for bosons. The logarithm of the total partition function can be obtained by summing the logarithms of the individual partition functions of the particle species. For a hadron  $i$  with baryon number  $B_i$ , third component of the isospin  $I_{3i}$ , strangeness  $S_i$  and charmness  $C_i$ , the chemical potential is given by

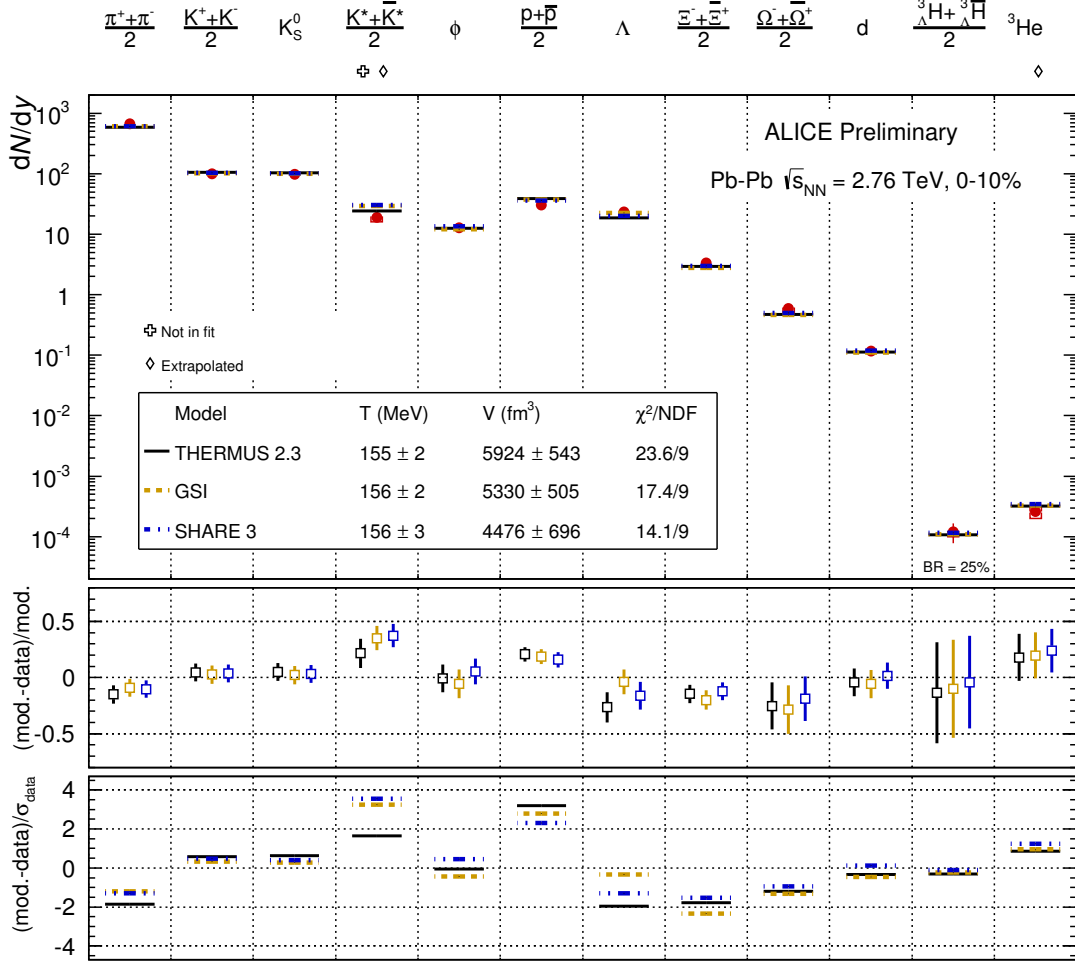
$$\mu_i = \mu_b B_i + \mu_S S_i + \mu_{I_3} I_{3i} + \mu_C C_i. \quad (6.8)$$

Here,  $\mu_S$ ,  $\mu_{I_3}$  and  $\mu_C$  are unknown, but can be calculated by conservation laws, i.e. the net strange and net charm content in the colliding nuclei is zero, which has to be conserved, since only quark anti-quark pairs can be generated. The summed isospin of the colliding nuclei amounts to  $\frac{Z-N}{2}$ . This leaves only the temperature  $T$ , the baryo-chemical potential  $\mu_B$  and the volume  $V$  as free parameters in the total partition function. Once these parameters have been obtained, the partition function can be used to calculate the thermodynamical quantities like the pressure, the entropy, the energy and in particular the particle yield

$$N_i^{GC} = T \frac{\partial \ln Z^{GC}}{\partial \mu_i}. \quad (6.9)$$

Usually, the yields  $dN/dy$  measured in heavy-ion collisions are used as input for thermal models and are fitted with an iterative procedure to obtain the remaining free parameters of the partition function. Instead of fitting particle yields, particle ratios can also be fitted, which has the advantage that the unknown parameter of the volume  $V$  cancels.

In Pb-Pb collisions a hot and dense medium is created and it seems counter-intuitive that the deuteron yield  $dN/dy$  should be fixed at the chemical freeze-out, since they should immediately dissipate at temperatures of about  $T_{ch} = 160$  MeV/c, because of their low binding energy of about 2.2 MeV/c. One idea to cope with this con-



ALI-PREL-74463

Fig. 6.17.: Thermal fit to the measured hadrons from the most central Pb-Pb collisions with SHARE 3, THERMUS 2.3 and the GSI model. Shown are the integrated particle yields  $dN/dy$  and the fit results in the top panel. The middle panel shows the relative deviation and the bottom panel the deviation as number of the measured  $\sigma_{\text{data}}$ . All models give similar results and the deuteron yield can be described with the thermal model fits. The fit quality is reasonable for all models, but better for the GSI model and SHARE 3. The fit quality can be further improved, when excluding protons. Please note that  $K^*$  has not been included in the fit and the  ${}^3\text{He}$  yield has been extrapolated to 0-10% centrality. Figure from [Flo14].

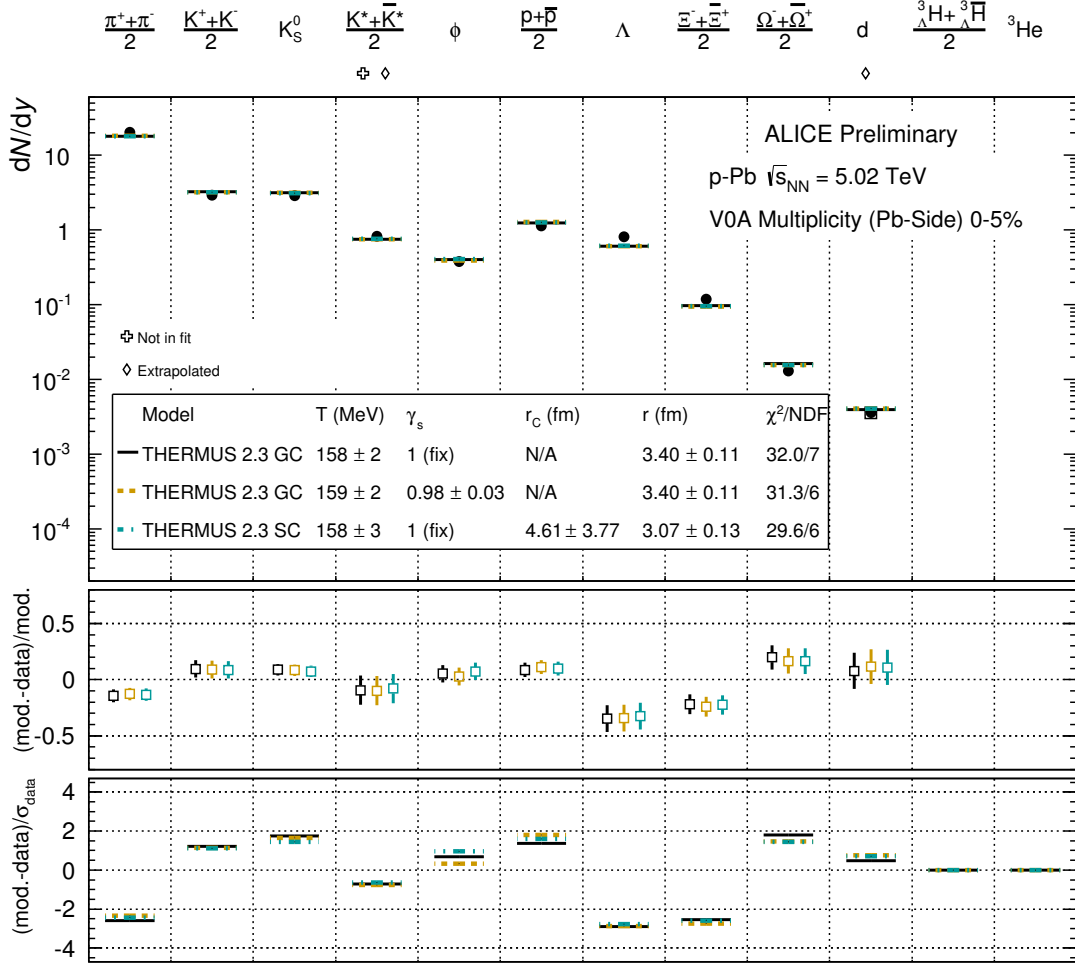
tradition, is that the nuclei formed in the hot medium, are broken up, but are regenerated (by coalescence) after the kinetic freeze-out.

However, thermal-statistical models are very successful in describing the available data on deuterons and even heavier nuclei. Fig. 6.17 shows a recent fit with three thermal models to the integrated yields  $dN/dy$  of all measured particles from the most central Pb-Pb collisions. Shown are the THERMUS 2.3 [WCH09], GSI [ABMS09] and SHARE 3 [PLRT14] model, which give compatible results and a chemical freeze-out temperature of about 155 MeV/ $c$ . The fit quality is reasonable for all models, but better for the GSI model and SHARE 3. The fits also include deuterons, which are in good agreement with the fits. Please note that the protons are off by about 20% ( $2-3\sigma$ ), which naturally results in a poor description of the  $d/p$  ratio, despite the good fit to the deuterons. When excluding the protons from the fit, the fit quality improves to  $\chi^2/\text{NDF} < 1$  for the GSI model [Flo14]. Please note that thermal models do not take into account that hadrons have different inelastic cross-sections. However, this could result in a sequential freeze-out of the different particle species at different temperatures.

Within [Flo14] the measured particles from high multiplicity  $p$ -Pb collisions have also been fitted with the THERMUS 2.3 model. The fit results are shown in Fig. 6.18 for three different configurations of THERMUS. The fit quality is poor when using the grand-canonical ensemble, because the  $p$ -Pb system is not expected to be described by it. The mixed-canonical (strangeness-canonical) ensemble, which treats the baryon and charge content grand-canonically and strangeness canonically, has also been tested, but the improvement of the fit quality is marginal and still poor. THERMUS also offers to include an additional free parameter  $\gamma_S$ , which accounts for incomplete strangeness equilibration [WC09]. It has been fixed to unity, i.e. complete strangeness equilibration, in the fits presented so far, but was allowed to vary for one of the fit configurations for  $p$ -Pb data. Anyway, it does not show any significant improvement of the fit quality and the fitted  $\gamma_S$  is compatible with unity.

In conclusion, thermal-statistical models are very successful in describing the hadron and nuclei production in Pb-Pb collisions. They are less successful in describing the data from high multiplicity  $p$ -Pb collisions and cannot explain the increasing  $d/p$  ratio with multiplicity.





ALI-PREL-74510

Fig. 6.18.: Thermal fit to the measured hadrons from high multiplicity p-Pb collisions with three different configurations of THERMUS 2.3. For the first two the grand-canonical ensemble and for the third one the mixed-canonical ensemble have been chosen. In the second configuration,  $\gamma_s$  was used as a free parameter, which can account for incomplete strangeness equilibration. However, the fit quality is not good for all three configurations. The use of a thermal-statistical model for smaller system sizes like p-Pb is questionable. Please note that  $K^*$  has not been included in the fit and the d yield has been extrapolated to the 0-5% multiplicity class. Figure from [Flo14].



## 7. Summary

In this thesis the particle production at low to intermediate transverse momenta in p-Pb collisions at  $\sqrt{s_{\text{NN}}} = 5.02$  TeV has been studied. These collisions provide a baseline for heavy-ion collisions, where a hot and dense medium is created. Proton-nucleus collisions are a unique tool to disentangle the effects of this hot medium from cold nuclear matter effects. In particular, the transverse momentum distributions as a function of charged particle multiplicity of pions, kaons, protons and deuterons have been studied within this thesis.

An enhancement of the particle production at low to intermediate transverse momenta is one of the introduced cold nuclear matter effects and has been observed in the nuclear modification factor of all charged particles in p-Pb collisions at the LHC [ALICE14b]. This Cronin effect is not visible for pions and kaons, but is pronounced for protons and  $\Xi$ s, which suggests a mass-dependent effect. However, the magnitude of the enhancement is smaller for the  $\phi$ -meson than for the proton and a pure mass dependence cannot explain the data from the LHC and RHIC. On the other hand, the missing suppression at high transverse momentum confirms that the suppression by more than a factor of two, seen in heavy-ion collisions, is a final state effect.

Previous results from ALICE suggest that the particle production in high multiplicity p-Pb collisions is subject to collective final-state effects [ALICE13e, ALICE13d]. With the measurement of the transverse momentum distributions of pions, kaons and protons several observations have been made that are reminiscent of the identified particle production in heavy-ion collisions, where they are commonly attributed to radial flow induced by a hydrodynamically expanding fireball.

The possible hydrodynamic behavior of p-Pb collisions was investigated by applying the Blast-Wave model to the measured data. While this model is very simple and has clear limitations, a trend was observed which is comparable to the results of Pb-Pb collisions. In addition, more sophisticated models like EPOS LHC and the Kraków

model, which incorporate final state effects, are more successful in describing the data, than DPMJET, which does not include final state effects.

The baryon to meson ratio  $p/\pi$  ( $\Lambda/\pi$ ) shows that the proton ( $\Lambda$ ) production is enhanced at intermediate transverse momenta and depleted at low transverse momenta in high multiplicity collisions with respect to low multiplicity collisions. The same observation has previously been made for heavy-ion collisions and is commonly interpreted as a momentum push induced by radial flow.

In addition, an increasing mean transverse momentum of the spectra with the particle mass and event multiplicity has been observed. This is typical for a collectively expanding medium and has also been measured in heavy-ion collisions. This mass ordering is broken by the  $\langle p_T \rangle$  of deuterons in p-Pb collisions. However, deuterons are only weakly bound and their production might not be subject to the same effect that drives the non-composite hadron production.

In fact, the deuteron to proton ratio as a function of charged particle multiplicity suggests that deuterons could be produced by coalescence of protons and neutrons that are close in phase-space. The saturation of the deuteron to proton ratio in Pb-Pb collisions suggests that the deuteron production is rather driven by the nucleon density than the nucleon multiplicity. While thermal-statistical models are very successful in describing not only the hadron, but also the light nuclei production in heavy-ion collisions, the fit quality for high multiplicity p-Pb data is poor.

To summarize, this thesis has contributed to the understanding of the particle production in proton-nucleus collisions and a good baseline for heavy-ion collisions is provided. Still, some features have been observed that support the hypothesis of collective final-state effects in high multiplicity p-Pb collisions. In this context, the interpretation of heavy-ion collision results might have to be handled with more caution. On the other hand, it may not be excluded that the energy density reached in high multiplicity p-Pb collisions is sufficient to create a small droplet of a QGP. In any case, the results demonstrate that proton-nucleus collisions are not a mere control experiment, but have a large discovery potential themselves.

# Zusammenfassung

In dieser Arbeit wurde die Teilchenproduktion bei niedrigen bis mittleren Transversalimpulsen in p-Pb Kollisionen bei  $\sqrt{s_{\text{NN}}} = 5.02$  TeV studiert. Diese Kollisionen sind eine Referenz für Schwerionenkollisionen, bei denen ein heißes und dichtes Medium erzeugt wird. Proton-Nukleus Kollisionen sind ein einzigartiges Werkzeug, um die Effekte von diesem heißen Medium von den kalten nuklearen Effekten zu trennen. In dieser Arbeit wurden insbesondere die Transversalimpuls-Verteilungen von Pionen, Kaonen, Protonen und Deuteronen als Funktion der geladenen Teilchendichte untersucht.

Eine verstärkte Teilchenproduktion bei niedrigen bis mittleren Transversalimpulsen ist einer der üblichen kalten nuklearen Effekte und wurde bei der Messung des nuklearen Modifikationsfaktors von allen geladenen Teilchen in p-Pb Kollisionen am LHC gemessen [ALICE14b]. Dieser Cronin-Effekt ist nicht sichtbar für Pionen und Kaonen, ist aber ausgeprägt für Protonen und  $\Xi$ s, was einen massenabhängigen Effekt nahelegt. Das Ausmaß der verstärkten Teilchenproduktion ist allerdings, verglichen mit Protonen, kleiner für  $\phi$ -Mesonen und eine reine Massenabhängigkeit kann die Daten vom LHC und RHIC nicht erklären. Auf der anderen Seite bestätigt die fehlende Unterdrückung bei hohen Transversalimpulsen, dass die Unterdrückung von mehr als einem Faktor zwei in Pb-Pb Kollisionen ein Endzustands-Effekt ist.

Vorherige Resultate von ALICE suggerieren, dass die Teilchenproduktion für p-Pb Kollisionen mit hoher Multiplizität auch kollektiven Endzustands-Effekten unterliegt [ALICE13e, ALICE13d]. Mit der Messung der Transversalimpuls-Verteilungen von Pionen, Kaonen und Protonen wurden einige Beobachtungen gemacht, die an die Teilchenproduktion in Schwerionenkollisionen erinnern. Hier werden sie in der Regel radialem Fluss zugeschrieben, der durch einen hydrodynamisch expandierenden Feuerball entsteht.

Das mögliche hydrodynamische Verhalten von p-Pb Kollisionen wurde untersucht, indem das Blast-Wave Modell auf die gemessenen Daten angewendet wurde. Dieses Modell ist sehr einfach und hat klare Limitationen. Es wurde jedoch ein Trend beobachtet, der vergleichbar mit den Resultaten von Pb-Pb Kollisionen ist. Zusätzlich können Modelle wie EPOS LHC und das Kraków Modell, die Endzustands-Effekte berücksichtigen, die Daten besser beschreiben als DPMJET, welches keine Endzustands-Effekte beinhaltet.

Das Verhältnis von Baryonen zu Mesonen  $p/\pi$  ( $\Lambda/\pi$ ) zeigt, dass die Protonproduktion (Lambdaproduktion) bei mittleren Transversalimpulsen erhöht und bei niedrigen Transversalimpulsen verringert ist, wenn man p-Pb Kollisionen mit hoher Multiplizität mit Kollisionen geringer Multiplizität vergleicht. Diese Beobachtung wurde zuvor auch bei Schwerionenkollisionen gemacht und wird in der Regel als eine Impulserhöhung, induziert von radialem Fluss, interpretiert.

Zusätzlich wurde ein ansteigender mittlerer Transversalimpuls für höhere Teilchenmassen und Multiplizitäten gemessen. Dies ist typisch für ein Medium, das sich kollektiv ausdehnt und wurde auch in Schwerionenkollisionen beobachtet. Diese Massenabhängigkeit ist mit dem  $\langle p_T \rangle$  von Deuteronen in p-Pb Kollisionen nicht gegeben. Allerdings sind Deuteronen nur schwach gebunden und ihre Produktion wird eventuell nicht durch den selben Effekt beeinflusst, der die nicht zusammengesetzten Hadronen antreibt.

Tatsächlich suggeriert das Verhältnis von Deuteronen zu Protonen als Funktion der geladenen Teilchenmultiplizität, dass Deuteronen durch Koaleszenz aus einem Proton und einem Neutron, die nah im Phasenraum sind, gebildet werden. Die Saturation des Verhältnisses von Deuteronen zu Protonen deutet an, dass die Deuteronenproduktion eher durch die Nukleonendichte als durch die Nukleonenmultiplizität bestimmt wird. Während thermisch-statistische Modelle sehr erfolgreich in der Beschreibung von Hadronen und leichten Kernen in Schwerionenkollisionen sind, ist die Fitqualität für p-Pb Kollisionen mit hoher Multiplizität schlecht.

Zusammenfassend trägt diese Arbeit zum Verständnis der Teilchenproduktion in Proton-Nukleus Kollisionen bei und es wird eine gute Referenz für Schwerionenkollisionen bereit gestellt. Allerdings wurden einige Beobachtungen gemacht, die die Hypothese von kollektiven Endzustands-Effekten in p-Pb Kollisionen mit hoher Multiplizität unterstützen. In diesem Zusammenhang ist es unter Umständen sinnvoll,

---

die Interpretation der Ergebnisse von Schwerionenkollisionen mit mehr Vorsicht zu formulieren. Auf der anderen Seite darf nicht ausgeschlossen werden, dass in p-Pb Kollisionen mit hoher Multiplizität ein kleiner Tropfen eines QGP erzeugt werden kann. In jedem Fall wurde gezeigt, dass Proton-Nukleus Kollisionen nicht nur ein Kontrollexperiment sind, sondern selber ein großes Potenzial für Entdeckungen bieten.





## A. Kinematic Variables

In the following some commonly used variables for ultra-relativistic particle collisions will be introduced. Please note that the convention  $c = \hbar = 1$  is used. The four-momentum is defined as  $P = (E, p_x, p_y, p_z)$  and its absolute value gives the Lorentz-invariant mass  $m_{inv}$ :

$$m_{inv}^2 = P^2 = E^2 - p_x^2 - p_y^2 - p_z^2 \quad (\text{A.1})$$

Considering two incoming particles of a ultra-relativistic collision with four-momenta  $P_A$  and  $P_B$ , the energy in the center-of-mass frame is given by the square-root of the Mandelstam variable  $\sqrt{s}$ , where:

$$s = (P_A + P_B)^2 \quad (\text{A.2})$$

Usually, for heavy-ion collisions the energy of a nucleon-nucleon collision  $\sqrt{s_{NN}}$  is stated. The energy is per definition invariant under Lorentz transformation.

The particle momentum is divided in longitudinal momentum  $p_L$  or  $p_z$  and transverse momentum  $p_T$ . Here, longitudinal refers to the momentum fraction parallel to the beam axis and transverse to the fraction perpendicular to it:

$$p_L = p \cos \theta = p_z \quad (\text{A.3})$$

$$p_T = p \sin \theta = \sqrt{p_x^2 + p_y^2}, \quad (\text{A.4})$$

where  $p$  is the absolute value of  $P$  and  $\theta$  is the angle of the particle with respect to the beam axis.  $p_T$  is invariant under Lorentz transformation in z-direction, whereas  $p_L$  is not and the dimensionless rapidity  $y$  is defined:

$$y = \frac{1}{2} \ln \left( \frac{E + p_L}{E - p_L} \right), \quad (\text{A.5})$$

which is additive under Lorentz transformation in z-direction. The rapidity of a particle can only be calculated, if the mass is known. For this reason the pseudo-rapidity  $\eta$  is defined:

$$\eta = -\ln \left[ \tan \left( \frac{\theta}{2} \right) \right] = \frac{1}{2} \left( \frac{p + p_L}{p - p_L} \right). \quad (\text{A.6})$$

It is a good approximation of the rapidity for high momentum particles, where  $E \gg m_0$  and is exact for mass-less particles.

Transverse momentum distributions are usually given as invariant yields  $\frac{d^3N}{dp^3}$ , which can be re-written as:

$$E \frac{d^3N}{dp^3} = \frac{d^2N}{2\pi p_T dp_T dy} \quad (\text{A.7})$$

with the previously defined quantities and the integration over the the azimuthal direction. The last term is a common way to express the invariant  $p_T$ -differential particle yield in high energy physics. Please note, that it is only Lorentz-invariant, when dividing by  $E$ .

# List of Figures

2.1. Strong coupling $\alpha_s$ as function of $Q$ . . . . .	7
2.2. QCD phase diagram . . . . .	10
2.3. Space-time evolution of heavy-ion collision . . . . .	12
2.4. Elliptic flow of identified particles in p-Pb collisions . . . . .	17
2.5. Nuclear modification factor $R_{AA}$ . . . . .	19
2.6. Exponent $\alpha$ of Cronin effect as a function of $p_T$ . . . . .	22
2.7. Sketch: structure function of nucleus normalized to deuterium . . . . .	24
2.8. Flavor distributions $xf$ at $Q^2 = 10 \text{ GeV}^2$ as a function of $x$ . . . . .	26
2.9. Gluon distributions $xg$ at different $Q^2$ as a function of $x$ . . . . .	27
3.1. Sketch of the ALICE detector . . . . .	30
3.2. ITS PID performance in p-Pb collisions . . . . .	32
3.3. TPC PID performance in p-Pb collisions . . . . .	34
3.4. TOF PID performance in p-Pb collisions . . . . .	36
3.5. Reconstruction scheme for ALICE data in the central barrel . . . . .	39
4.1. Geometry for Glauber calculations . . . . .	45
5.1. Effect of different rapidity ranges for pions and protons . . . . .	54
5.2. Global tracking efficiency of $\pi$ , K, and p . . . . .	55
5.3. TOF matching efficiency of $\pi$ , K, and p . . . . .	56
5.4. Secondary fit of protons (example) . . . . .	58
5.5. Fit to remove electron contamination in kaon signal (example) . . . . .	60
5.6. MC closure test minimum bias . . . . .	61
5.7. Sources of systematic uncertainties . . . . .	63
5.8. Full systematic uncertainties . . . . .	65
5.9. Fit to TOF signal (example) . . . . .	67
5.10. PID with the TPC in the relativistic rise region . . . . .	68
5.11. Invariant $p_T$ -differential yields of pions, kaons and protons . . . . .	70
5.12. Integrated kaon and proton yield $dN/dy$ normalized to pions . . . . .	73
5.13. Kaon and proton to pion ratio as function of $p_T$ . . . . .	75
5.14. Scaling of proton over pion ratio with multiplicity . . . . .	77
5.15. $\langle p_T \rangle$ of identified particles as a function of charged particle multiplicity . . . . .	79
5.16. Blast-Wave fit for p-Pb collisions . . . . .	81
5.17. Blast-Wave fit quality for pp and Pb-Pb collisions . . . . .	82

5.18. Blast-Wave parameters for different collision systems and PYTHIA . . . . .	83
5.19. Example for interpolation of pp reference to $\sqrt{s_{NN}} = 5.02$ TeV . . . . .	86
5.20. Nuclear modification factors of pions, kaons and protons . . . . .	87
5.21. Comparison of pion, kaon, proton and lambda spectra with models . . . . .	89
6.1. Deuteron spectra for two different rapidity ranges . . . . .	93
6.2. Transverse momentum correction for deuterons . . . . .	94
6.3. Comparison of efficiencies for enhanced and standard MC production . . . . .	95
6.4. TPC PID performance . . . . .	96
6.5. Fit of squared deuteron mass measured with TOF . . . . .	98
6.6. Absorption in Geant 3 + optical model and Geant 4 . . . . .	99
6.7. Tracking and TOF matching efficiency for (anti-)deuterons . . . . .	100
6.8. Example of template fit to calculate secondary deuteron contribution . . . . .	102
6.9. Secondary correction for deuterons as a function of $p_T$ . . . . .	103
6.10. Systematic uncertainties of deuterons . . . . .	104
6.11. Systematic uncertainties of anti-deuterons . . . . .	105
6.12. Deuteron and anti-deuteron transverse momentum distributions . . . . .	108
6.13. Anti-deuteron over deuteron ratio . . . . .	110
6.14. $\langle p_T \rangle$ of deuterons as a function of charged particle multiplicity . . . . .	111
6.15. Deuteron over proton ratio as a function of multiplicity . . . . .	112
6.16. Coalescence parameter $B_2$ for p-Pb collisions . . . . .	114
6.17. Thermal fit to the most central Pb-Pb events . . . . .	117
6.18. Thermal fit to high multiplicity p-Pb events . . . . .	119

# List of Tables

2.1. Properties of the six quarks . . . . .	6
4.1. Parameters for p-Pb Glauber calculations . . . . .	47
5.1. Event classes in p-Pb collisions . . . . .	52
5.2. Track selection cuts for $\pi$ , K, and p track candidates . . . . .	53
5.3. Integrated yields $dN/dy$ of pions, kaons and protons . . . . .	71
6.1. Data used for the deuteron analysis . . . . .	92
6.2. Multiplicity bins and charged particle multiplicity at mid-rapidity . .	93
6.3. Integrated yields $dN/dy$ of deuterons and anti-deuterons . . . . .	107
6.4. Integrated anti-deuteron to deuteron ratio . . . . .	109



# Bibliography

- [A<sup>+</sup>00] A. Akindinov et al., *The multigap resistive plate chamber as a time-of-flight detector*, Nucl. Instrum. Meth. **A456**(1–2), 16 – 22 (2000).
- [AAA<sup>+</sup>10] J. Alme, Y. Andres, H. Appelshauser, S. Bablok, N. Bialas et al., *The ALICE TPC, a large 3-dimensional tracking device with fast readout for ultra-high multiplicity events*, Nucl. Instrum. Meth. **A622**, 316–367 (2010).
- [AAA<sup>+</sup>13] A. Akindinov, A. Alici, A. Agostinelli, P. Antonioli, S. Arcelli et al., *Performance of the ALICE Time-Of-Flight detector at the LHC*, Eur. Phys. J. Plus **128**, 44 (2013).
- [ABMRS11] A. Andronic, P. Braun-Munzinger, K. Redlich and J. Stachel, *The thermal model on the verge of the ultimate test: particle production in Pb-Pb collisions at the LHC*, J. Phys. **G38**, 124081 (2011).
- [ABMS06] A. Andronic, P. Braun-Munzinger and J. Stachel, *Hadron production in central nucleus-nucleus collisions at chemical freeze-out*, Nucl. Phys. **A772**, 167–199 (2006).
- [ABMS09] A. Andronic, P. Braun-Munzinger and J. Stachel, *Thermal hadron production in relativistic nuclear collisions: The hadron mass spectrum, the horn, and the QCD phase transition*, Phys. Lett. **B673**(2), 142 – 145 (2009).
- [ABMSS11] A. Andronic, P. Braun-Munzinger, J. Stachel and H. Stocker, *Production of light nuclei, hypernuclei and their antiparticles in relativistic nuclear collisions*, Phys. Lett. **B697**, 203–207 (2011).
- [Acc02] A. Accardi, *Cronin effect in proton nucleus collisions: A Survey of theoretical models*, (2002), hep-ph/0212148.
- [ACF<sup>+</sup>79] D. Antreasyan, J. Cronin, H. J. Frisch, M. Shochet, L. Kluberg et al., *Production of Hadrons at Large Transverse Momentum in 200 GeV, 300 GeV and 400 GeV pp and pn Collisions*, Phys. Rev. **D19**, 764–778 (1979).
- [AEF<sup>+</sup>06] Y. Aoki, G. Endrodi, Z. Fodor, S. Katz and K. Szabo, *The Order of the quantum chromodynamics transition predicted by the standard model of particle physics*, Nature **443**, 675–678 (2006).
- [AF<sup>+</sup>13] R. Alemany-Fernandez et al., *Operation and Configuration of the LHC in Run 1*, (2013).

- [AKST10] N. Armesto, A. B. Kaidalov, C. A. Salgado and K. Tywoniuk, *Nuclear shadowing in Glauber-Gribov theory with Q2-evolution*, Eur. Phys. J. **C68**, 447–457 (2010), 1003.2947.
- [ALI14a] ALICE Offline, <http://aliceinfo.cern.ch/Offline>, 2014, Accessed: 17.09.2014.
- [Ali14b] AliEn: Alice Environment, <http://alien2.cern.ch/>, 2014, Accessed: 19.09.2014.
- [ALICE99] L. Riccati et al. (ALICE Collaboration), *ALICE Inner Tracking System (ITS): Technical Design Report*, (1999).
- [ALICE03] I. Hrivnacova et al. (ALICE Collaboration), *The Virtual Monte Carlo*, (2003), cs.SE/0306005.
- [ALICE04] F. Carminati et al. (ALICE Collaboration), *ALICE: Physics performance report, volume I*, J. Phys. **G30**, 1517–1763 (2004).
- [ALICE06] B. Alessandro et al. (ALICE Collaboration), *ALICE: Physics performance report, volume II*, J. Phys. **G32**, 1295–2040 (2006).
- [ALICE08] K. Aamodt et al. (ALICE Collaboration), *The ALICE experiment at the CERN LHC*, JINST **3**, S08002 (2008).
- [ALICE10] K. Aamodt et al. (ALICE Collaboration), *Midrapidity antiproton-to-proton ratio in pp collisions at  $\sqrt{s} = 0.9$  and 7 TeV measured by the ALICE experiment*, Phys. Rev. Lett. **105**, 072002 (2010).
- [ALICE11a] K. Aamodt et al. (ALICE Collaboration), *Centrality dependence of the charged-particle multiplicity density at mid-rapidity in Pb-Pb collisions at  $\sqrt{s_{NN}} = 2.76$  TeV*, Phys. Rev. Lett. **106**, 032301 (2011).
- [ALICE11b] K. Aamodt et al. (ALICE Collaboration), *Production of pions, kaons and protons in pp collisions at  $\sqrt{s} = 900$  GeV with ALICE at the LHC*, Eur. Phys. J. **C71**, 1655 (2011).
- [ALICE11c] I. Hrivnacova, O. Datskova, A. Gheata, A. Morsch and E. Sicking (ALICE Collaboration), *The ALICE Geant4 simulation*, J. Phys. Conf. Ser. **331**, 032016 (2011).
- [ALICE12a] B. Abelev et al. (ALICE Collaboration), *Pion, Kaon, and Proton Production in Central Pb–Pb Collisions at  $\sqrt{s_{NN}} = 2.76$  TeV*, Phys. Rev. Lett. **109**, 252301 (2012).
- [ALICE12b] B. Abelev et al. (ALICE Collaboration), *Transverse Momentum Distribution and Nuclear Modification Factor of Charged Particles in p-Pb Collisions at  $\sqrt{s_{NN}} = 5.02$  TeV*, Phys. Rev. Lett. **110**, 082302 (2012).
- [ALICE13a] B. Abelev et al. (ALICE Collaboration), *Centrality Dependence of Charged Particle Production at Large Transverse Momentum in Pb–Pb Collisions at  $\sqrt{s_{NN}} = 2.76$  TeV*, Phys. Lett. **B720**, 52–62 (2013).



- 
- [ALICE13b] B. Abelev et al. (ALICE Collaboration), *Centrality dependence of  $\pi$ ,  $K$ ,  $p$  production in Pb-Pb collisions at  $\sqrt{s_{NN}} = 2.76$  TeV*, Phys. Rev. **C88**(4), 044910 (2013).
  - [ALICE13c] B. Abelev et al. (ALICE Collaboration), *Centrality determination of Pb-Pb collisions at  $\sqrt{s_{NN}} = 2.76$  TeV with ALICE*, Phys. Rev. **C88**(4), 044909 (2013).
  - [ALICE13d] B. Abelev et al. (ALICE Collaboration), *Long-range angular correlations of  $\pi$ ,  $K$  and  $p$  in p-Pb collisions at  $\sqrt{s_{NN}} = 5.02$  TeV*, Phys. Lett. **B726**, 164–177 (2013).
  - [ALICE13e] B. Abelev et al. (ALICE Collaboration), *Long-range angular correlations on the near and away side in p-Pb collisions at  $\sqrt{s_{NN}} = 5.02$  TeV*, Phys. Lett. **B719**, 29–41 (2013).
  - [ALICE13f] B. Abelev et al. (ALICE Collaboration), *Measurement of inelastic, single- and double-diffraction cross sections in proton–proton collisions at the LHC with ALICE*, Eur. Phys. J. **C73**, 2456 (2013).
  - [ALICE13g] B. Abelev et al. (ALICE Collaboration), *Multiplicity dependence of the average transverse momentum in pp, p-Pb, and Pb-Pb collisions at the LHC*, Phys. Lett. **B727**, 371–380 (2013).
  - [ALICE13h] B. Abelev et al. (ALICE Collaboration), *Pseudorapidity density of charged particles in p-Pb collisions at  $\sqrt{s_{NN}} = 5.02$  TeV*, Phys. Rev. Lett. **110**, 032301 (2013).
  - [ALICE13i] B. Abelev et al. (ALICE Collaboration), *Upgrade of the ALICE Time Projection Chamber*, Technical Report CERN-LHCC-2013-020. ALICE-TDR-016, CERN, Geneva, 2013.
  - [ALICE13j] R. Haake (ALICE Collaboration), *Charged Jets in Minimum Bias p-Pb Collisions at  $\sqrt{s_{NN}} = 5.02$  TeV with ALICE*, PoS EPS-HEP2013 , 176 (2013).
  - [ALICE14a] B. Abelev et al. (ALICE Collaboration), *Measurement of charged jet suppression in Pb-Pb collisions at  $\sqrt{s_{NN}} = 2.76$  TeV*, JHEP **1403**, 013 (2014).
  - [ALICE14b] B. Abelev et al. (ALICE Collaboration), *Transverse momentum dependence of inclusive primary charged-particle production in p-Pb collisions at  $\sqrt{s_{NN}} = 5.02$  TeV*, Eur. Phys. J. **C74**, 3054 (2014).
  - [ALICE14c] B. Abelev et al. (ALICE Collaboration), *Centrality dependence of particle production in p-Pb collisions at  $\sqrt{s_{NN}} = 5.02$  TeV*, (2014), in preperation.
  - [ALICE14d] B. Abelev et al. (ALICE Collaboration), *Centrality dependence of the nuclear modification factor of charged pions, kaons, and protons in Pb-Pb collisions at  $\sqrt{s_{NN}} = 2.76$  TeV*, (2014), in preperation.
  - [ALICE14e] B. Abelev et al. (ALICE Collaboration), *Elliptic flow of identified hadrons in Pb-Pb collisions at  $\sqrt{s_{NN}} = 2.76$  TeV*, (2014), 1405.4632.

- [ALICE14f] B. Abelev et al. (ALICE Collaboration), *Measurement of light nuclei and anti-nuclei in pp and Pb–Pb collisions at LHC energies*, (2014), in preperation.
- [ALICE14g] B. Abelev et al. (ALICE Collaboration), *Measurement of pion, kaon and proton production in proton-proton collisions at  $\sqrt{s} = 7$  TeV*, (2014), in preperation.
- [ALICE14h] B. Abelev et al. (ALICE Collaboration), *Multiplicity Dependence of Pion, Kaon, Proton and Lambda Production in p–Pb Collisions at  $\sqrt{s_{NN}} = 5.02$  TeV*, Phys. Lett. **B728**(0), 25 – 38 (2014).
- [ALICE14i] B. Abelev et al. (ALICE Collaboration), *Performance of the ALICE Experiment at the CERN LHC*, (2014), 1402.4476.
- [ALICE14j] B. Abelev et al. (ALICE Collaboration), *Production of charged pions, kaons and protons at large transverse momenta in pp and Pb-Pb collisions at  $\sqrt{s_{NN}} = 2.76$  TeV*, (2014), 1401.1250.
- [ALICE14k] D. Alexandre (ALICE Collaboration), *Multi-strange baryon production in pp, p-Pb and Pb-Pb collisions measured with ALICE at the LHC*, Presented at Quark Matter, Darmstadt, Germany <https://indico.cern.ch/event/219436/session/19/contribution/207>, 2014.
- [ALICE14l] D. Alexandre (ALICE Collaboration), *Multi-strange baryon production in pp, p-Pb and Pb–Pb collisions measured with ALICE at the LHC*, Nucl. Phys. **A**, in press (2014), 1410.2117.
- [ALICE14m] C. Andrei (ALICE Collaboration), *Light flavor hadron spectra at low- $p_T$  and search for collective phenomena in high multiplicity pp, p-Pb and Pb-Pb collisions measured with the ALICE experiment*, Presented at Quark Matter, Darmstadt, Germany <https://indico.cern.ch/event/219436/session/9/contribution/232>, 2014.
- [ALICE14n] J. Anielski (ALICE Collaboration), *Transverse Momentum Distributions of Identified Particles in p-Pb Collisions at  $\sqrt{s_{NN}} = 5.02$  TeV*, J. Phys. Conf. Ser. **509**, 012106 (2014).
- [ALICE14o] F. Bellini (ALICE Collaboration), *Hadronic resonance production measured by ALICE at the LHC*, Nucl. Phys. **A**, in press (2014).
- [ALICE14p] J. F. Grosse-Oetringhaus (ALICE Collaboration), *Overview of ALICE Results at Quark Matter 2014*, (2014), 1408.0414.
- [ALICE14q] M. Meres (ALICE Collaboration), *Midrapidity antibaryon-to-baryon ratios in Pb-Pb and p-Pb collisions measured by the ALICE experiment*, Presented at Quark Matter, Darmstadt, Germany <https://indico.cern.ch/event/219436/session/2/contribution/195>, 2014.

- 
- [ALICE14r] A. Ortiz Velasquez (ALICE Collaboration), *Production of  $\pi/K/p$  from intermediate to high  $p_T$  in  $pp$ ,  $p$ -Pb and Pb-Pb collisions measured by ALICE*, (2014), 1404.4354.
  - [AR10] B. Alver and G. Roland, *Collision geometry fluctuations and triangular flow in heavy-ion collisions*, Phys. Rev. **C81**, 054905 (2010).
  - [Arm06] N. Armesto, *Nuclear shadowing*, J. Phys. **G32**, R367–R394 (2006).
  - [Arn94] M. Arneodo, *Nuclear effects in structure functions*, Phys. Rept. **240**, 301–393 (1994).
  - [ATL14a] Centrality and rapidity dependence of inclusive jet production in  $\sqrt{s_{NN}} = 5.02$  TeV proton–lead collisions with the ATLAS detector, Technical Report ATLAS-CONF-2014-024, CERN, Geneva, 2014.
  - [ATL14b] Charged hadron production in  $p$ +Pb collisions at  $\sqrt{s_{NN}} = 5.02$  TeV measured at high transverse momentum by the ATLAS experiment, Technical Report ATLAS-CONF-2014-029, CERN, Geneva, 2014.
  - [ATLAS12a] G. Aad et al. (ATLAS Collaboration), *Combined search for the Standard Model Higgs boson using up to  $4.9\text{ fb}^{-1}$  of  $pp$  collision data at  $\sqrt{s} = 7$  TeV with the ATLAS detector at the LHC*, Phys. Lett. **B710**, 49–66 (2012).
  - [ATLAS12b] G. Aad et al. (ATLAS Collaboration), *Observation of a new particle in the search for the Standard Model Higgs boson with the ATLAS detector at the LHC*, Phys. Lett. **B716**, 1–29 (2012).
  - [ATLAS13a] G. Aad et al. (ATLAS Collaboration), *Measurement of the jet radius and transverse momentum dependence of inclusive jet suppression in lead-lead collisions at  $\sqrt{s_{NN}} = 2.76$  TeV with the ATLAS detector*, Phys. Lett. **B719**, 220–241 (2013).
  - [ATLAS13b] G. Aad et al. (ATLAS Collaboration), *Observation of Associated Near-side and Away-side Long-range Correlations in  $\sqrt{s_{NN}} = 5.02$  TeV Proton-lead Collisions with the ATLAS Detector*, Phys. Rev. Lett. **110**, 182302 (2013).
  - [B<sup>+</sup>94] J. Barrette et al., *Production of light nuclei in relativistic heavy-ion collisions*, Phys. Rev. **C50**, 1077–1084 (1994).
  - [BBB<sup>+</sup>98] S. Bass, M. Belkacem, M. Bleicher, M. Brandstetter, L. Bravina et al., *Microscopic models for ultrarelativistic heavy ion collisions*, Prog. Part. Nucl. Phys. **41**, 255–369 (1998).
  - [BBC76] A. Białas, M. Bleszyński and W. Czyż, *Multiplicity distributions in nucleus-nucleus collisions at high energies*, Nucl. Phys. **B111**(3), 461 – 476 (1976).
  - [BCG94] R. Brun, F. Carminati and S. Giani, *GEANT Detector Description and Simulation Tool*, (1994), CERN-W5013.
  - [BCL<sup>+</sup>04] O. S. Brüning, P. Collier, P. Lebrun, S. Myers, R. Ostojic, J. Poole and P. Proudlock, *LHC Design Report*, CERN, Geneva, 2004.

- [Belle13] Z. Q. Liu et al. (Belle Collaboration), *Study of  $e^+e^- \rightarrow \pi^+\pi^- J/\psi$  and Observation of a Charged Charmoniumlike State at Belle*, Phys. Rev. Lett. **110**, 252002 (2013).
- [BESIII13] M. Ablikim et al. (BESIII Collaboration), *Observation of a Charged Charmoniumlike Structure in  $e^+e^- \rightarrow \pi^+\pi^- J/\psi$  at  $\sqrt{s} = 4.26$  GeV*, Phys. Rev. Lett. **110**, 252001 (2013).
- [Bet13] S. Bethke, *World Summary of  $\alpha_s$  (2012)*, Nucl. Phys. Proc. Suppl. **234**, 229–234 (2013).
- [Bjo83] J. Bjorken, *Highly Relativistic Nucleus-Nucleus Collisions: The Central Rapidity Region*, Phys. Rev. **D27**, 140–151 (1983).
- [Blo30] H. Bloch, *Zur Theorie des Durchgangs schneller Korpuskularstrahlen durch Materie*, Ann. Phys. **397**, 325 – 400 (1930).
- [BMRS03] P. Braun-Munzinger, K. Redlich and J. Stachel, *Particle production in heavy ion collisions*, (2003), nucl-th/0304013.
- [BMS<sup>+</sup>07a] G. Battistoni, S. Muraro, P. R. Sala, F. Cerutti, A. Ferrari et al., *The FLUKA code: Description and benchmarking*, AIP Conf. Proc. **896**, 31–49 (2007).
- [BMS07b] P. Braun-Munzinger and J. Stachel, *The quest for the quark-gluon plasma*, Nature **448**, 302–309 (2007).
- [Boz12a] P. Bozek, *Collective flow in p-Pb and d-Pb collisions at TeV energies*, Phys. Rev. **C85**, 014911 (2012).
- [Boz12b] P. Bozek, *Hydrodynamic flow from RHIC to LHC*, Acta Phys. Polon. **B43**, 689 (2012), 1111.4398.
- [BP63] S. T. Butler and C. A. Pearson, *Deuterons from High-Energy Proton Bombardment of Matter*, Phys. Rev. **129**, 836–842 (1963).
- [BRAHMS05a] I. Arsene et al. (BRAHMS Collaboration), *Centrality dependent particle production at  $y=0$  and  $y \sim 1$  in Au + Au collisions at  $\sqrt{s_{NN}} = 200$  GeV*, Phys. Rev. **C72**, 014908 (2005).
- [BRAHMS05b] I. Arsene et al. (BRAHMS Collaboration), *Quark gluon plasma and color glass condensate at RHIC? The Perspective from the BRAHMS experiment*, Nucl. Phys. **A757**, 1–27 (2005).
- [BRR08] W. Blum, W. Riegler and L. Rolandi, *Particle Detection with Drift Chambers*, Particle Acceleration and Detection, Springer, 2008.
- [Bug96] K. A. Bugaev, *Shock - like freezeout in relativistic hydrodynamics*, Nucl. Phys. **A606**, 559–567 (1996), nucl-th/9906047.
- [BWP12] P. Bozek and I. Wyskiel-Piekarska, *Particle spectra in Pb-Pb collisions at  $\sqrt{s_{NN}} = 2.76$  TeV*, Phys. Rev. **C85**, 064915 (2012).
- [CF74] F. Cooper and G. Frye, *Single-particle distribution in the hydrodynamic and statistical thermodynamic models of multiparticle production*, Phys. Rev. **D10**, 186–189 (1974).

- 
- [CFS<sup>+</sup>73] J. Cronin, H. J. Frisch, M. Shochet, J. Boymond, P. Piroue et al., *Production of Hadrons with Large Transverse Momentum at 200 GeV and 300 GeV.*, Phys. Rev. Lett. **31**, 1426–1429 (1973).
- [CJJ<sup>+</sup>74] A. Chodos, R. L. Jaffe, K. Johnson, C. B. Thorn and V. F. Weisskopf, *New extended model of hadrons*, Phys. Rev. **D9**, 3471–3495 (Jun 1974).
- [CKK<sup>+</sup>11] J. Cleymans, S. Kabana, I. Kraus, H. Oeschler, K. Redlich et al., *Antimatter production in proton-proton and heavy-ion collisions at ultrarelativistic energies*, Phys. Rev. **C84**, 054916 (2011).
- [CMS11a] S. Chatrchyan et al. (CMS Collaboration), *Observation and studies of jet quenching in PbPb collisions at  $\sqrt{s_{NN}} = 2.76$  TeV*, Phys. Rev. **C84**, 024906 (2011).
- [CMS11b] S. Chatrchyan et al. (CMS Collaboration), *Study of Z boson production in PbPb collisions at nucleon-nucleon centre of mass energy = 2.76 TeV*, Phys. Rev. Lett. **106**, 212301 (2011).
- [CMS12a] S. Chatrchyan et al. (CMS Collaboration), *Combined results of searches for the standard model Higgs boson in pp collisions at  $\sqrt{s} = 7$  TeV*, Phys. Lett. **B710**, 26–48 (2012).
- [CMS12b] S. Chatrchyan et al. (CMS Collaboration), *Measurement of isolated photon production in pp and PbPb collisions at  $\sqrt{s_{NN}} = 2.76$  TeV*, Phys. Lett. **B710**, 256–277 (2012).
- [CMS12c] S. Chatrchyan et al. (CMS Collaboration), *Study of high-pT charged particle suppression in PbPb compared to pp collisions at  $\sqrt{s_{NN}} = 2.76$  TeV*, Eur. Phys. J. **C72**, 1945 (2012).
- [CMS12d] S. Chatrchyan et al. (CMS Collaboration), *Study of the inclusive production of charged pions, kaons, and protons in pp collisions at  $\sqrt{s} = 0.9, 2.76$ , and 7 TeV*, Eur. Phys. J. **C72**, 2164 (2012).
- [CMS12e] S. Chatrchyan et al. (CMS Collaboration), *Study of W boson production in PbPb and pp collisions at  $\sqrt{s_{NN}} = 2.76$  TeV*, Phys. Lett. **B715**, 66–87 (2012).
- [CMS13a] Charged particle nuclear modification factor and pseudorapidity asymmetry in pPb collisions at  $\sqrt{s_{NN}} = 5.02$  TeV with CMS, Technical Report CMS-PAS-HIN-12-017, CERN, Geneva, 2013.
- [CMS13b] S. Chatrchyan et al. (CMS Collaboration), *Observation of long-range near-side angular correlations in proton-lead collisions at the LHC*, Phys. Lett. **B718**, 795–814 (2013).
- [CMS14a] Measurement of inclusive jet nuclear modification factor in pPb collisions at  $\sqrt{s_{NN}} = 5.02$  TeV with CMS, Technical Report CMS-PAS-HIN-14-001, CERN, Geneva, 2014.

- [CMS14b] S. Chatrchyan et al. (CMS Collaboration), *Study of the production of charged pions, kaons, and protons in pPb collisions at  $\sqrt{s_{NN}} = 5.02$  TeV*, Eur. Phys. J. **C74**, 2847 (2014).
- [CP75a] N. Cabibbo and G. Parisi, *Exponential Hadronic Spectrum and Quark Liberation*, Phys. Lett. **B59**, 67–69 (1975).
- [CP75b] J. C. Collins and M. J. Perry, *Superdense Matter: Neutrons or Asymptotically Free Quarks?*, Phys. Rev. Lett. **34**, 1353–1356 (1975).
- [CSTT94] A. Capella, U. Sukhatme, C. I. Tan and J. Tran Thanh Van, *Dual parton model*, Phys. Rept. **236**, 225–329 (1994).
- [DDG<sup>+</sup>71] S. Denisov, S. Donskov, Y. Gorin, V. Kachanov, V. Kutjin, A. Petrukhin, Y. Prokoshkin, E. Razuvaev, R. Shuvalov and D. Stojanova, *Measurements of antideuteron absorption and stripping cross sections at the momentum 13.3 GeV/c*, Nucl. Phys. **B31**(2), 253 – 260 (1971).
- [DH77] K. Das and R. C. Hwa, *Quark-antiquark recombination in the fragmentation region*, Phys. Lett **B68**(5), 459 – 462 (1977).
- [E<sup>+</sup>05] C. Eck et al., *LHC computing Grid: Technical Design Report*, CERN, Geneva, 2005.
- [EB08] L. Evans and P. Bryant, *LHC Machine*, J. Instrum. **3**(08), S08001 (2008).
- [EKL89] K. Eskola, K. Kajantie and J. Lindfors, *Quark and gluon production in high energy nucleus-nucleus collisions*, Nucl. Phys. **B323**(1), 37 – 52 (1989).
- [EMC83] J. Aubert et al. (EMC Collaboration), *The ratio of the nucleon structure functions  $F_2^n$  for iron and deuterium*, Phys. Lett. **B123**, 275 (1983).
- [ER96] R. Engel and J. Ranft, *Hadronic photon-photon interactions at high energies*, Phys. Rev. **D54**, 4244–4262 (1996).
- [Flo14] M. Floris, *Hadron yields and the phase diagram of strongly interacting matter*, (2014), 1408.6403.
- [FMNB03] R. Fries, B. Muller, C. Nonaka and S. Bass, *Hadronization in heavy ion collisions: Recombination and fragmentation of partons*, Phys. Rev. Lett. **90**, 202303 (2003).
- [Fru87] R. Fruehwirth, *Application of Kalman filtering to track and vertex fitting*, Nuc. Instrum. Meth. **A262**(2–3), 444 – 450 (1987).
- [GEANT03] S. Agostinelli et al. (GEANT Collaboration), *GEANT4: A Simulation toolkit*, Nucl. Instrum. Meth. **A506**, 250–303 (2003).
- [GL72] V. Gribov and L. Lipatov, *Deep inelastic e p scattering in perturbation theory*, Sov. J. Nucl. Phys. **15**, 438–450 (1972).

- [GSJ<sup>+</sup>76] H. H. Gutbrod, A. Sandoval, P. J. Johansen, A. M. Poskanzer, J. Gosset, W. G. Meyer, G. D. Westfall and R. Stock, *Final-State Interactions in the Production of Hydrogen and Helium Isotopes by Relativistic Heavy Ions on Uranium*, Phys. Rev. Lett. **37**, 667–670 (1976).
- [HEHS12] I. Helenius, K. J. Eskola, H. Honkanen and C. A. Salgado, *Impact-Parameter Dependent Nuclear Parton Distribution Functions: EPS09s and EKS98s and Their Applications in Nuclear Hard Processes*, JHEP **1207**, 073 (2012).
- [HKH<sup>+</sup>01] P. Huovinen, P. Kolb, U. W. Heinz, P. Ruuskanen and S. Voloshin, *Radial and elliptic flow at RHIC: Further predictions*, Phys. Lett. **B503**, 58–64 (2001).
- [HY04] R. C. Hwa and C. Yang, *Final state interaction as the origin of the Cronin effect*, Phys. Rev. Lett. **93**, 082302 (2004).
- [IV03] E. Iancu and R. Venugopalan, *The Color glass condensate and high-energy scattering in QCD*, (2003), hep-ph/0303204.
- [Kal12] A. Kalweit, *Production of light flavor hadrons and anti-nuclei at the LHC*, PhD thesis, TU Darmstadt, 2012.
- [Kap80] J. I. Kapusta, *Mechanisms for deuteron production in relativistic nuclear collisions*, Phys. Rev. **C21**, 1301–1310 (1980).
- [KB04] C. Klein-Bösing, *Production of Neutral Pions and Direct Photons in Ultra-Relativistic Au+Au Collisions*, PhD thesis, WWU Münster, 2004.
- [KSSS10] M. Kliemant, R. Sahoo, T. Schuster and R. Stock, *Global Properties of Nucleus-Nucleus Collisions*, Lect. Notes Phys. **785**, 23–103 (2010).
- [KSW13] I. A. Karpenko, Y. M. Sinyukov and K. Werner, *Uniform description of bulk observables in the hydrokinetic model of A+A collisions at the BNL Relativistic Heavy Ion Collider and the CERN Large Hadron Collider*, Phys. Rev. **C87**, 024914 (2013).
- [LHCb14] R. Aaij et al. (LHCb Collaboration), *Observation of the resonant character of the  $Z(4430)^-$  state*, Phys. Rev. Lett. **112**, 222002 (2014).
- [LR07] J. Letessier and J. Rafelski, *Strangeness chemical equilibration in QGP at RHIC and CERN LHC*, Phys. Rev. **C75**, 014905 (2007).
- [MO97] A. Moiseev and J. Ormes, *Inelastic cross section for antihelium on nuclei: an empirical formula for use in the experiments to search for cosmic antimatter*, Astropart. Phys. **6**, 379–386 (1997).
- [MRSS07] M. L. Miller, K. Reygers, S. J. Sanders and P. Steinberg, *Glauber modeling in high energy nuclear collisions*, Ann. Rev. Nucl. Part. Sci. **57**, 205–243 (2007).

- [MSW12] B. Muller, J. Schukraft and B. Wyslouch, *First Results from Pb+Pb collisions at the LHC*, Ann. Rev. Nucl. Part. Sci. **62**, 361–386 (2012).
- [NA5203] R. Arsenescu et al. (NA52 Collaboration), *An Investigation of the anti-nuclei and nuclei production mechanism in Pb + Pb collisions at 158-A-GeV*, New J. Phys. **5**, 150 (2003).
- [Oll08] J.-Y. Ollitrault, *Relativistic hydrodynamics for heavy-ion collisions*, Eur. J. Phys. **29**(2), 275 (2008).
- [PDG12] J. Beringer et al. (PDG Collaboration), *Review of Particle Physics (RPP)*, Phys. Rev. **D86**, 010001 (2012).
- [Per00] D. Perkins, *Introduction to High Energy Physics*, Cambridge University Press, 2000.
- [PHENIX01] K. Adcox et al. (PHENIX Collaboration), *Suppression of Hadrons with Large Transverse Momentum in Central Au + Au Collisions at  $\sqrt{s_{NN}} = 130$  GeV*, Phys. Rev. Lett. **88**, 022301 (2001).
- [PHENIX04a] S. Adler et al. (PHENIX Collaboration), *High- $p_T$  charged hadron suppression in Au + Au collisions at  $\sqrt{s_{NN}} = 200$  GeV*, Phys. Rev. **C69**, 034910 (2004).
- [PHENIX04b] S. S. Adler et al. (PHENIX Collaboration), *Identified charged particle spectra and yields in Au+Au collisions at  $\sqrt{s_{NN}} = 200$  GeV*, Phys. Rev. **C69**, 034909 (2004).
- [PHENIX05] K. Adcox et al. (PHENIX Collaboration), *Formation of dense partonic matter in relativistic nucleus-nucleus collisions at RHIC: Experimental evaluation by the PHENIX collaboration*, Nucl. Phys. **A757**, 184–283 (2005).
- [PHENIX13a] A. Adare et al. (PHENIX Collaboration), *Quadrupole Anisotropy in Dihadron Azimuthal Correlations in Central d+Au Collisions at  $\sqrt{s_{NN}}=200$  GeV*, Phys. Rev. Lett. **111**(21), 212301 (2013).
- [PHENIX13b] A. Adare et al. (PHENIX Collaboration), *Spectra and ratios of identified particles in Au+Au and d+Au collisions at  $\sqrt{s_{NN}} = 200$  GeV*, Phys. Rev. **C88**, 024906 (2013).
- [PHOBOS05] B. Back, M. Baker, M. Ballintijn, D. Barton, B. Becker et al. (PHOBOS Collaboration), *The PHOBOS perspective on discoveries at RHIC*, Nucl. Phys. **A757**, 28–101 (2005).
- [PKK<sup>+</sup>13] T. Pierog, I. Karpenko, J. Katzy, E. Yatsenko and K. Werner, *EPOS LHC : test of collective hadronization with LHC data*, (2013), hep-ph/1306.0121.
- [PLRT14] M. Petran, J. Letessier, J. Rafelski and G. Torrieri, *SHARE with CHARM*, Comput. Phys. Comm. **185**, 2056–2079 (2014).
- [RER00] S. Roesler, R. Engel and J. Ranft, *The Monte Carlo event generator DPMJET-III*, pages 1033–1038 (2000), hep-ph/0012252.



- 
- [Roo14] ROOT Data Analysis Framework, <http://root.cern.ch/drupal/>, 2014, Accessed: 17.09.2014.
  - [SBRS98] J. Sollfrank, F. Becattini, K. Redlich and H. Satz, *Canonical strangeness enhancement*, Nucl. Phys. **A638**, 399C–402C (1998).
  - [SH99] R. Scheibl and U. W. Heinz, *Coalescence and flow in ultrarelativistic heavy ion collisions*, Phys. Rev. **C59**, 1585–1602 (1999).
  - [SHHS11] C. Shen, U. Heinz, P. Huovinen and H. Song, *Radial and elliptic flow in Pb + Pb collisions at energies available at the CERN Large Hadron Collider from viscous hydrodynamics*, Phys. Rev. **C84**, 044903 (2011).
  - [SMS08] T. Sjostrand, S. Mrenna and P. Z. Skands, *A Brief Introduction to PYTHIA 8.1*, Comput. Phys. Commun. **178**, 852–867 (2008), 0710.3820.
  - [Sne11] R. Snellings, *Elliptic Flow: A Brief Review*, New J. Phys. **13**, 055008 (2011).
  - [SS11] H. Schulz and P. Skands, *Energy Scaling of Minimum-Bias Tunes*, Eur. Phys. J. **C71**, 1644 (2011).
  - [SSH93] E. Schnedermann, J. Sollfrank and U. W. Heinz, *Thermal phenomenology of hadrons from 200-A/GeV S+S collisions*, Phys. Rev. **C48**, 2462–2475 (1993).
  - [STAR02] C. Adler et al. (STAR Collaboration), *Centrality Dependence of High- $p_T$  Hadron Suppression in Au+Au Collisions at  $\sqrt{s_{NN}} = 130$  GeV*, Phys. Rev. Lett. **89**, 202301 (2002).
  - [STAR03a] J. Adams et al. (STAR Collaboration), *Evidence from d + Au measurements for final state suppression of high  $p_T$  hadrons in Au+Au collisions at RHIC*, Phys. Rev. Lett. **91**, 072304 (2003).
  - [STAR03b] C. Adler et al. (STAR Collaboration), *Disappearance of Back-To-Back High- $p_T$  Hadron Correlations in Central Au + Au Collisions at  $\sqrt{s_{NN}} = 200$  GeV*, Phys. Rev. Lett. **90**, 082302 (2003).
  - [STAR06] J. Adams et al. (STAR Collaboration), *Identified hadron spectra at large transverse momentum in p+p and d+Au collisions at  $\sqrt{s_{NN}} = 200$ -GeV*, Phys. Lett. **B637**, 161–169 (2006).
  - [STAR09] B. Abelev et al. (STAR Collaboration), *Systematic Measurements of Identified Particle Spectra in pp, d+Au and Au+Au Collisions from STAR*, Phys. Rev. **C79**, 034909 (2009).
  - [STAR14] L. Adamczyk et al. (STAR Collaboration), *Energy Dependence of Moments of Net-Proton Multiplicity Distributions at RHIC*, Phys. Rev. Lett. **112**, 032302 (Jan 2014).
  - [SW07] P. Z. Skands and D. Wicke, *Non-perturbative QCD effects and the top mass at the Tevatron*, Eur. Phys. J. **C52**, 133–140 (2007).

- [SZ13] E. Shuryak and I. Zahed, *High-multiplicity pp and pA collisions: Hydrodynamics at its edge*, Phys. Rev. **C88**(4), 044915 (2013).
- [UAG<sup>+</sup>11] V. Uzhinsky, J. Apostolakis, A. Galoyan, G. Folger, V. Grichine, V. Ivanchenko and D. Wright, *Antinucleus–nucleus cross sections implemented in Geant4*, Phys. Lett. **B705**(3), 235 – 239 (2011).
- [Wan91] Wang, X.N. and Gyulassy, M., *HIJING: A Monte Carlo model for multiple jet production in pp, pA, and AA collisions*, Phys. Rev. **D44**, 3501 (1991).
- [WC09] S. Wheaton and J. Cleymans, *THERMUS: A Thermal model package for ROOT*, Comput. Phys. Commun. **180**, 84–106 (2009).
- [WCH09] S. Wheaton, J. Cleymans and M. Hauer, *THERMUS—A thermal model package for ROOT*, Computer Phys. Comm. **180**(1), 84 – 106 (2009).
- [Wil74] K. G. Wilson, *Confinement of quarks*, Phys. Rev. **D10**, 2445–2459 (Oct 1974).
- [WKB<sup>+</sup>12] K. Werner, I. Karpenko, M. Bleicher, T. Pierog and S. Porteboeuf-Houssais, *Jets, Bulk Matter, and their Interaction in Heavy Ion Collisions at Several TeV*, Phys. Rev. **C85**, 064907 (2012).
- [ZCH<sup>+</sup>96] E. C. Zeballos, I. Crotty, D. Hatzifotiadou, J. L. Valverde, S. Neupane, M. Williams and A. Zichichi, *A new type of resistive plate chamber: The multigap RPC*, Nucl. Instrum. Meth. **A374**(1), 132 – 135 (1996).
- [ZEUS03] S. Chekanov et al. (ZEUS Collaboration), *A ZEUS next-to-leading-order QCD analysis of data on deep inelastic scattering*, Phys. Rev. **D67**, 012007 (2003).

# Danksagung

Diese Arbeit wäre nicht zu Stande gekommen ohne die Unterstützung vieler Menschen. Ich möchte mich hiermit bei der gesamten ALICE Kollaboration und der Arbeitsgruppe um Prof. Dr. Wessels bedanken. Besonders hervorzuheben sind hier Johannes Wessels, Alexander Kalweit und Christian Klein-Bösing.

Für die Unterstützung im privaten Umfeld und für das große Verständnis während der Promotion bedanke ich mich bei Mechthild, Peter, Denis und natürlich Maren und Luise.



# Curriculum Vitae

Name	Jonas Anielski
Geburtsdatum	31.01.1986
Geburtsort	Ibbenbüren
Staatsangehörigkeit	Deutsch
Eltern	Peter Anielski Mechthild Anielski, geb. Löpmeier

## Schulausbildung

08/1992 - 07/1996	Bruder-Klaus-Schule, Brochterbeck
08/1996 - 07/2002	Goethe-Gymnasium, Ibbenbüren
08/2002 - 06/2003	Johansen High School, Modesto, Kalifornien
06/2003 - 05/2005	Goethe-Gymnasium, Ibbenbüren
05/2005	Allgemeine Hochschulreife

## Studium

10/2005 - 03/2011	Diplomstudiengang Physik an der WWU Münster Diplomarbeit in Experimenteller Kernphysik Titel: <i>Entwicklung eines Triggersystems zum Testen und Kalibrieren der Supermodule des ALICE-TRD</i>
03/2011	Diplomprüfung

## Promotionsstudium

06/2011	Beginn der Dissertation am CERN und am Institut für Kernphysik an der WWU Münster unter der Betreuung von Prof. Dr. J. P. Wessels
---------	---

## Berufstätigkeit

10/2008 - 04/2010	Studentische Hilfskraft am Institut für Angewandte Physik an der WWU Münster
04/2010 - 05/2011	Studentische Hilfskraft am Institut für Kernphysik an der WWU Münster
06/2011 - 04/2012	Wissenschaftliche Hilfskraft am Institut für Kernphysik an der WWU Münster
05/2012	Wissenschaftlicher Mitarbeiter am Institut für Kernphysik an der WWU Münster

